Optical Characterisation of Mandovi – Zuari estuaries for Analysing Colour through Remotely Sensed Data

Thesis Submitted to Goa University

For the Degree of Doctor of Philosophy

in

Marine Sciences

By

Nutan P. Sangekar

Department of Marine Sciences

Goa University, Goa – 403 206, India

May 2012

To,

My Parents

Statement

As required by the University ordinance 0.19.8 (vi), I state that the present thesis entitled "**Optical Characterisation of Mandovi-Zuari estuaries for analysing colour through remotely sensed data**" is my original contribution and the same has not been submitted on any previous occasion. To the best of my knowledge the present study is the first comprehensive work of its kind from the area mentioned.
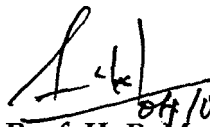
The literature related to the problem investigated has been cited. Due acknowledgements have been made wherever facilities and suggestions have been availed of.
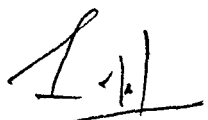
Nutan P. Sangekar

Certificate

This is to certify that the thesis entitled *"**Optical Characterisation of Mandovi-Zuari estuaries for analysing colour through remotely sensed data**"*, submitted by Ms. Nutan P. Sangekar for the award of Doctor of Philosophy in Marine Sciences is based on her original studies carried out by her under my supervision. The thesis or any part thereof has not been previously submitted for any degree or diploma in any Universities or Institutions.

04/07/2012

Prof. H. B. Menon
Research Guide
Head, Department of Marine Sciences
Goa University

All the corrections suggested by referees
have been incorporated.

4.5.2012
(Dr. R. M. Dwivedi)

4/5/2012
(Guide, (Pof. H. B. Menon)

ACKNOWLEDGEMENTS

CONTENTS

List of Figures

List of Tables

Abbreviations

Acronym	Full form
AOP	Apparent Optical Properties
AOT	Aerosol Optical Thickness
AWS	Automatic Weather Station
CDOM	Chromophoric Dissolved Organic Matter
CTD	Conductivity, Temperature and Depth
CZCS	Coastal Zone Colour Scanner
DN	Digital Numbers
EMR	Electro-magnetic radiation
GCP	Ground Control Point
GPS	Global Positioning System
Hyper-OCR	Hyperspectral-Ocean Colour Radiometer
IOP	Inherent Optical Properties
IOCCG	International Ocean Colour Co-ordinating Group
IRS	Indian Remote Sensing
MERIS	Medium Resolution Imaging Spectroradiometer
MODIS	Moderate resolution Imaging Spectroradiometer
MOS	Marine Observation Satellite
NIR	Near Infrared
NOAA-AVHRR	National Oceanic and Atmospheric Administration-
NRSC	National Remote Sensing Centre
OAC	Optically active constituent
OCM	Ocean Colour Monitor
OCTS	Ocean Colour and Temperature Sensor
OD	Optical Density
PAR	Photosynthetically Available Radiation
POLDER	Polarization and Directionality of Earth Reflectance
PSLV	Polar Satellite Launching Vehicle
PSU	Practical Salinity Unit
REVAMP	Regional Validation of MERIS Chlorophyll products
SeaWIFs	Sea-viewing Wide Field-of-view sensor
TSM	Total Suspended Matter

Notations & Symbols

Symbol/ notation	Description
α	Ångström wavelength exponent
β	Ångström turbidity parameter
λ	Wavelength
ψ	Azimuthal angle
ρ	Fresnel reflectance
τ_a	Aerosol optical thickness
μm	micrometer
μW	microWatts
θ_s	Sun zenith angle
θ_v	Satellite view angle
ω_0	Single scattering albedo
a_c	Absorption coefficient of chlorophyll-a
a^*_c	Specific absorption coefficient of chlorophyll-a
a_{CDOM}	Absorption coefficient of CDOM
$a_{CDOM}(440)$	Absorption coefficient of CDOM at 440 nm
a_s	Absorption coefficient of TSM
a^*_s	Specific absorption coefficient of TSM
a_w	Absorption coefficient of pure water
a_{c_nor}	Normalised absorption by chlorophyll-a
a_{s_nor}	Normalised absorption by suspended sediment
a_{CDOM_nor}	Normalised absorption by CDOM
b	Total scattering coefficient`
b_b	Total backscattering coefficient
c	Velocity of light
C_c	Chlorophyll-a concentration
C_s	Suspended sediment concentration
D	Julian day
E_d	Downwelling irradiance
E_s	Surface irradiance
f	Surface area of filter paper for TSM analysis
F_s	Extra-terrestrial irradiance at the top of atmosphere
F_0	Average Extra-terrestrial irradiance for a year
h	Planck's constant
k_d	Downwelling diffuse attenuation coefficient
L_a	Aerosol radiance
L_g	sun glint
L_p	path radiance from aerosol and Rayleigh scattering

L_r	Rayleigh radiance
L_u	Upwelling radiance
L_w	water leaving radiance
nm	nanometre
OD_c	Corrected OD for chlorophyll
OD_f	OD of total suspended matter
OD_s	Corrected OD of total suspended matter
P_x	Phase function
R_{rs}	Remote sensing reflectance
s	Slope coefficient for CDOM
sr	Steridian
t	Direct transmittance
T_d	diffuse transmittance
TD	Number of days in a year
V	Volume of water filtered

Chapter 1.
Introduction

1.1 General Introduction

Oceans cover the major portion of the earth's surface. Despite that, immediate human interaction with the marine environment occurs in coastal water bodies that dominate the daily affairs of mankind. Consequently, anthropogenic activities in the coastal regions exert high pressure on the coastal and estuarine ecosystems (Hallegraeff, 1993) owing to transport of material through the estuarine channels, disposal of effluents from the industries, sewage dumping, coastal constructions, ports and oil spills from ships and boats. Globally, most of the human settlements are situated along the banks of the estuaries and coasts (Miller *et al.,* 2005). Over 50% of the human population lives in the coastal zones. Thus, the fact that coastal oceans and estuaries are an indispensable part of human life renders them highly vulnerable to pollution thereby disrupting the natural exchange process between freshwater and sea water. This necessitates regular and effective monitoring of the coastal ecosystems on a global scale (Kostadinov *et al.,* 2007). Concerns about increased turbidity and its impact on coastal and estuarine environments have encouraged efforts to relate satellite observations to in-situ properties of light attenuation in the water column (Stumpf and Pennock, 1991). Resourceful monitoring tools can thus be developed for the estuaries and coastal zones using optical remote sensing (Siegel *et al.,* 1999; Voss *et al.,* 2000). Remote sensing technique provides a synoptic coverage and has the ability to monitor large-scale trends and variability of water quality parameters through optical signatures of the water column (Sathyendranath, 2000). The optical signatures in the visible region of the Electromagnetic Radiation (EMR) from the open ocean are simple as the only factor affecting them is the phytoplankton, which possess Chlorophyll-a pigment. However, in the coastal and estuarine waters the

1

optical signature is a complex mixture of signals from optically active constituents (OAC) such as chromophoric dissolved organic matter (CDOM), total suspended matter (TSM) (both in-situ and land-derived) and phytoplankton Chlorophyll-a. The composition of such waters varies from region to region (Kratzer *et al.*, 2000). This necessitates the development of site-specific algorithms to retrieve OAC from satellite sensors with application limited for particular region (Sathyendranath, 2000; Darecki *et al.*, 2003). The use of remote sensing for precise studies in these regions necessitates careful delineation of the optical signatures leaving the water column. Thus, the optical characterization of the water column is vital in facilitating retrieval of appropriate information from remotely sensed data of optically complex waters (Sathyendranath *et al.*, 1989; Tassan, 1994).

1.2 Literature Review

Ocean optics or optical oceanography has long since gained significance as a special branch of oceanography. In-water optical measurements date back to 1885 when Fol and Sarasin used photographic plates in the Mediterranean off the Cote d'Azur (Jerlov, 1976). Spectral radiances were measured at different depths in the sea by Knudsen (1922). Optical technique was revolutionised with the introduction of photoelectric cells for marine observations (Shelford and Gail, 1922). In 1930's, substantial pioneering work was done on the design and use of radiance and irradiance meters (Atkins and Poole, 1933; Clarke, 1933; Jerlov and Liljequist, 1938; Takenouti, 1940; Whitney, 1941). Shuleikin (1923, 1933) correctly explained the colour of the sea and carried out quantitative analysis of the structure of the light field in turbid media. Important results pertaining to the effect of yellow substance on the

2

transmission of light and colour of the sea were obtained by Kalle (1938). Gershun (1936, 1939) propounded a general theory for the light fields and introduced new photometric concept: scalar irradiance. The development has continued and highly improved modern technology has introduced hyperspectral radiometers, fluorometers, scattering, absorption and attenuation meters. Underwater optics has wide applications in oceanography as a precursor to ocean remote sensing, in view of which, characterisation of water bodies by means of their optical properties has gained immense importance.

Optical properties of a water body are largely determined by various dissolved and particulate substances present therein. Based on the above, the oceanic waters are broadly categorised as Case 1 and Case 2 waters (Morel and Prieur, 1977). The Case 1 waters are typically the open ocean waters. By definition, the optical properties of Case 1 waters are a function of phytoplankton and their co-varying derivative products. However, this does not rule out the possibility of substances other than phytoplankton affecting the optical properties of these waters. In fact, the absorption characteristics can be altered by biological debris generated by grazing and decay of phytoplankton organisms and chromophoric dissolved organic matter (CDOM) liberated from biological particles, thus altering the optical properties of Case 1 waters (Sathyendranath and Morel, 1983). It is also known that small organisms such as flagellates, heterotrophic bacteria and viruses, which co-exist with phytoplankton, play an important role in determining some optical properties of Case 1 waters (Morel and Ahn, 1991; Stramski and Kiefer, 1991; Ulloa et al., 1992). Therefore, it does not mean that phytoplankton are the only agents responsible for the colour of Case 1 waters. However, contribution from other substances, if present, is relatively small in Case 1 waters, and can be modelled as a function of phytoplankton concentration.

The Case 2 waters include the coastal and estuarine waters wherein the dominant factor affecting the optical properties of the water column is not phytoplankton but other particulate matter or dissolved organic matter or both make a significant contribution to the optical properties (Sathyendranath, 2000). Furthermore, these contributions are not linked to the phytoplankton concentration but they act as independent variables.

A pictorial representation of the two cases adapted from Prieur and Sathyendranath (1981) is given below.
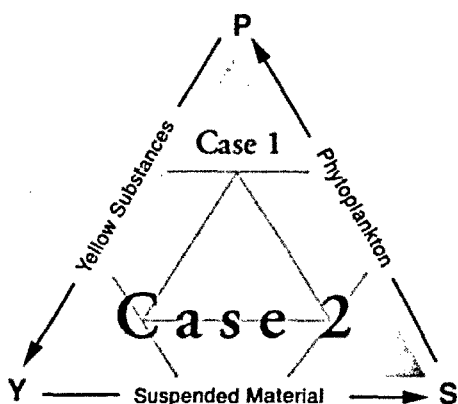
Fig. 1.1 Diagrammatic representation of Case 1 and Case 2 waters adapted from Prieur and Sathyendranath (1981) (see also Morel and Antoine, 1997; Dowell, 1998).

The triangular classification of oceanic waters into Case 1 and Case 2 (Fig. 1.1) is based on relative contribution of the three components of OAC and not the concentration of the individual component. This classification scheme can be used as a simple device to differentiate waters where phytoplankton-related signals dominate the signal from more optically-complex water bodies.

The optical signatures acquired from either the optically simple or complex waters can be used to gather information about the nature of the OAC prevailing in the water column.

Optical remote sensing of the oceanic waters was developed as a science by Gordon (Gordon and McCluney, 1975; Gordon and Morel, 1983; Gordon *et al.*, 1988)

by using the Coastal Zone Colour Scanner (CZCS) to retrieve Chlorophyll-a concentration from Case 1 waters. The CZCS was the first ocean colour sensor launched on Nimbus 7 satellite in 1978 with 4 bands in the visible spectrum of EMR. This was the pioneering step in gathering information about oceanic waters remotely. A simple blue to green band-ratio algorithm was used to deduce Chlorophyll-a concentration from recorded water leaving radiance values (Morel and Prieur, 1977; Sathyendranath et al., 1987). This paved the way for further research in optical remote sensing of oceanic waters. Significant efforts have been made in the recent past to develop ocean colour satellite missions with improved spectral and radiometric performance, spatial and temporal coverage, and quality of data products (Morel, 1988). This has led to the launching of various ocean colour sensors such as MOS (Marine Observation Satellite), OCTS (Ocean Colour and Temperature Scanner), POLDER (The POLarization and Directionality of Earth Reflectances), SeaWIFS (Sea viewing WIde Field of view), MODIS(MODerate resolution Imaging Spectroradiometer), OCM (Ocean Colour Monitor), MERIS (MEdium Resolution Imaging Spectroradiometer) andOCM2 of which, SeaWIFS and MODIS have been immensely used to map Chlorophyll-a concentration on a global scale over Case 1 waters. Over 90% of the oceanic waters are Case 1 (Darecki and Stramski, 2004). The current satellite operational algorithms for the retrieval of pigments and other bio-optical properties have been empirically derived from field data collected mainly from ocean waters that are categorised as Case 1 (O'Reilly et al., 1998, 2000; Darecki and Stramski, 2004) and are based on the fact that the optical properties behave as a function of phytoplankton Chlorophyll-a. However, in Case 2 waters, the OAC vary independently of phytoplankton and each other (Bouman et al., 2000). Such complexity in the optical properties of Case 2 waters results in inadequacy in

Chlorophyll-a based single-variable optical models and failure of standard algorithms used for Chlorophyll-a retrieval from satellite data (Sathyendranath, 2000). Hence, new algorithms based on new approaches for dealing with both atmospheric correction (since the NIR bands in the Case 2 waters receive signal from the water column in highly turbid waters) and retrieval of ocean bio-optical properties from water-leaving radiance in Case 2 waters are required (Sathyendranath, 2000). Remote sensing of Case 2 waters imposes additional demands on the sensor as the relationship between the concentrations of aquatic constituents and ocean colour is nonlinear, and often small changes in the signal have to be removed to retrieve useful information. This implies that instruments with a high signal-to-noise ratio are required. The proximity to land and the possibility of encountering highly-reflective waters raises the need for sensors with a high dynamic range (Sathyendranth, 2000). Overall, remote sensing of Case 2 waters has more stringent requirements than for Case 1 waters. Several new ocean-colour sensors (MODIS, MERIS, OCM (1 and 2)) meet the requirements for Case 2 waters to a much higher degree than the CZCS. The improved prospects for dealing with Case 2 waters have led to studies for developing algorithms for remote sensing of Case 2 waters.

One of the major drawbacks in the remote sensing of Case 2 waters is that a single algorithm cannot be applied over different regions. A greater number of variables influence the measured spectra in Case 2 waters and this implies the necessity of specific algorithms to account for the multivariate characteristics. Because of overlapping absorption and scattering spectra of the OAC, variations in radiance (or reflectance) cannot be related directly to any one component and hence all components have to be solved simultaneously. Inherent optical properties (IOP) of different waters are also impacted by seasonal changes and this requires algorithms

that account for the local and seasonal variations. This implies that no single, global algorithm for Case 2 waters would work equally well in all regions. Another factor is the geographical variability in the species of the OAC, for e.g., the phytoplankton species vary greatly from region to region. Further, mineral particles (their source, size and shape) play a major role in altering the optical signatures of the water column (Morris and Howarth, 1998; Ferrari *et al.*, 2003). It is thus clear that Case 2 waters require more complex and sophisticated algorithms than those developed for open-ocean (Case 1) waters. Recent efforts have resulted in site-specific algorithms to derive OAC (Froidefond *et al.*, 1991; Uncles *et al.*, 2001; Doxaran *et al.*, 2002a, 2002b, 2003, 2005; Menon *et al.*, 2006; Petus *et al.*, 2010).

1.3 Objectives

It is evident from the above that a detailed study of the optics of the Case 2 water column is a pre-requisite for developing site-specific algorithm. The study of reflectance offers an insight on the optical complexity of the water column as it is affected by all the OAC (Doxaran *et al.*, 2002a; Schofield *et al.*, 2004; Tzortziou *et al.*, 2007). In India, there is no record of optical properties of estuaries until recent past. Only two estuaries in Goa along the west coast have been surveyed once for optical properties in 2002 with a multi-spectral radiometer and covered a total of only 10 stations in both Mandovi and Zuari estuaries (Menon *et al.*, 2005, 2006). However, a detailed seasonal and spatial study pertaining to optical complexity of the estuaries has not been documented till date. Hence, the present research work was proposed with the following objectives.

a) To study the inherent and apparent optical properties (IOP and AOP) of the Mandovi - Zuari estuarine system seasonally and to check the feasibility of using the data to develop algorithm to retrieve optically active constituents (OAC) through optical sensor.

b) To analyse the variability of aerosol optical characteristics over the study area so as to apply atmospheric correction to remotely sensed data.

c) To study the hydrographic characteristics of Mandovi - Zuari estuarine system during pre-monsoon and post-monsoon and to examine the feasibility of analyzing the estuarine dynamics through ocean colour analysis.

d) To examine the feasibility of using CDOM as a proxy to salinity to retrieve it through an ocean colour sensor.

Chapter 2.

Study Area and Data

2.1   Study Area

The Mandovi – Zuari estuarine system (Fig.2.1) of Goa along Central West coast of India, a complex system affected by mining transports was selected for the study.
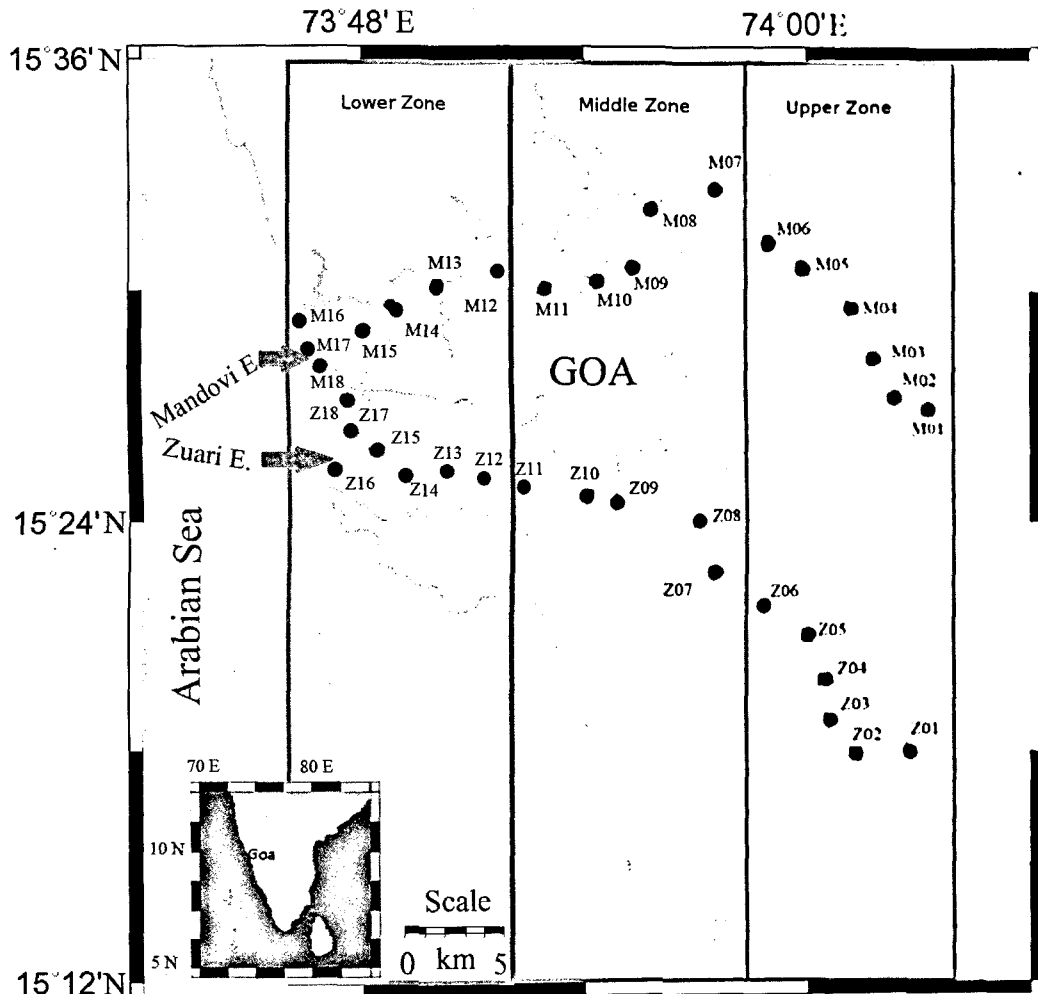
Fig 2.1 Study Area map showing sampling stations and the three zones.

2.1.1   General Background

The west coast of India is characterized by the Western Ghats (the Sahyadris). The Sahyadris are called 'ghats' owing to their characteristic steep and terraced hills

made of horizontally bedded lavas that run parallel to the coastline and have taken a distinctive landing stair shape (Wadia, 1975). The average height of these hills is about 900 m. The western coastal plain and the western slopes of the Sahyadris receive more than 2 m rainfall and are one of the highest rainfall receiving regions in India. Most of the rain is received during the summer monsoon (June – September). The estuarine network forms an important conduit to carry the runoff that flows from the Sahyadris and the coastal plain to the Arabian Sea. During monsoon, the water level in the upstream region of the estuaries is controlled by fresh water, whereas tidal influence is the dominating driving mechanism for transport in the estuarine network in the non-monsoon period. The oceanographic processes differ between monsoon season, when the freshwater flow is high and the dry season, when the runoff is negligible and tide dominates the circulation and mixing within the estuaries. The water level in the downstream region of the estuaries is always under tidal control. Such monsoonal estuaries are found all along the West coast of India. The Mandovi and Zuari estuaries along with Cumbharjua canal form one such estuarine system along the West coast of India.

2.1.2 Mandovi – Zuari Estuarine network

Mandovi – Zuari estuarine network, situated in Goa along the west coast of India, is one of the most complex ecosystems. The latitude 15°25' N to 15°31' N and longitude 73°45' E to 73°59' E form the geographic margins of this network (Fig. 2.1). Both the rivers originate in the Western Ghats and meet the Arabian sea. The length of Mandovi and Zuari rivers is 75 km and 70 km respectively. The Mandovi and Zuari estuaries are coastal plain estuaries as they are located on the alluvial plains between

Sahyadris and the Arabian sea. The estuarine system is characterized by heavy rainfall during the Southwest monsoon. About 80% of the total rainfall received by Goa (average 3000 mm) occurs during the Southwest monsoon (Qasim and Sengupta, 1981). During this season, both the estuaries receive large volumes of land runoff from the catchment areas of Mandovi basin (1895 km^2; Suprit and Shankar, 2008) and Zuari basin (550 km^2; Qasim, 2003). Mandovi has many tributaries compared to Zuari and receives greater runoff. The catchment area is mountainous and composed of Western Dharwar Craton with gneissic and schistose rocks and ferruginized lateritic cappings (Naqvi, 2005).

The Cumbharjua canal connecting the two estuaries is about 17 km long and 0.5-0.7 km wide. The width at the mouth of Mandovi is about 3.2 km and at the widest region, near Aguada, it is 4 km. Beyond the bay region, the width of the estuary decreases to 0.25 km upstream. The wider segment at the mouth of Mandovi is known as the Aguada bay and the average depth of the bay is about 5 m. The width of Zuari at the mouth is about 5.5 km. The 10 km stretch upstream from the mouth is known as the Mormugao bay and is approximately 5 km wide and 5 m deep. At the upstream end of the Mormugao bay, the width decreases to less than 1 km and the channel narrows further up to about 0.5 km. The depth of the main channels of both the estuaries varies considerably with location, and their cross-sectional area decreases rapidly in the upward direction (Shetye *et al.*, 2007a). Such channels have been described as 'strongly convergent' (Friedrichs and Aubrey, 1994). The convergence has important implications for dynamics of tides in the estuarine channels. The spring tides are higher than 2 m and hence both the estuaries are macrotidal. The effect of the tide is seen up to 50 km upstream from the mouth (Shetye *et al.*, 1995). The hydrodynamics of both the estuaries is controlled by both

river runoff and tide during monsoon. During monsoon, due to excess runoff the estuaries get stratified and exhibit salt-wedge type behaviour. After the withdrawal of the monsoon, the runoff decreases rapidly rendering a partially mixed characteristic to the estuaries. The runoff reaches negligible levels by November. Consequently, tidal flow at the mouth of the channel becomes the sole driving mechanism for transport into the estuarine network in the pre-monsoon resulting in fully mixed type estuaries (Murthy *et al.*, 1976; Shetye *et al.*, 1995).

2.1.3 Salinity structure in Mandovi and Zuari estuaries:
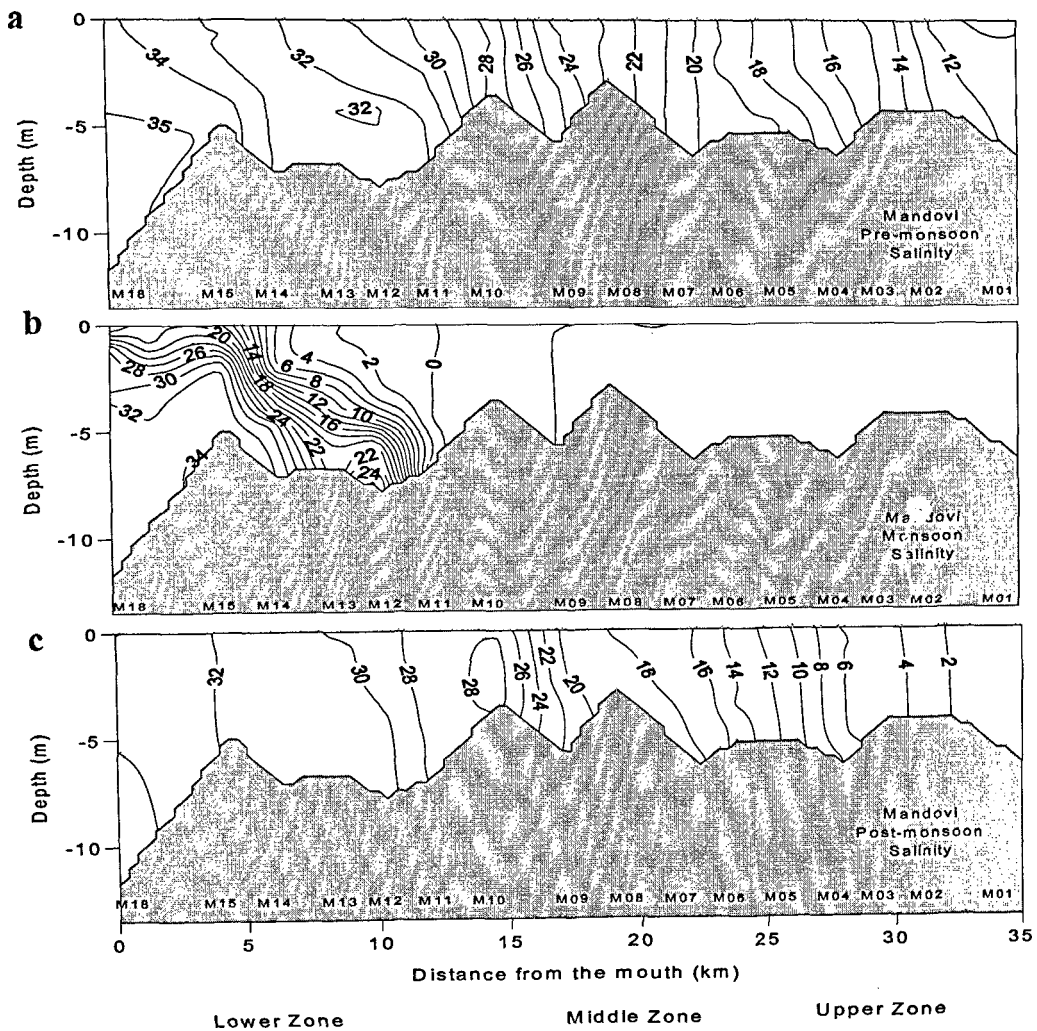
Fig. 2.2 Vertical sections of salinity in Mandovi estuary during a) pre-monsoon, b) monsoon and c) post-monsoon seasons

The vertical section of salinity was documented for December'97 in Mandovi and December'98 for Zuari (Shetye *et al.*, 2007b). This section extended up to 35 km from the mouth and depicted the characteristic of only post-monsoon. Menon *et al.* (2011) had discussed the salinity variability for two seasons (pre-monsoon and post-monsoon) up to 12 km and 14 km from the mouth of both Mandovi and Zuari estuaries respectively. In this study, the salinity sections for all the three seasons are presented to an extent up to 35 km and 40 km in Mandovi and Zuari estuaries respectively.

Fig. 2.2a shows the salinity section of the Mandovi estuary during pre-monsoon season. The salinity was observed to increase gradually from 11 PSU at the upper reaches of the estuary to 35 PSU at the mouth. This range itself was an indication of the strong mixing taking place in the estuary. It was clearly observed that the estuary is vertically homogeneous up to station 12. Towards the mouth however, the partially mixed waters depicted salt-wedge type structure. The fresh water inflow during the pre-monsoon season is very meagre. Thus, the extent of saline intrusion was greater in this season as compared to the monsoon and post – monsoon. It is also interesting to note that the salinity contours are equally spaced throughout the region covered. This was an indication of the seaward mixing which has taken place after monsoon.

Figure 2.2b shows the salinity distribution in Mandovi estuary for monsoon season. It was well evident from the figure that the estuary was transformed into salt-wedge type as large amount of fresh water was brought into the estuary due to the heavy monsoonal rains in this season. It was observed that the Mandovi estuary was filled with fresh water up to lower zone, beyond which the mixing takes place

forming salt-wedge in the lower zone. The salinity increases from 0 PSU to 34 PSU. The surface salinity at the mouth was 20 PSU.

The post-monsoon season again showed a vertically homogeneous salinity structure (Fig 2.2c). However, the salinity (2 PSU – 32 PSU) was lower than in the pre-monsoon season. This was the effect of the fresh water flow which slowly decreased from monsoon. The salinity in the upper zone increased slowly as the fresh water flow decreased and became negligible in pre-monsoon.
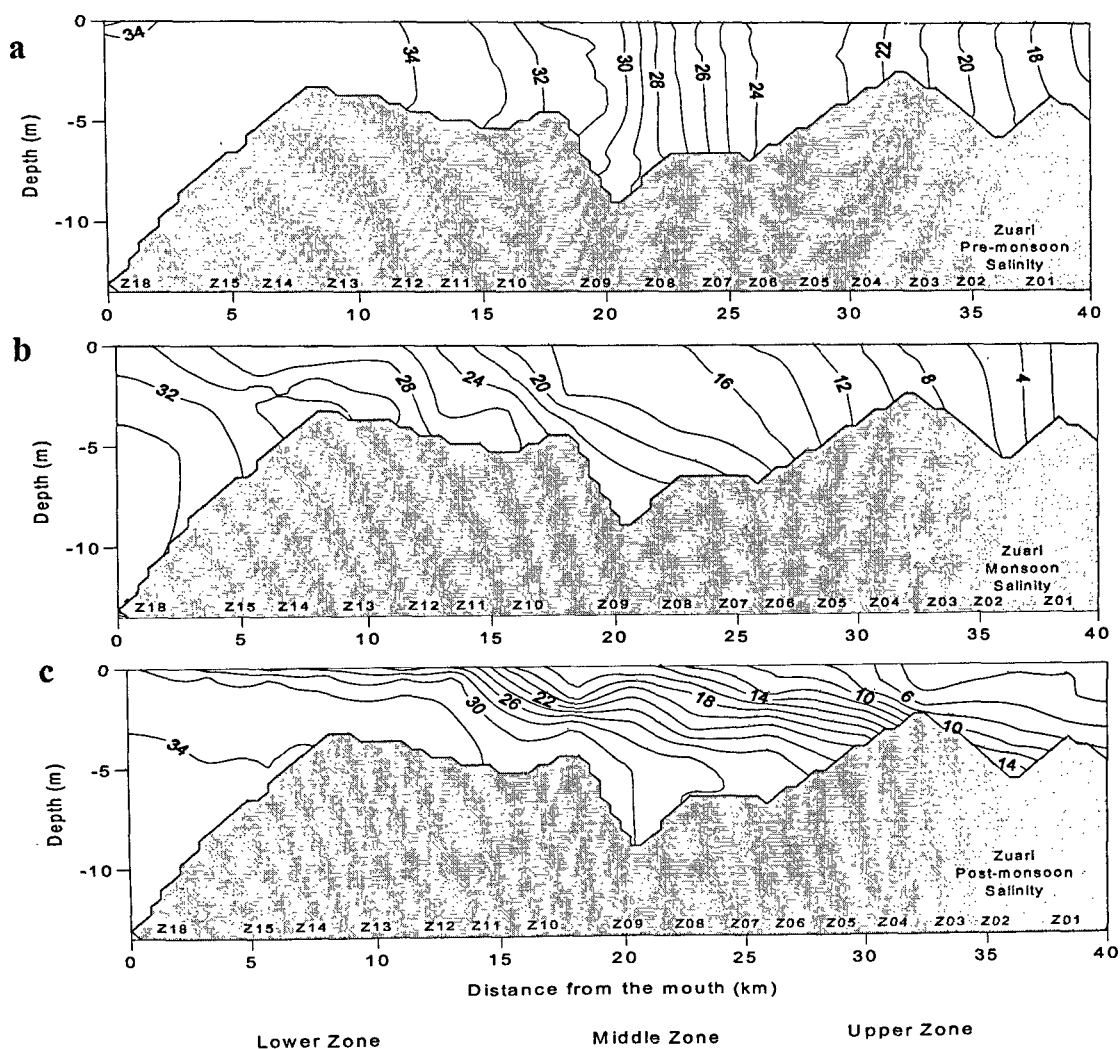
Fig. 2.3 Vertical sections of salinity in Zuari estuary during a) pre-monsoon, b) monsoon and c) post-monsoon seasons.

Fig. 2.3a shows the salinity distribution in the Zuari estuary for pre-monsoon season. A vertically mixed characteristic was observed throughout the Zuari estuary. The salinity increased from 17 PSU at the upper reaches of the estuary to 34 PSU at the mouth. The Zuari basin at the mouth composed of nearly homogeneous water mass. The salinity at the upper region of the estuary was greater than that of the Mandovi estuary. This was due to lesser fresh water input in the Zuari estuary. Unlike Mandovi estuary, the contours are unevenly spaced. The salinity contours are more closely placed at the middle region as compared to the rest of the estuary.

The salt-wedge observed in Mandovi estuary was not observed in Zuari (Fig. 2.3 b), as it has lesser tributaries and the fresh water flow into the system is lesser than in the Mandovi. The salinity varied from 4 PSU to 32 PSU in this season in the Zuari estuary. Post-monsoon showed a sharp gradient in salinity in the middle zone (Fig. 2.3c) from 15 PSU to 26 PSU. The surface value at the mouth was observed to be between 26 PSU and 30 PSU.

In all the three seasons, the salinity values in Zuari were higher than in Mandovi. This can be attributed to less fresh water flow in the Zuari estuary, although both the estuaries lie in the same latitudinal belt. The seasonal difference in the salinity profiles was well evident and the difference between the two estuaries was also very clear.

Depending on the salinity structure in the two estuaries in pre-monsoon and monsoon seasons, the study area was divided into three zones namely upper-zone (stations M01-M06 and Z01-Z06), middle-zone (stations M07-M12 and Z07-Z12) and lower-zone (stations M13-M18 and Z13-Z18). Hereinafter each region of the estuaries is referred as zone.

2.2 Measurements and Analysis

2.2.1 Sampling Details

Both the Mandovi and Zuari estuaries were surveyed during pre-monsoon, monsoon and post-monsoon seasons onboard a trawler along the fairway channel. The sampling was carried out at pre-determined stations in the two estuaries (Fig. 2.1). The details about the dates and duration of the surveys and in-situ measurements are summarized in Table 2.1.

Table 2.1 Details of the field survey and in-situ measurements in Mandovi – Zuari Estuarine region
(Observations column shows measurements (properties derived provided in parentheses)) Notation: W – Water Sample, S – Sunphotometer, C – CTD, R – Radiometer, IOP – Inherent Optical Properties, AOT – Aerosol Optical Thickness, T – Temperature, Sa – Salinity, AOP – Apparent Optical Properties.

Estuary	Date	No. of Stations	Observations
Mandovi – Zuari	12-02-05	14	W (IOP), S (AOT), C (T, Sa)
Mandovi – Zuari	18-03-05	18	W (IOP), S (AOT), C (T, Sa)
Mandovi – Zuari	11-05-05	18	W (IOP), S (AOT), C (T, Sa)
Mandovi – Zuari	15-08-05	17	W (IOP), S (AOT), C (T, Sa)
Mandovi – Zuari	17-09-05	16	W (IOP), S (AOT), C (T, Sa)
Mandovi – Zuari	11-11-05	20	W (IOP, Sa), S (AOT)
Mandovi – Zuari	13-12-05	22	W (IOP, Sa), S (AOT)
Mandovi	29-02-08	17	W (IOP), S (AOT), C (T, Sa), R(AOP)
Zuari	06-03-08	13	W (IOP), S (AOT), C (T, Sa), R(AOP)
Zuari	28-08-08	15	W (IOP), S (AOT), C (T, Sa), R(AOP)
Mandovi	23-09-08	17	W (IOP), S (AOT), C (T, Sa), R(AOP)
Zuari	07-10-08	16	W (IOP), S (AOT), C (T, Sa), R(AOP)
Mandovi	13-11-08	16	W (IOP), S (AOT), C (T, Sa), R(AOP)
Zuari	22-02-11	18	W (IOP), S (AOT), C (T, Sa), R(AOP)
Mandovi	24-02-11	18	W (IOP), S (AOT), C (T, Sa), R(AOP)
Zuari	19-08-11	14	W (IOP), S (AOT), C (T, Sa), R(AOP)
Mandovi	23-09-11	12	W (IOP), S (AOT), C (T, Sa), R(AOP)
Zuari	25-12-11	18	W (IOP), S (AOT), C (T, Sa), R(AOP)
Mandovi	27-12-11	16	W (IOP), S (AOT), C (T, Sa), R(AOP)

All the in-situ observations and collection of water samples were carried out during cloud-free days (except during the monsoon season where instances of passing clouds cannot be avoided). The sampling was done at locations where the total depth of the water column was greater than three times the Secchi disk depth. This precaution was taken to avoid radiance from the bottom of the station (Muller and Austin, 1995) that would affect the satellite retrieval of the data.

2.2.2 In-situ measurements

The optical data were recorded with a Satlantic hyperspectral Radiometer (HyperOCR) with 138 bands in the interval of 349-803 nm. For each optical measurement, SeaBird 19plus CTD (Conductivity, Temperature and Depth), Microtops II Sunphotometer with 5 bands (380, 440, 555, 765, 865 nm), hand-held Global Positioning System (GPS) and Secchi disk were also operated and water sample was collected using Niskin Sampler to analyse Chlorophyll-a, CDOM and TSM. Atmospheric parameters such as air temperature, atmospheric pressure, relative humidity and wind speed and direction were obtained from Automatic Weather Station (AWS) installed at the Goa University during estuarine surveys.

The thesis consists of chapters dedicated to different aspects related to optical properties, atmospheric correction and satellite retrieval of salinity. To analyse each aspect, the data sets required are different. Hence, this chapter describes the general methodology, while the methodologies dealing with specific components have been explained in the respective chapters.

A. In-water Radiometer

The HyperOCR has three basic sensors for measuring profiles of upwelling radiance ($L_u(\lambda, z)$), downwelling irradiance ($E_d(\lambda, z)$) and solar irradiance reaching the sea surface ($E_s(\lambda)$). It has auxiliary sensors for depth and temperature and an attached WetLabs fluorometer that estimates Chlorophyll-a concentration using Chlorophyll-a fluorescence. The surface irradiance sensor (E_s) was tied on the deck of the trawler at a position unaffected by shadows during the radiometer operation. The radiometer was operated from along the side of trawler facing the sun to avoid the shadow cast by the trawler itself. In addition, care was exercised to deploy it as far as possible from the trawler to avoid the shadow from the trawler bottom. It was operated up to euphotic depth (the depth at which 1% of surface PAR is encountered) or the total depth (minus 1-2 m to avoid abrasion to the instrument), whichever was encountered first. The recorded data was processed using the software Prosoft 7.7.10 supplied by the manufacturer.

Various parameters derived from the radiometric measurements of L_u, E_d and E_s were photosynthetically active radiation (PAR), Remote sensing reflectance (R_{rs}) and diffuse attenuation coefficient (k_d). The details are given in Chapter 3.

B. Sunphotometer measurements

The spectral aerosol optical thickness (AOT) was measured using a hand-held Microtops II Sunphotometer during the field surveys at all the cloud-free stations. It has five bands (380, 440, 500, 675 and 870 nm) and measures AOT with a full field of view of $2.5°$. The instrument calculates AOT at each wavelength based on the energy

received at the target, its calibration constants, atmospheric pressure, time and position of observation. It has a built-in pressure sensor to measure the atmospheric pressure, which is mainly used to compute Rayleigh radiance. A hand-held GPS is interfaced with the sunphotometer to give the accurate measure of time, position and solar zenith angle.

Through spectral analysis of AOT, aerosol size index (Ångström wavelength exponent, α) and Ångström turbidity factor (β) were derived. Further, aerosol path radiance (L_a) and Rayleigh path radiance (L_r) were estimated using AOT and atmospheric pressure, respectively. The L_a and L_r were used to apply atmospheric correction to OCM data. The details are given in Chapter 4.

C. CTD measurement

A SeaBird SBE 19plus CTD was used to obtain temperature and salinity profiles at each station. The CTD was cast till the maximum depth of the water column and operated from the sunlit side of the sampling vessel. The data was binned at an interval of 0.25 m and the contours were then plotted using Surfer version 8.4.

2.2.3 Water sample analysis and generation of inherent optical properties

The Chlorophyll-a was estimated as per Strickland and Parsons (1972). The CDOM analysis was carried out as per Kowalczuk and Kaczmarek (1996). TSM analysis for concentration was carried out as per Gardner et al. (1989) and REVAMP protocols (Tilstone et al., 2002), and the absorption coefficient analysis was carried

out using filter pad technique (Cleveland and Weidemann, 1993; Tassan and Ferrari, 1995). The detailed procedure is explained in Chapter 3.

2.2.4 Satellite Data processing

The satellite data used for the present study was the IRS-P4-OCM (Indian Remote Sensing Satellite – PSLV 4 – Ocean Colour Monitor) data. It was procured from the National Remote Sensing Centre (NRSC), Hyderabad. The sensor OCM was launched onboard IRS – P4 satellite in 1999 in a sun-synchronous polar orbit at an altitude of 720 km. It passes the equator at local noon (±20 min). This nullifies the effect of the sun zenith angle in the recorded data for which correction has to be applied otherwise. The OCM has 8 bands, 6 in visible and 2 in NIR. The details of the sensor are summarized in the table below.

Table 2.2 Table showing specifications of the Ocean Colour Monitor (OCM)

Parameters	Specifications	
Spatial Resolution	360 x 250 m	
Swath	1420 km	
No. of Spectral bands	8	
Spectral range	402 – 885 nm	
Revisit time	2 days	
Spectral Band	Central wavelength (bandwidth) in nm	Saturation radiance ($\mu W/cm^2/sr/nm$)
C1	412 (20)	35.5
C2	442 (20)	28.5
C3	489 (20)	22.8
C4	512 (20)	25.7
C5	557 (20)	22.4
C6	670 (20)	18.1
C7	768(20)	9.0
C8	867 (20)	17.2

The OCM data of 12th January, 12th February, 18th March, 13th April, 11th May, 17th September, 9th October, 11th November and 09th December 2005 were used in the present study. The data were processed using ERDAS Imagine 8.4. The OCM data is provided in 16-bit binary format. In addition to the above, a LEADER.OCM file is supplied with the data. This file contains data information about image record length, number of rows and columns of the image, line header bytes and file header bytes required to import data. The geometric correction was then performed using Ground Control Points (GCP). The scene input and reference coordinates were taken in the file LEADER.OCM. The coordinates were given in terms of Longitude and Latitude corresponding to pixel and scan of the image. The geometric correction was performed as polynomial with a suitable polynomial order and the images were then projected as 'Geometric Lat / Long'. Subsequently, land masking was done to highlight ocean features. For masking the land, binary masking scheme was adopted (Assign, Land=0 and Ocean=1). Then, the digital numbers (DN) were converted into radiance by dividing the DN values by different constants corresponding to different bands. The unit of radiance values was $\mu W/cm^2/nm/sr$. Subsequently, atmospheric correction was applied to different pixels of each visible band by subtracting aerosol radiance (L_a) and Rayleigh radiance (L_r) computed from in-situ measurements. The details are given in Chapter 4. Further, the retrieval algorithm was applied to generate CDOM and salinity. The images were then classified and composed into a map.

Chapter 3.

Bio-optical properties of estuarine waters and the

associated light climate

The bio-optical properties of a water column consist of the absorption (a), scattering (b) characteristics, diffuse attenuation coefficient (k_d) and remote-sensing reflectance (R_{rs}) mainly due to the optically active constituents (OAC) (Chlorophyll-a, chromophoric dissolved organic matter (CDOM) and total suspended matter (TSM)) (Sathyendranath *et al.*, 2000). The presence of the three OAC with overlapping optical properties led to the classification of coastal and estuarine waters into Case 2 waters (Morel and Prieur, 1977). The optical characterisation of these waters can be dealt with more accurately if the optical properties are available in high resolution. These parameters can either be derived from water sample analysis or from radiometer and absorption-attenuation meters. The downwelling diffuse attenuation coefficient (k_d) can be considered as a measure of water quality as attenuation coefficients do not vary much if the composition of the water remains fairly constant (Baker and Smith, 1979). R_{rs}, an AOP, is the ratio of L_u to E_d (two AOP), fairly depends on two IOP, absorption (a) and back scattering (b_b)

The remote sensing reflectance helps in understanding both absorption and scattering and therefore, can be used as a single property to characterise a water body. The Remote sensing reflectance (R_{rs}), the spectral signature, is the measure of the colour of the water column, which indicates the water type and is widely used for classification of the water types (Szekielda *et al.*, 2003). It is imperative to study the IOP derived from water samples to enable the understanding of its effect on R_{rs} variability. Hence, this chapter deals with the results of an attempt to understand the optical nature of the water using the data derived from both radiometer and water sample analyses.

3.1 Water sample analyses and generation of inherent optical properties (IOP) through spectrophotometric measurements

3.1.1 Chlorophyll-a estimation:

Chlorophyll-a was estimated as per Strickland and Parsons (1972). During the field survey, the samples were collected and filtered on the trawler, using 0.45μm Millipore glass fibre filters. 1 ml of Saturated $MgCO_3$ was spread on the filter paper at the end of the filtration to prevent biodegradation. The filter paper was crushed, soaked in 90% acetone and kept in dark at low temperature for 20-24 hours for pigment extraction. Subsequently, the chlorophyll-a extract was centrifuged at 3000 r.p.m. for 10-15 minutes and its volume was made to 10 ml by adding 90% acetone. The sample optical density (OD) was then measured using Perkin Elmer Lambda 35 UV/Vis Spectrophotometer using 1 cm cuvette in the spectral range 400 nm - 700 nm with an interval of 1 nm against the cell containing 90% acetone as blank.

The chlorophyll-a concentration was then calculated (Strickland and Parsons, 1972) as

$$C_c = 11.6*(OD_c(665))-1.31*(OD_c(645))-0.14*(OD_c(630))*v/V \text{ (ug/l)} \qquad (3.1)$$

Where,

$OD_c(\lambda)=OD(\lambda)-OD(750)$

C_c = concentration of chlorophyll-a

V = volume of extract

V = volume of water filtered

The absorbance for chlorophyll-a was calculated as

$$a_c(\lambda) = 2.303 * ODc(\lambda) *100 \text{ (m}^{-1}) \qquad (3.2)$$

$$a^*_c(\lambda) = a_c(\lambda)/ C_c \tag{3.3}$$

where a^*_c is the specific absorption coefficient of Chlorophyll-a

3.1.2 Total Suspended Matter (TSM) estimation

The Total Suspended Matter (TSM) estimation was carried out by filtering the water samples in the laboratory using pre-weighed 0.45 μm Millipore membrane filter papers (Strickland and Parsons, 1972). Subsequently, the salts collected on the filters were removed by rinsing the filters with 50 ml of distilled water (Van der Linde, 1998). These filters were dried in hot air oven at 70° C for 24 hours (REVAMP protocol, Tilstone *et al.*, 2002). Subsequently, the filters were placed in desiccator for cooling and weighed again to calculate the concentration (C_s) of TSM as,

C_s = weight of the filter after filtration – weight of the filter before filtration (mg/l).

The sample OD (OD_f) was measured in the spectral range 400 nm -700 nm with an interval of 1 nm using filter pad technique (Cleveland and Weidemann, 1993; Tassan and Ferrari, 1995) with pre-combusted glass fibre filter as blank.

The absorption coefficient of TSM (a_s) is given as per Cleveland and Weidemann (1993) and Tassan and Ferrari (1995).

$$a_s(\lambda) = 2.303 \; OD_s(\lambda) / (V/f) \tag{3.4}$$

where, $a_s(\lambda)$ is the absorption coefficient of TSM, 'V' is the filtration volume (m^3) and 'f' is the filtration area (m^2) and OD_s is the corrected OD of TSM given as

$$OD_s(\lambda) = 0.378OD_f(\lambda) + 0.523 \; [OD_f(\lambda)]^2 \tag{3.5}$$

Where, $OD_f(\lambda)$ is the optical density of total suspended particulate matter.

$$a^*_s(\lambda) = a_s(\lambda)/ C_s \tag{3.6}$$

where a^*_s is the specific absorption coefficient of TSM

3.1.3 Chromophoric dissolved organic matter (CDOM) estimation

The CDOM estimation from the water samples was carried out according to the method suggested by Kowalczuk and Kaczmarek (1996). The samples were collected and immediately filtered on trawler using 0.2μm Whatman membrane filters. 0.5 M $HgCl_2$ was added to prevent biological degradation and then stored in dark at low temperature. The OD for CDOM samples was then measured using Perkin Elmer Lambda 35 UV/Vis Spectrophotometer over the spectral range 400 nm to 700 nm with an interval of 1 nm against distilled water as blank. The absorption coefficients were obtained as

$$a_{CDOM1}(\lambda) = 2.303*OD(\lambda)*100 \ (m^{-1}) \hspace{3cm} (3.7)$$

The spectral absorption coefficient was calculated by normalizing with respect to 440 nm (Kowalczuk and Kaczmarek, 1996) using the formula,

$$a_{CDOM}(\lambda) = a_{CDOM}(440)*e^{-s((\lambda-440))} \ (m^{-1}) \hspace{2.5cm} (3.8)$$

Where,

$a_{CDOM}(440)$ is the CDOM absorption measured at 440 nm and 's' is the slope coefficient.

The slope coefficient was determined as slope of linear fit to the function $\ln[a_{CDOM1}(\lambda)]$ for the range 400 nm - 700 nm. Absorption coefficients were corrected for backscattering of small particles and colloids, which passes through filters (Green and Blough, 1994).

$$a_{CDOMcorr}(\lambda) = a_{CDOM}(\lambda) - a_{CDOM}(700)*(\lambda / 700) \hspace{2cm} (3.9)$$

Where,

$a_{CDOMcorr}(\lambda)$ is the corrected absorption at wavelength (λ)

$a_{CDOM}(\lambda)$ is the measured absorption at wavelength (λ) and

$a_{CDOM}(700)$ is absorption at 700 nm.

The magnitude of a_{CDOM} (440) is the index of concentration while the spectral slope (s) is the measure of its composition (Stedmon and Markager, 2003).

Hence, the total absorption, a (λ), by different OAC's is calculated as

$$a\ (\lambda) = a_w\ (\lambda) + a^*_c\ (\lambda).\ C_c + a^*_s\ (\lambda).C_s + a_{CDOM}\ (\lambda)\ [m^{-1}] \qquad (3.10)$$

The subscript $_{w,\ c,\ s}$ and $_{CDOM}$ refer to water molecule, Chlorophyll-a, TSM and CDOM, respectively. The absorption coefficients for water molecules were obtained from Pope and Fry (1997).

3.2 Optically Active Constituents (OAC) concentration and absorption

3.2.1 Chlorophyll-a

3.2.1.1 Temporal and spatial variability of Chlorophyll-a

In Mandovi estuary, the pre-monsoon distribution of chlorophyll-a revealed high concentration (4.69 µg/l) in the upper zone with gradual decrease towards middle and lower zones. However, in Zuari estuary, the middle zone depicted highest chlorophyll concentration (11.15 µg/l at Z10) (Fig. 3.1b) and the lower zone depicted the lowest concentration (0.9 µg/l at Z15). This result was in accordance with the findings of Prabhu Matondkar et al. (2007) who attributed the distribution to presence of freshwater amenable phytoplankton in Zuari estuary in greater abundance than in the Mandovi estuary.

a)

b)
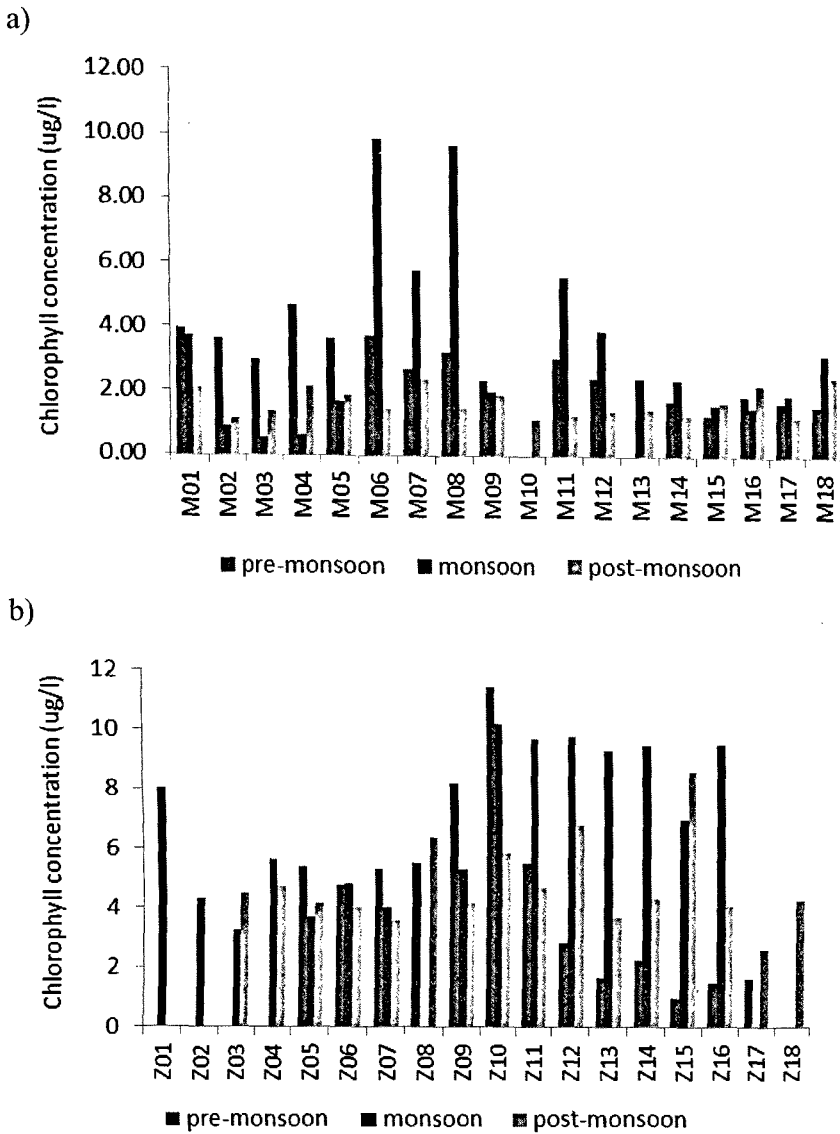
Fig. 3.1 Temporal and spatial variability of Chlorophyll-a in a) Mandovi estuary and b) Zuari estuary

The distribution pattern was different during monsoon season, wherein the maximum concentration (9.8 µg/l) was encountered in the middle zone with low concentration both in upper (0.45 µg/l) and lower (1.75 µg/l) zones in Mandovi estuary. The Zuari estuary depicted high concentration in the upper zone (Z01, 8.1 µg/l), decreased at the middle zone, then increased at Z09 and remained high throughout lower zone (~10 µg/l). Here, again the fresh water phytoplankton showed prominence which could be attributed to the increased freshwater flow during this

27

season. Although, the freshwater flow in Mandovi is four times greater than that in Zuari, the chlorophyll-a concentration is low. The Mandovi estuary supports more euryhaline phytoplankton which displays increased chlorophyll-a with slight decrease in salinity (Prabhu Matondkar *et al.*, 2007). However, that is not the case here as the Mandovi basin is completely filled with fresh water (Fig. 2.2 b) and cannot support euryhaline phytoplankton.

During post-monsoon, Chlorophyll-a concentration didn't vary much between the different zones of both Mandovi and Zuari estuaries. However, the Zuari estuary exhibited higher concentration of Chlorophyll-a than the Mandovi estuary in all three seasons and all three zones.

3.2.1.2 Mean and standard deviation of absorption by Chlorophyll-a ($a_c(\lambda)$).

A) Pre-monsoon.

Fig. 3.2 shows the mean and standard deviation of the absorption by Chlorophyll-a during pre-monsoon. The absorption spectra depict two absorption peaks of Chlorophyll-a (primary peak at 438 nm and secondary at 665 nm). The spectral characteristics remained same for all the three zones in both estuaries. The highest mean was observed at the middle zone in both Mandovi and Zuari estuaries (Fig. 3.2(ii)a and b) and the lowest mean in the lower zone (Fig. 3.2(iii)a and b). However, the standard deviation was highest in the middle zone for Mandovi (Fig. 3.2(ii)a) and lower zone for Zuari (Fig. 3.2(iii)b).

(i)

(ii)

(iii)
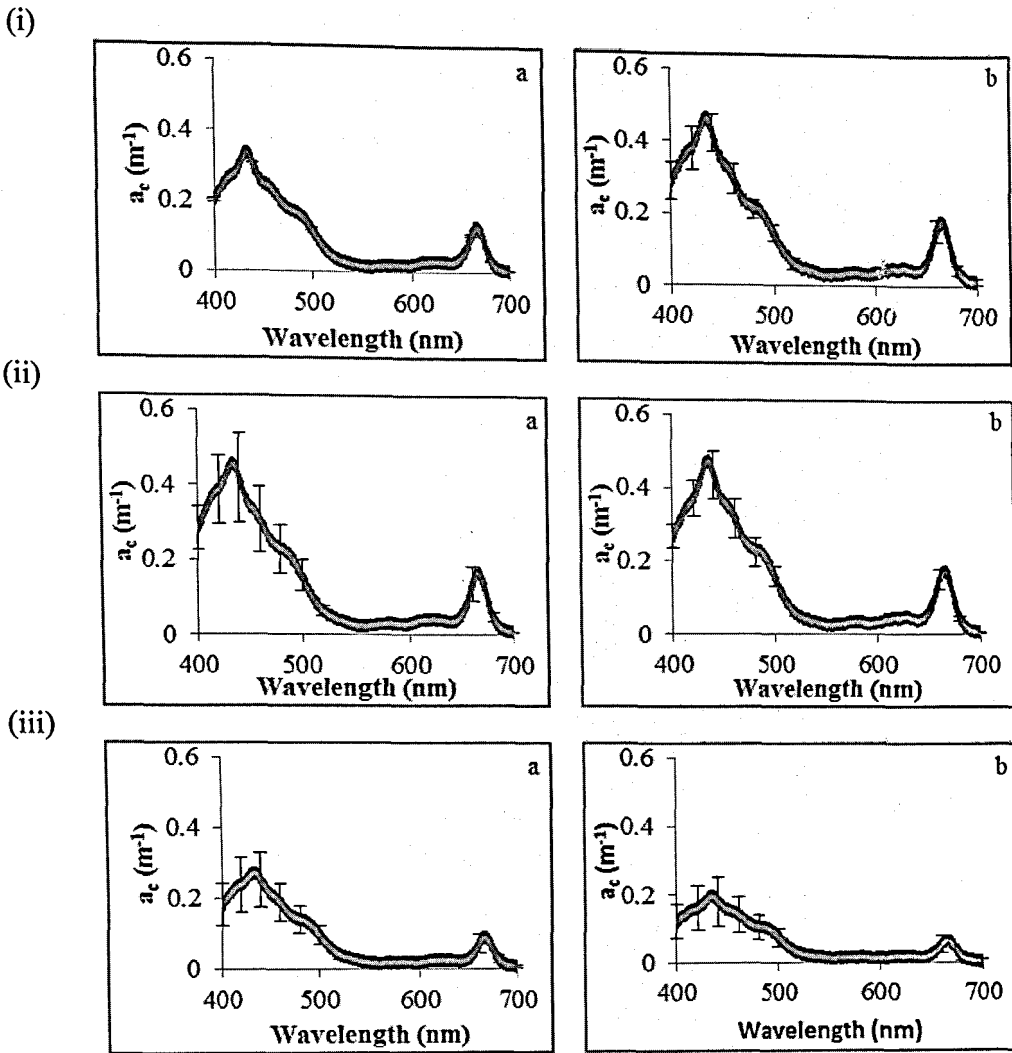
Fig. 3.2 Mean and Standard deviation ofSpectral variation of absorption coefficient $(a_c(\lambda))$ in pre-monsoon at (i) upper (ii) middle and (iii) lower zones of (a) Mandovi and (b) Zuari estuaries

B) Monsoon

The absorption spectra during monsoon season were the same as in the pre-monsoon season. However, there was a large difference between the two estuaries. The mean value for Zuari was observed to be two to three times higher as compared to that for Mandovi. In Mandovi estuary, the absorption values were in a small range between 0-0.15 m^{-1}. In Zuari estuary, the highest mean was observed in the middle zone (Fig. 3.3(ii) b) and lowest in the upper zone (Fig. 3.3(i) b). However, the

standard deviation was found to be the highest in the upper zone (Fig. 3.3(i) b) and the lowest in middle zone (Fig. 3.3(ii) b). To facilitate appropriate comparison, a uniform scale was uniformly maintained. Hence, some graphs exhibited flat spectrum.

(i)

(ii)

(iii)
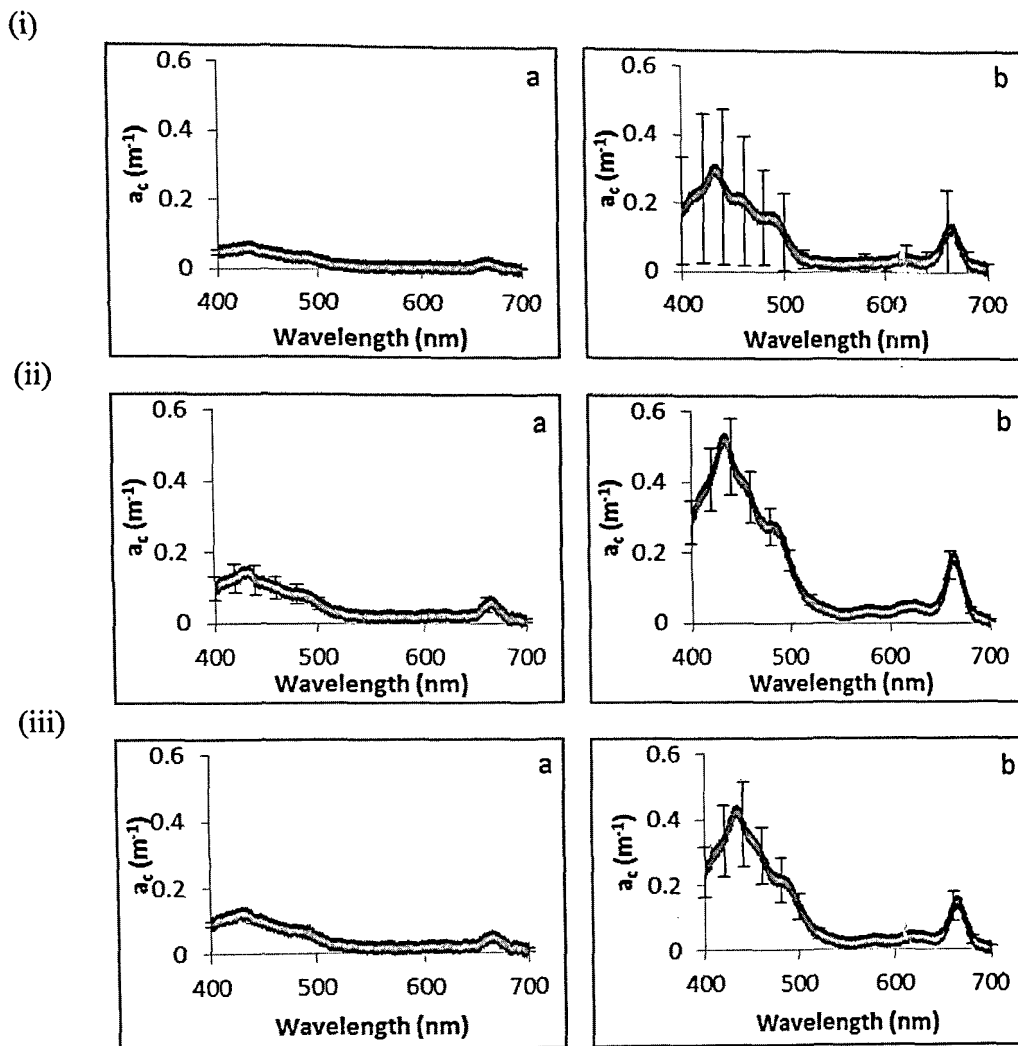
Fig. 3.3 Mean and standard deviation of spectral variation of absorption coefficient of chlorophyll-a $(a_c(\lambda))$ in monsoon at (i) upper, (ii) middle and (iii) lower zones of (a) Mandovi and (b) Zuari estuaries.

C) Post-monsoon

The spectral characteristics of the absorption spectra during post-monsoon season were similar to those observed during the other two seasons. The values were

30

similar in both the estuaries (Fig. 3.4). In Mandovi and Zuari, the highest mean was observed in the upper zone (Fig. 3.4(i) a and b) and lowest in the lower zone (Fig. 3.4(iii)a and b). However, the standard deviation was found to be the highest in the middle zone (Fig. 3.4(ii) a and b) for both the estuaries.

(i)

(ii)

(iii)
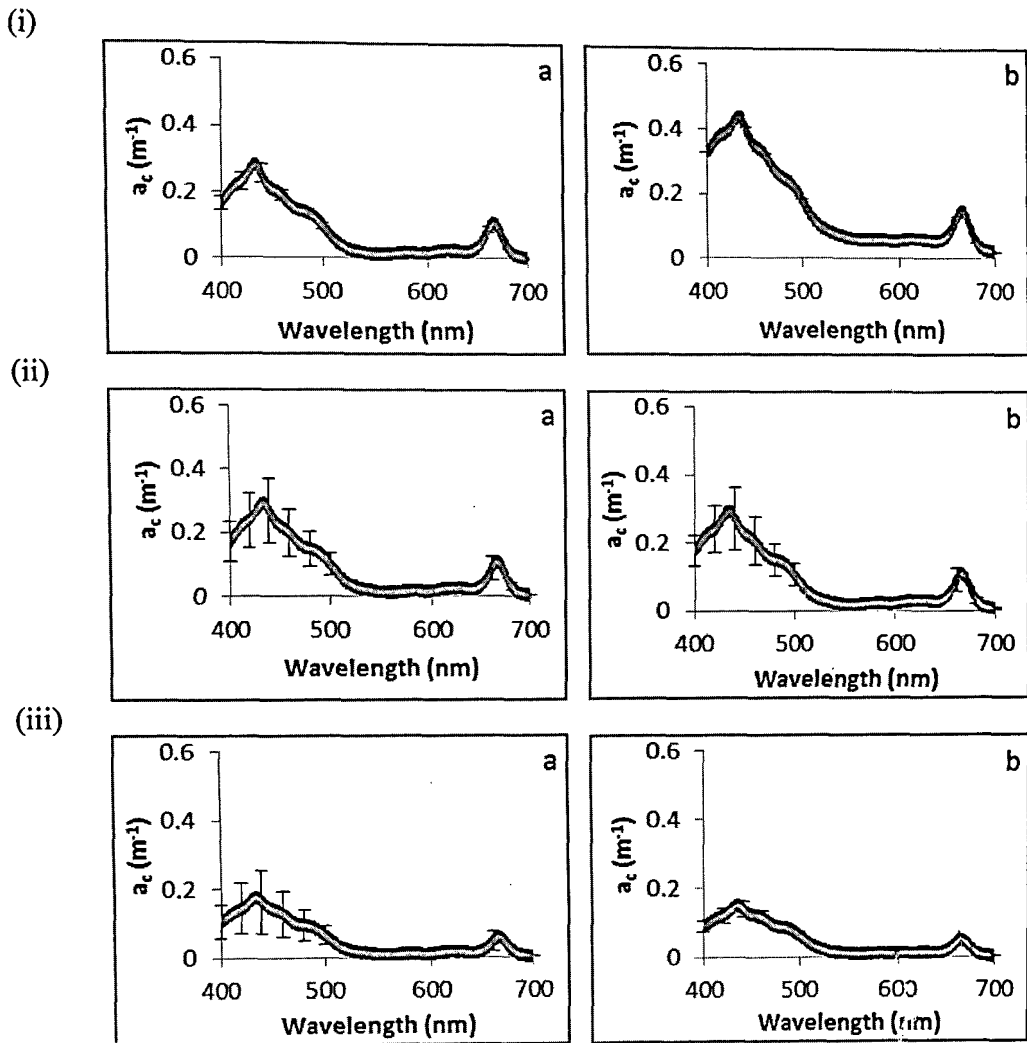
Fig. 3.4 Mean and standard deviation of spectral variation of absorption coefficient of chlorophyll-a (($a_c(\lambda)$)) in post-monsoon at (i) upper (ii) middle and (iii) lower zones for (a) Mandovi and (b) Zuari estuaries

The difference in the magnitude of absorption by Chlorophyll-a was clearly evident between the seasons and the zones.

3.2.2 Total Suspended Matter (TSM)

3.2.2.1 Temporal and spatial variability of total suspended matter (TSM)

The pre-monsoon season depicted low values throughout the estuary (~3-5 mg/l). In Zuari estuary the pre-monsoon season depicted highest values (40 mg/l) in the middle zone and the lowest (5 mg/l) in the lower zone.

a)
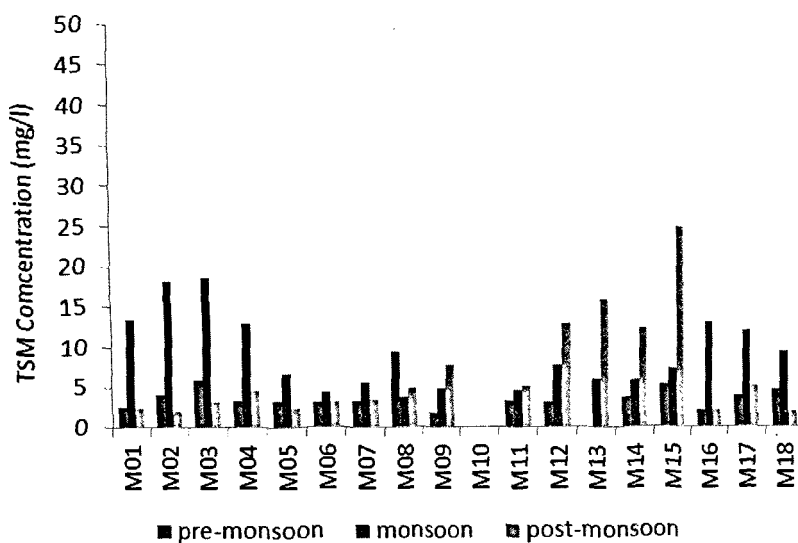
b)
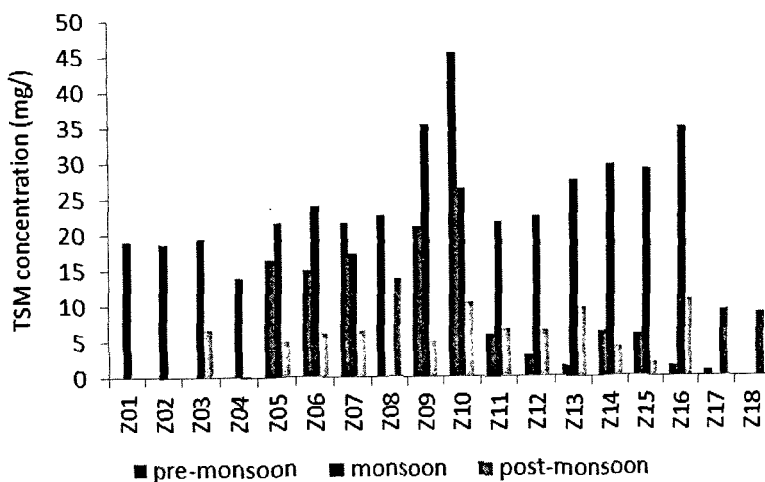
Fig. 3.5 Temporal and spatial variation of TSM in a) Mandovi and b) Zuari estuaries

During monsoon season, maximum TSM concentration (18.6 mg/l) was encountered in the upper zone of the Mandovi estuary (Fig 3.5a). The change in the concentration was such that it decreased from upper zones to middle zone (3.8 mg/l) and further increased to lower zone (13.2 mg/l), resembling a bimodal distribution during this season. The Zuari estuary depicted high concentration throughout the estuary (15 - 35 mg/l) compared to Mandovi with highest concentration of 35.4 mg/l at Z09 and lowest at Z04 (14.8 mg/l) (Fig. 3.5b).

However, the spatial distribution of TSM during post-monsoon in Mandovi estuary depicted an entirely different picture compared to earlier seasons. It increased from the upper zone to the middle of the lower zone where maximum concentration (25 mg/l) was encountered. This was the highest concentration of TSM among all the three seasons. In Zuari estuary however, the TSM values were the least among the three seasons (2.3 -12.5 mg/l).

3.2.2.2 Mean and standard deviation of absorption by TSM (a_s)

A) Pre-monsoon

The a_s spectra displayed a decreasing trend from 400 nm to 700 nm. In Mandovi estuary, the highest mean and standard deviation was observed in middle zone (Fig. 3.6(ii)a) and the least in the lower zone (Fig. 3.6(iii)a).

In Zuari, the mean was similar (~ 2 m^{-1} at 400 nm) in all three zones. However, standard deviation was the highest in the middle zone (Fig. 3.6(ii)b) and lowest in the upper zone (Fig. 3.6(i)b). The mean spectra were not very different between the two estuaries.

(i)

(ii)

(iii)
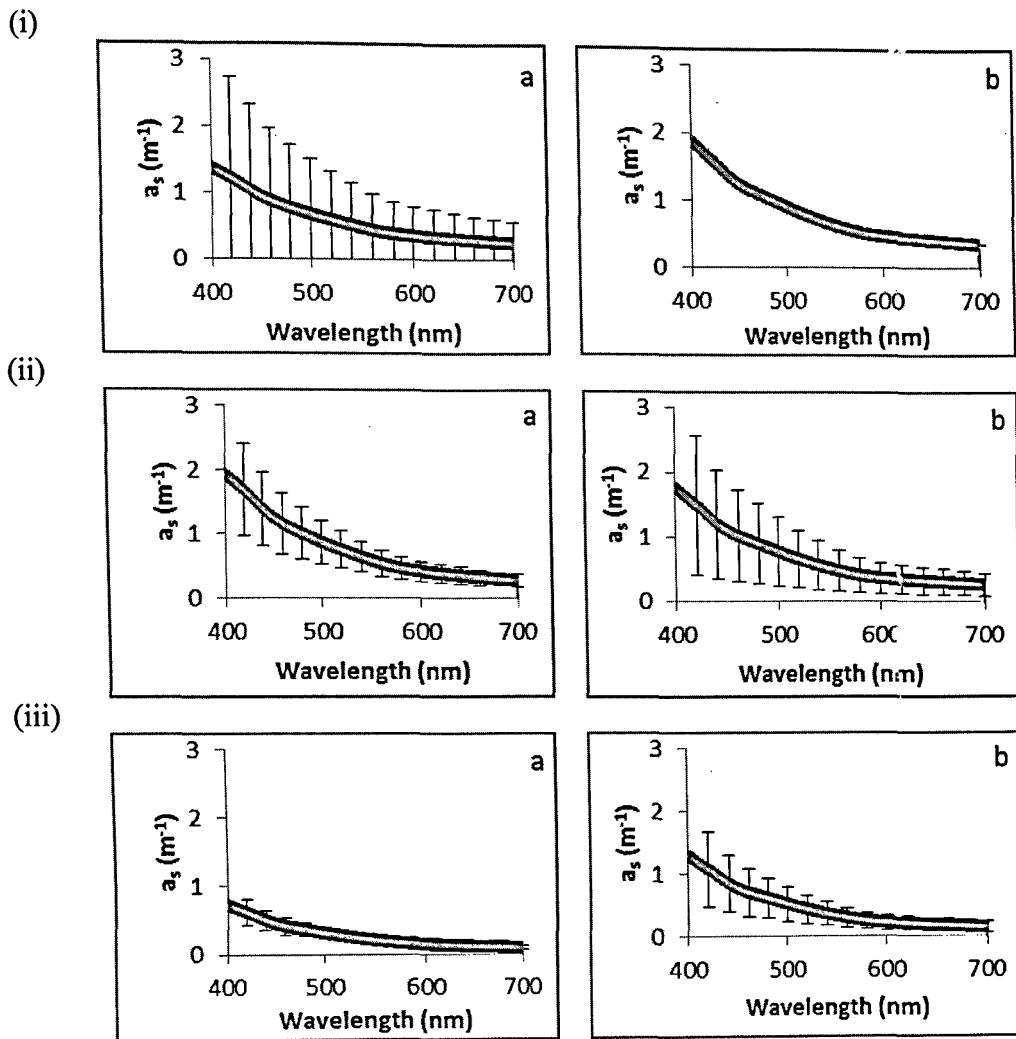
Fig. 3.6 Mean and standard deviation of spectral variation of absorption coefficient of TSM ($a_s(\lambda)$) in pre-monsoon at (i) upper (ii) middle and (iii) lower zones for (a) Mandovi and (b) Zuari estuaries

B) Monsoon

The middle zones of both the estuaries showed high absorption coefficient and standard deviation during monsoon season (Fig.3.7(ii)), almost two times the absorption in the other two zones.

The least absorption was observed in lower zones (Fig. 3.7(iii)a) of both the estuaries. The least standard deviation was observed in the upper zone of Mandovi estuary (Fig. 3.7 (i)a) and lower zone of Zuari estuary (Fig. 3.7 (iii)b).
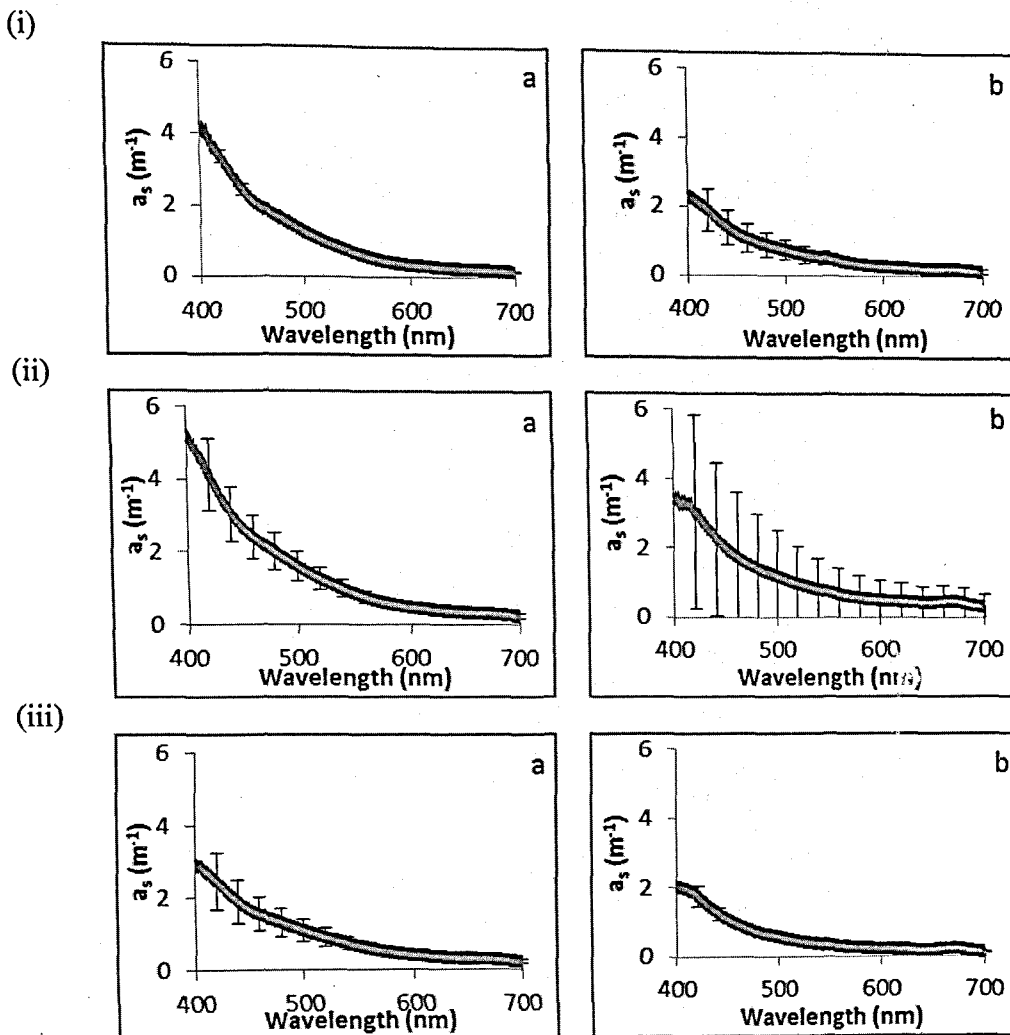
Fig. 3.7 Mean and standard deviation of spectral variation of absorption coefficient of TSM ($a_s(\lambda)$) in monsoon at (i) upper (ii) middle and (iii) lower zones of (a) Mandovi and (b) Zuari estuaries

C) Post-monsoon

During post-monsoon, the highest mean value for Mandovi estuary was observed in the middle zone (Fig. 3.8 (ii)a) and the lowest in lower zone (Fig. 3.8 (iii)b). In Zuari estuary, the highest mean absorption was observed in the upper zone

(Fig. 3.8 (i)b) and the lowest in the lower zone (Fig. 3.8 (iii)). The highest standard deviation was observed in the middle zone for both the estuaries.

(i)

(ii)

(iii)
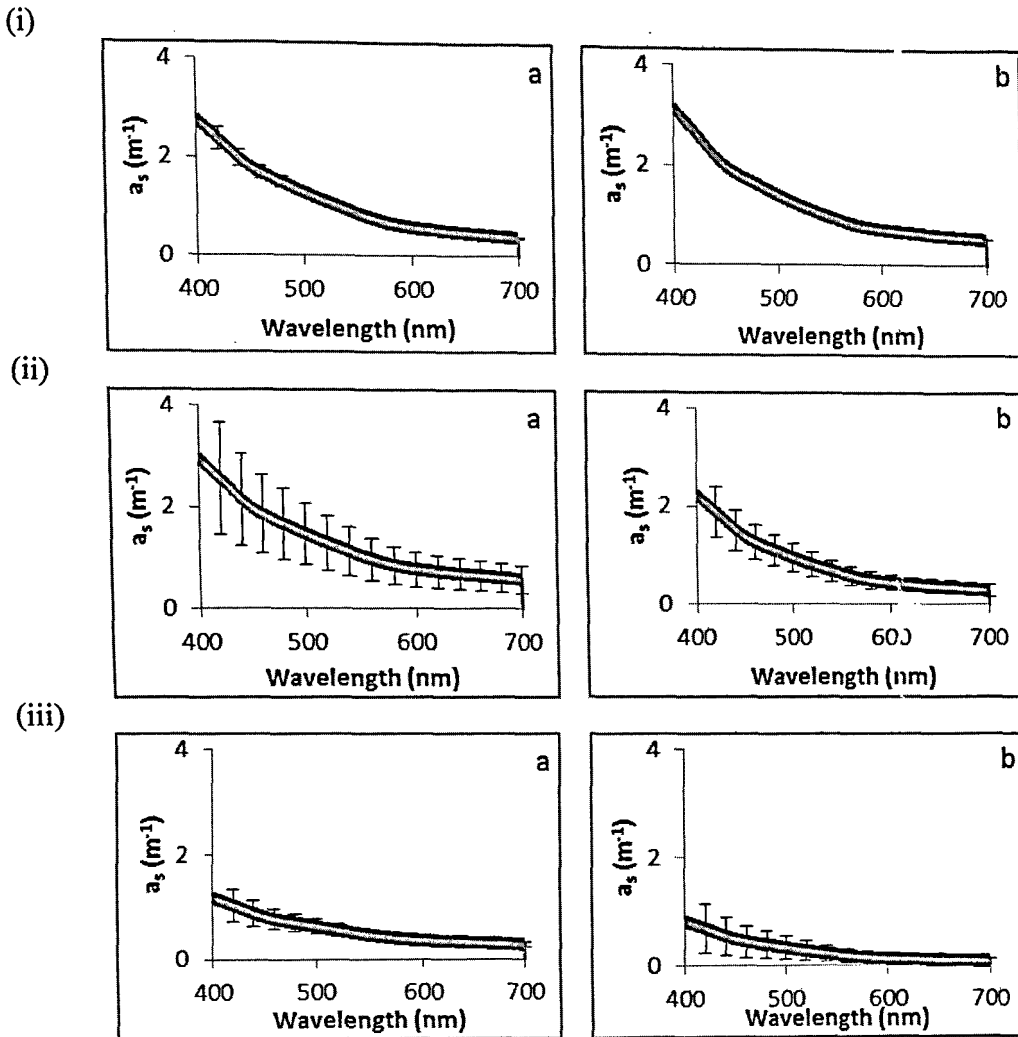
Fig. 3.8 7 Mean and standard deviation of spectral variation of absorption coefficient of TSM ($a_s(\lambda)$) in Post-monsoon at (i) upper (ii) middle and (iii) lower zones for (a) Mandovi and (b) Zuari estuaries

3.2.3 Chromophoric Dissolved Organic Matter (CDOM)

3.2.3.1 Temporal and spatial variability of Chromophoric Dissolved Organic Matter ($a_{CDOM}(440)$)

Fig. 3.9a displays that $a_{CDOM}(440)$ in Mandovi estuary, during pre-monsoon season decreased from upper zone to middle zone and further increased to lower

zone. Maximum value (0.93 m^{-1}) was observed in the lower zone. In the Zuari estuary, a$_{CDOM}$(440) varied irregularly with high concentrations (>1 m^{-1}) at stations Z05, Z08, Z11, Z15.

a)

b)
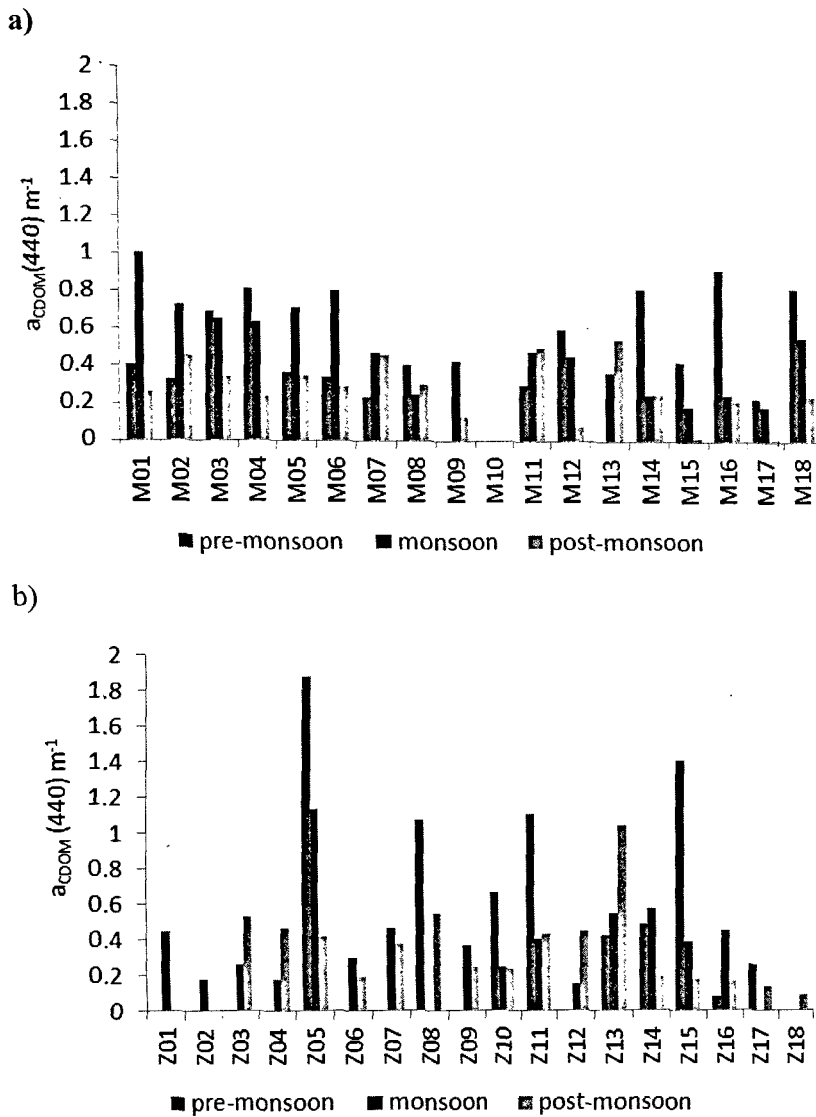
Fig. 3.9 Temporal and spatial variation of a$_{CDOM}$(440) in a) Mandovi estuary and b) Zuari estuary.

During monsoon season, maximum a$_{CDOM}$(440) (m^{-1}) was observed in the upper zone (station M01) of Mandovi estuary. Further, it was also observed that at all the stations of the upper zone, a$_{CDOM}$(440) was in the range 0.7 - 1 m^{-1}. The absorption at 440 nm decreased to middle zone (0.3 - 0.5 m^{-1}). In Zuari estuary however, the

$a_{CDOM}(440)$ values ranged from 0.18 to 0.59 m^{-1} except at station Z05 (1.2 m^{-1};Fig. 3.9b). The variation was in an irregular pattern between middle and lower zones (0.2 - 0.6m^{-1}).

During post-monsoon season, an asymmetrical variability of $a_{CDOM}(440)$ was depicted throughout the estuary. In Mandovi, the range of $a_{CDOM}(440)$ in the upper zone was 0.2 – 0.4 m^{-1} while in the middle and lower zones the range was similar (0.1-0.6 m^{-1}). The Zuari estuary depicted pattern and range similar to its monsoon variation and highest $a_{CDOM}(440)$ value was recorded at Z13 in lower zone (Fig. 3.9b).

3.2.3.2 Mean and standard deviation of absorption by CDOM (a_{CDOM})

A) Pre-monsoon.

The spectral variation of a_{CDOM} is such that the values decrease exponentially from 400 nm to 700 nm. In Mandovi estuary, the mean spectral values were almost similar for all the three zones, while in Zuari it was observed to be highest in the lower zone (Fig. 3.10(iii) b). The other two zones depicted values similar to each other. The standard deviation in the lower zone of the Zuari estuary was the highest (Fig. 3.10(iii) b). In the other zones, the standard deviation was very low. A similar feature was observed in Mandovi estuary.

(i)

(ii)

(iii)
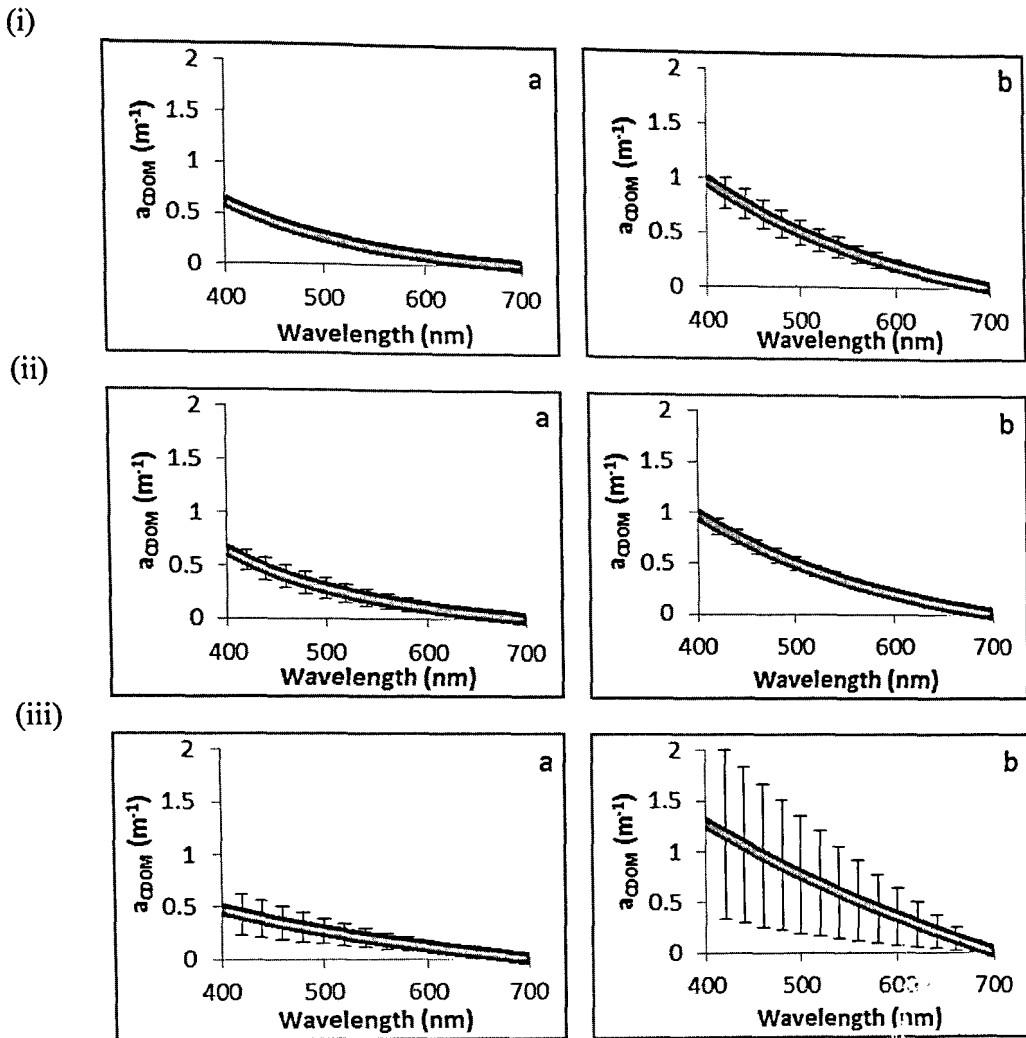
Fig. 3.10 7 Mean and standard deviation of spectral variation of absorption coefficient of chromophoric dissolved organic matter ($a_{CDOM}(\lambda)$) in pre-monsoon at (i) upper (ii) middle and (iii) lower zones for (a) Mandovi and (b) Zuari estuaries

B) Monsoon

In monsoon, the highest mean a_{CDOM} and standard deviation was observed in middle (Fig. 3.11(ii)a) and upper zone (Fig. 3.11(i)b) of Mandovi and Zuari estuary respectively. The upper zone of Mandovi estuary and the lower zone of the Zuari estuary depicted lowest means and standard deviation for the respective estuaries.

39

(i)

(ii)

(iii)
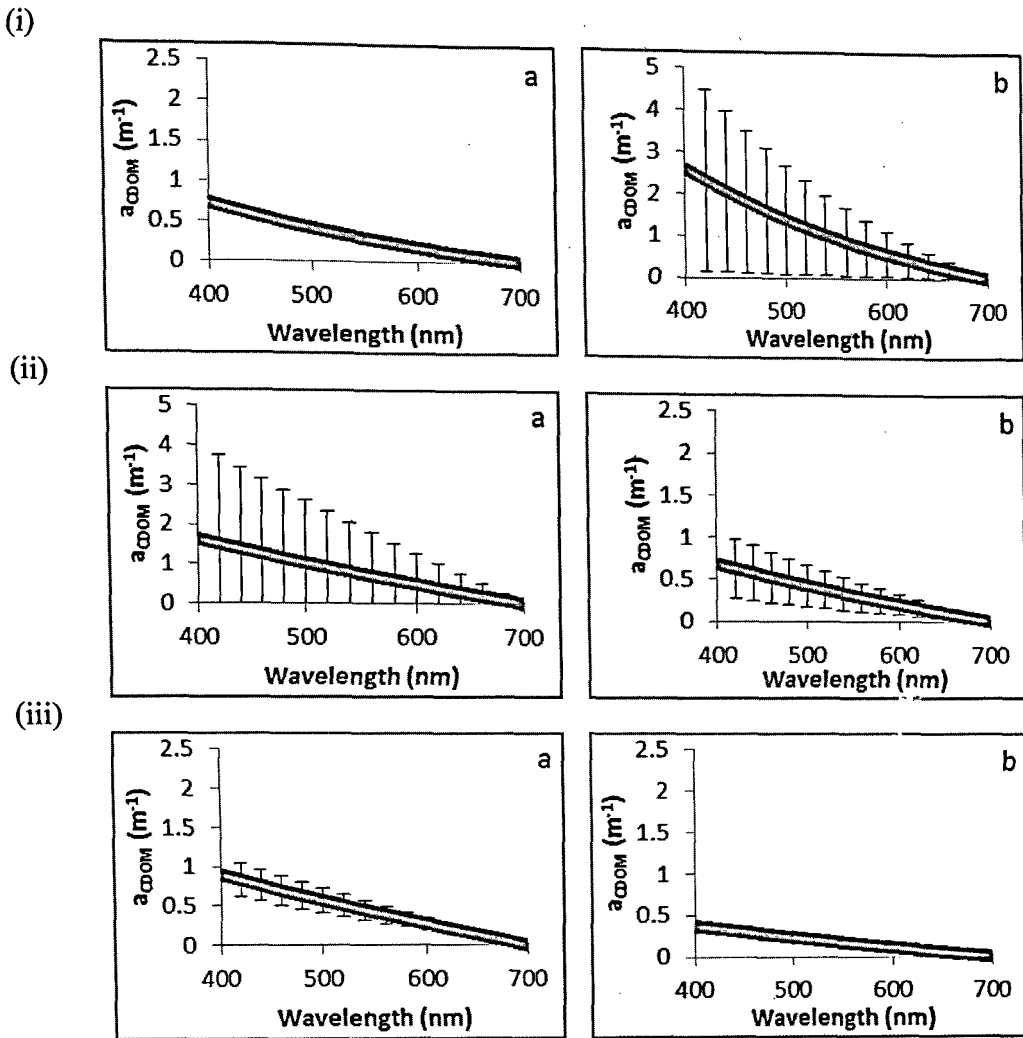
Fig. 3.11 7 Mean and standard deviation of spectral variation of absorption coefficient of chromophoric dissolved organic matter ($a_{CDOM}(\lambda)$) in monsoon at (i) upper (ii) middle and (iii) lower zones for (a) Mandovi and (b) Zuari estuaries

C) Post-monsoon

The post-monsoon depicted similar means in all three zones of both the estuaries. In Mandovi estuary, the standard deviation was the highest in the middle zone (Fig. 3.12(ii)a) while in the case of Zuari it was the highest in the lower zone (Fig. 3.12(iii)b).

(i)

(ii)

(iii)
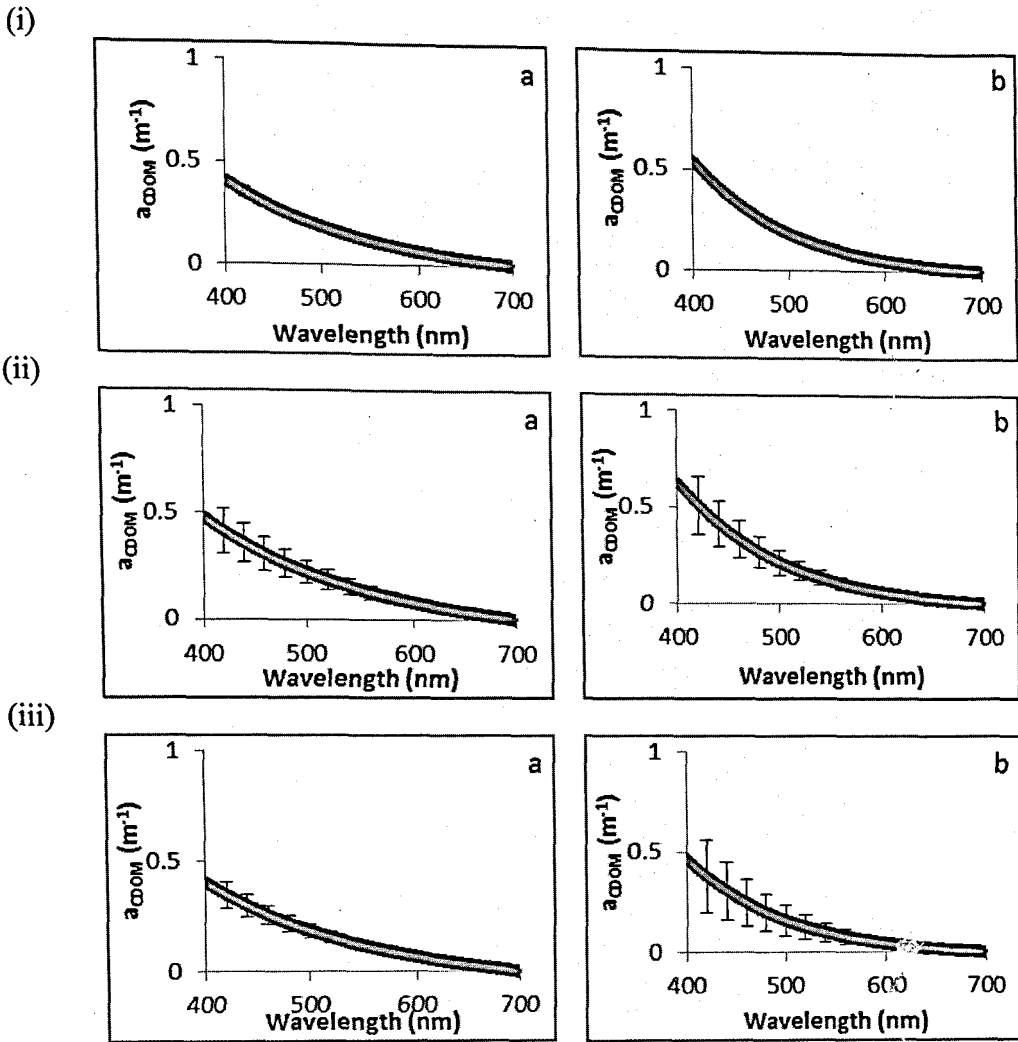
Fig. 3.12 7 Mean and standard deviation of spectral variation of absorption coefficient of chromophoric dissolved organic matter ($a_{CDOM}(\lambda)$) in post-monsoon at (i) upper (ii) middle and (iii) lower zones for (a) Mandovi and (b) Zuari estuaries

3.3 Radiometric measurements:

The radiometer was operated from the side of the trawler facing the sun to avoid the shadow cast by the trawler itself. In addition, care was exercised to deploy it as far as possible from the trawler to avoid the shadow of the trawler bottom. It was operated either up to euphotic depth (the depth at which 1% of surface PAR is

41

encountered) or the total depth (minus 1-2 m to avoid abrasion to the instrument), whichever was encountered first.

The recorded data was processed using the software Prosoft 7.7.10 supplied with the instrument. Various parameters derived from the radiometric measurements of L_u, E_d and E_s are given below

The PAR was computed using the following equation (Kirk, 1994)

$$PAR = [h\ c]^{-1} \int_{400}^{700} \lambda\ E_d(\lambda,\ z)\ d\lambda\ [quanta\text{-}m^{-2}\text{-}sec^{-1}] \tag{3.11}$$

Where h is the Plank's constant and c is velocity of light in vacuum. Diffuse attenuation coefficient of E_d (λ), (k_d (λ)), over the euphotic depth was then calculated as

$$k_d\ (\lambda) = -\ [E_d(\lambda)]^{-1}\ d\ [E_d(\lambda)]\ /dz\ [m^{-1}] \tag{3.12}$$

The remote sensing reflectance (R_{rs} (λ, 0^+)) was calculated as per Carder (1993)

$$R_{rs}\ (\lambda,\ 0^+) = L_u\ (\lambda,\ 0^+)\ /\ E_d\ (\lambda,\ 0^+)\ [sr^{-1}] \tag{3.13}$$

L_u (λ, 0^+) is L_w (λ), the water leaving radiance, derived from $L_u(\lambda, 0^-)$ (L_u just below the surface) measured using radiometer as per Magnuson $et\ al.$, (2004),

$$L_w(\lambda) = 0.54\ L_u(\lambda,\ 0^-) \tag{3.14}$$

and E_d (λ, 0^+) is the surface downwelling irradiance derived from E_d (λ, 0^-) (E_d just below the surface) measured using radiometer measurements as per (Magnuson $et\ al.$, 2004),

$$E_d\ (\lambda,\ 0^+) = E_d\ (\lambda,\ 0^-)/0.98 \tag{3.15}$$

3.4 Remote sensing reflectance variability

3.4.1 Pre-monsoon season
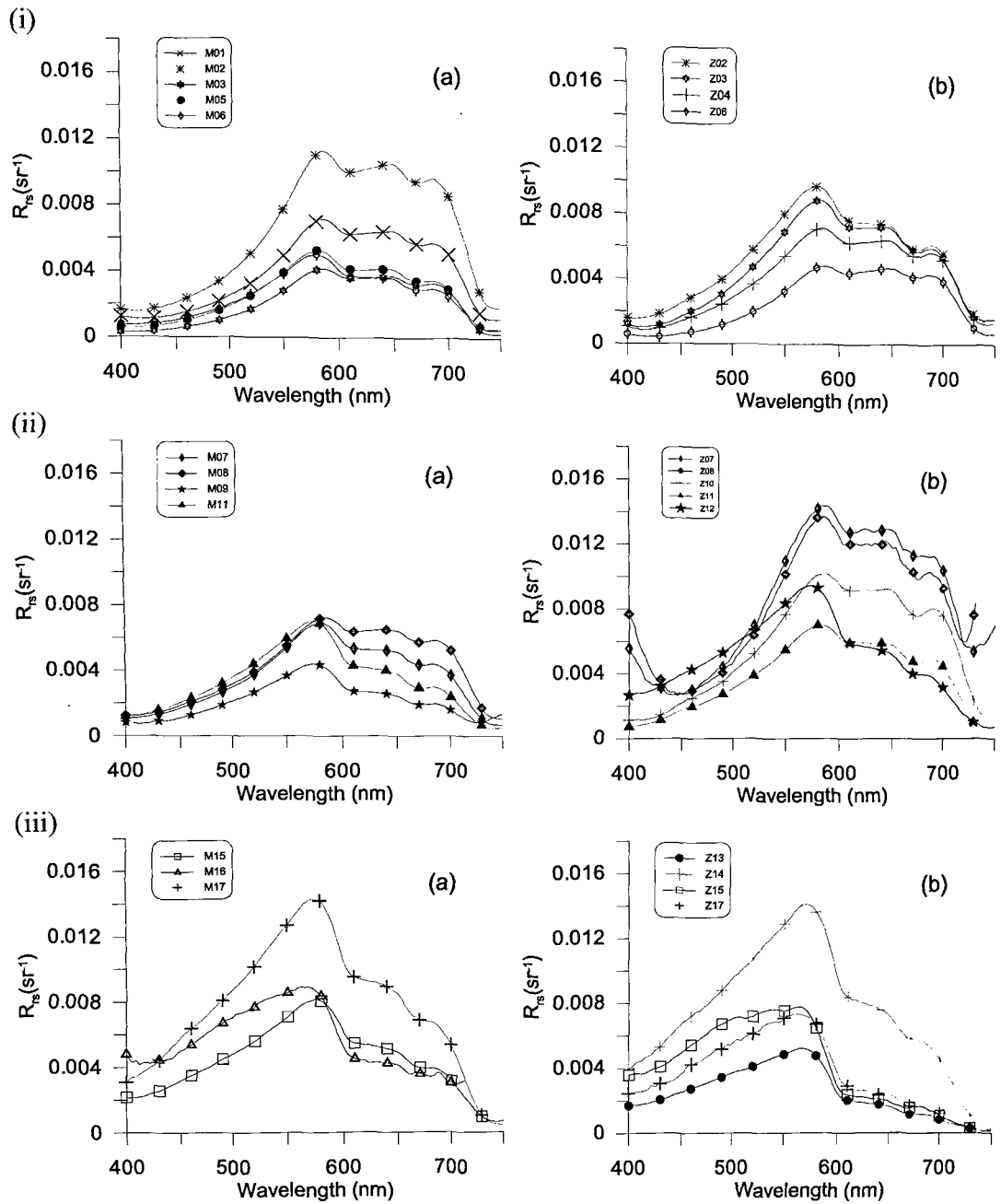
Fig. 3.13 Spectral variation of R_{rs} during pre-monsoon at (i) upper (ii) middle and (iii) lower zones for (a) Mandovi and (b) Zuari estuaries.

The R_{rs} spectra generated in pre-monsoon are shown in the Fig. 3.13. As seen from the figure, the spectral shape of the R_{rs} varies from the upper zone to the lower zone. The R_{rs} at all the stations, irrespective of the seasons and estuary displayed a

common feature between 400 nm and 580 nm. In this wavelength range the R_{rs} was low. All the three OAC were observed to absorb in this region of the spectra (Figs. 3.2 to 3.12) and hence resulted in low reflectance.

In the upper zone, the reflectance spectra at all the stations exhibited similar shape. The maximum R_{rs} was encountered at 586 nm. The R_{rs} remained high up to 688 nm and then decreased up to 750 nm. Overall, the region of high R_{rs} was between 580 to 690 nm for the upper zone. The Mandovi estuary depicted flat spectrum between 580 to 690 nm at all the stations. The R_{rs} values at longer wavelengths were high and co-varied with the TSM concentration (except station M01). However, in Zuari the spectrum showed a peak at 580 nm for stations Z02, Z03 and Z04. Z06 depicted a flat spectrum. The R_{rs} values at longer wavelengths were high and co-varied with the TSM concentration (except station M01). The middle zone exhibited spectral characteristics marked with high R_{rs} between 586 nm to 688 nm in both Mandovi and Zuari estuaries. R_{rs} values were similar between 400 nm and 586 nm at all stations except M09. The R_{rs} was observed to be higher in Zuari compared to Mandovi (Fig. 3.13 (ii)). In the lower zone, the R_{rs} peaked at about 570 nm and then decreased gradually up to 750 nm in both the estuaries. High values at longer wavelengths observed for spectra of the upper and the middle zones were not seen here. Both Chlorophyll-a and TSM were low in concentration in this zone (Figs. 3.1 and 3.5), while CDOM concentration increased.

The difference in the spectral characteristic could be attributed to the difference in the OAC present in the water column between the two zones (more terrigeneous towards the upper zone (upper end) and marine towards the lower zone (lower end) of the estuary.

3.4.2 Monsoon season
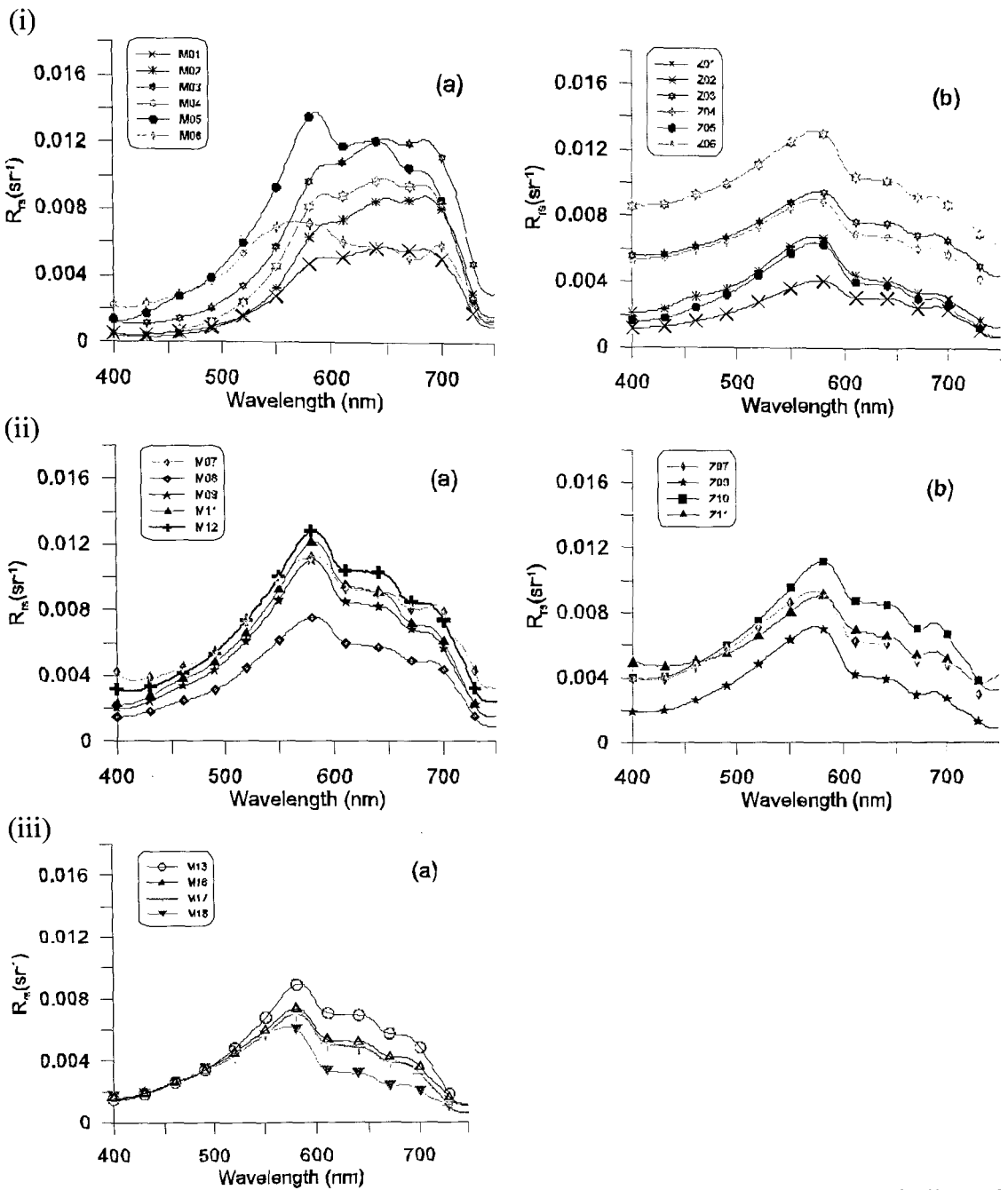
Fig. 3.14 Spectral variation of R_{rs} during monsoon season at (i) upper (ii) middle and (iii) lower zones for (a) Mandovi and (b) Zuari estuaries

Due to the rough weather conditions in the monsoon season, sampling at the lower zone of the Zuari estuary was not carried out.

Similar to the observations during pre-monsoon, the R_{rs} values were high between 570 nm and 700 nm and then decreased up to 750 nm in the upper zone of

the Mandovi estuary (Fig. 3.14(i) a). However, the stations M01 - M04 depicted a shift of R_{rs} peak from 580 nm to 680 nm. The R_{rs} spectrum at station M05 showed a peak at 580 nm while the R_{rs} spectrum at M06 showed a peak at 555 nm. The above difference could be attributed to the difference in the TSM concentration at these stations (Fig. 3.5a). The TSM concentration recorded at stations M01 - M04 was 2 - 3 times the concentration at stations M05 and M06. Such high TSM concentration may have resulted in the increase in R_{rs} in the red region. The observed surface salinity was close to zero in this zone (Fig. 2.2 b) and highlighted the fact that the high TSM concentration was due to the excessive land run off in the monsoon. The relatively high CDOM and Chlorophyll-a concentration resulted in R_{rs} values less than $0.002sr^{-1}$ between 400 and 470 nm. Although, the range of TSM concentration in the upper zone of the Zuari estuary was observed to be similar to that in Mandovi, it displayed a completely different picture. The Chlorophyll-a concentration, however, was 2 to 4 times than that in Mandovi estuary for the respective zone.

In the middle zone of the Mandovi estuary, TSM concentration was almost 3 times lesser than that observed in the upper zone which led to R_{rs} in the red region. The R_{rs} peaked at 575 nm and then decreased gradually towards the longer wavelength. This zone depicted salinity of less than 1PSU (Fig. 2.1a) and therefore, it is under considerable influence of the fresh water flow. The Zuari estuary exhibited spectral variation similar to that of Mandovi estuary and the values were also in a similar range. The spectral shape of R_{rs} in the lower zone was similar to that in the middle zone for both the estuaries. This zone depicted high R_{rs} in the longer wavelength as compared to the lower zone in the pre-monsoon.

3.4.3 Post-monsoon season.

(i)

(ii)

(iii)
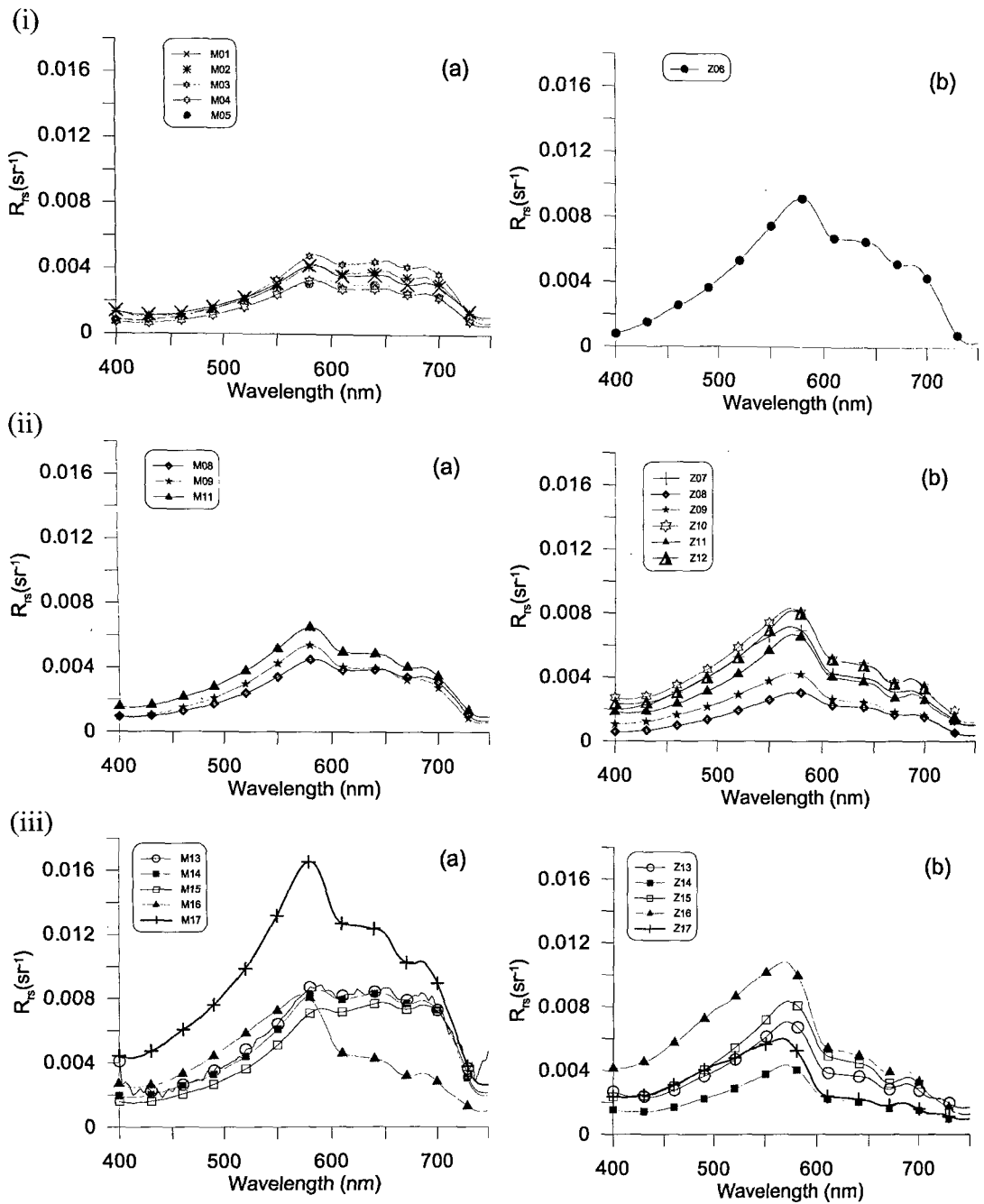
Fig. 3.15 Spectral variation of R_{rs} during post-monsoon at (i) upper (ii) middle and (iii) lower zones for (a) Mandovi and (b) Zuari

During the post-monsoon season, the R_{rs} values were very low in the upper zone of the Mandovi estuary and displayed flat spectrum between 585 nm and 670 nm

47

(Fig.3.15(i)a). OAC concentration within the zone did not vary substantially (Fig. 3.5). This was reflected in the R_{rs} spectra which did not show large variation in the values within this zone. In Zuari estuary however, the R_{rs} depicted peak at around 575 nm and the values decreased towards the longer wavelength (Fig.3.15(i)b).

The spectral characteristics recorded in the lower zones of both the estuaries during the post-monsoon were similar to those recorded in the lower zone during the other two seasons except three stations in Mandovi estuary (M13, M14 and M15) (Fig. 3.15(iii)). These three stations depicted high values between 586 nm and 675 nm and remained flat in this spectral region. High TSM concentrations were encountered at these stations.

The spectral characteristics of R_{rs} were highly variable both spatially and seasonally as observed above. In addition, it was also observed that the spectral characteristics were not similar between the two estuaries in some cases (pre-monsoon upper and middle zone, monsoon upper zone and post-monsoon upper zone). However, there were a few similar characteristics observed in all the spectra. The R_{rs} spectra consistently displayed low reflectance in the spectral interval between 400 nm and 550 nm. All the three OAC (Figs. 3.1 to 3.12) absorb mainly in the shorter wavelength region (400-500 nm). A small dip was also observed consistently at around 667 nm in the R_{rs} spectra. This could be attributed to the secondary chlorophyll absorption peak (Figs. 3.2 to 3.4). These observations are consistent with the studies carried out in other estuarine waters (Froidefond *et al.*, 2002; Szekielda *et al.*, 2003).

The influence of monsoon on the optical signature (R_{rs}) is clearly demonstrated especially in the upper zone of the Mandovi estuary where the peak was

observed at 690 nm. This R_{rs} peak varied between monsoon and non-monsoon seasons. The peak in the R_{rs} at about 690 nm is usually attributed to the sun-induced natural fluorescence of the photosynthetic pigments (Hoge and Swift, 1987). However, in Mandovi, low Chlorophyll-a concentration suggests that the chlorophyll fluorescence is low. The catchment area is mountainous and composed of Western Dharwar Craton with gneissic and schistose rocks and ferruginized lateritic cappings (Naqvi, 2005). High abundance of kaolinite (product of silicate alteration in lateritic soils) is found in the suspended sediments at the upper region of Mandovi estuary (Bukhari and Nayak, 1996; Kessarkar et al., 2010). This clay mineral is found in close association with the laterite and its concentration is reported to be very high during the monsoon season (Bukhari and Nayak, 1996). Thus the sediment load in the water column is responsible for a peak at 690 nm at upper zone in monsoon in Mandovi estuary (Fig. 3.14 (i) a).

In Zuari estuary, however, this feature was not observed though the concentration of TSM was greater than in Mandovi. The concentrations of OAC alone do not affect the spectral signature of a water column. In case of TSM, the particle size and shape also play an important role (Ferrari et al., 2003). Since the particle size and shape was not a part of the present study, this was not analysed. Chlorophyll-a concentration was also high in this season compared to Mandovi estuary, which might have led to absorption and hence low reflectance. In addition, during monsoon season, the environmental condition (cloud cover and high sediment load) is not conducive for an intense fluorescence emission which is around 680 nm. Since the geology of the catchment areas of both the estuaries is same (Naqvi, 2005), the sediment load is expected to be similar and impart similar spectral properties. However, the upper zone of the Mandovi was completely under the influence of the fresh water while in Zuari

there was saline intrusion up to the upper zone, though at a very small scale as compared to the other seasons (Fig. 2.3 (ii)). The increase in salinity can lead to flocculation of clay–like particles (Roux et al., 1998). This might be one of the reasons for the removal of the suspended particles from the upper zone of Zuari responsible for the reflectance in the red region of the spectrum and hence low reflectance.

Another feature observed was the flat spectrum at three stations in the lower zone of Mandovi estuary during post-monsoon season. In the post-monsoon season the estuary was characterised as partially mixed (Fig. 2.2c). In this estuary, as the monsoon ceases, salinity incursion due to tide dominates which results in the weakening of haline front at the lower zone and mixing of suspended particles flocculated at this front. Since the stations M13, M14 and M15 were from the position where haline front was formed (Fig.2.2 (iii)), the instability of front due to the tide might have mixed the water column and augmented the sediment concentration due to resuspension. However, the other two stations of lower zone were from the seaward side of the estuary, where a peak was observed at 586 nm instead of a flat spectrum. This is also evident from the low TSM concentration (Fig. 3.5a).

All the spectra in the lower zone exhibited typical coastal water characteristics with a peak at 586 nm. Studies have shown change in reflectance characteristics with change in concentration and constituents present in the water column (Liew et al., 1999; Froidefond et al., 2002). In accordance with the above, the material in suspension in the upper and lower zones of the two estuaries was different from that of the upper zone. The suspended matter in the lower zone is of marine origin (Bukhari and Nayak, 1996) and composed of sand and clay (Bhaskar and Bhosale, 2008). These particles do not scatter light in the longer wavelength region like the

50

suspended material found in the upper zone, hence low reflectance in the red region of the spectrum.

Overall, it was observed that the seasonal variation in the R_{rs} is more evident from its spectral characteristics instead of its magnitude which does not show any effect on the R_{rs}. Seasonal changes observed with respect to spectral signature rather than the magnitude have also been reported by Darecki *et al.* (1995), Kowalczuk *et al.* (1999) and Olszewski *et al.* (1999). It was also observed that the R_{rs} spectra vary with the OAC composition of the water column. A combined study of R_{rs} and OAC species can help identify the exact OAC effects with respect to their species. The two estuaries displayed highly diverse R_{rs} characteristics. This implies that the optical environment of the two estuaries is highly complex and different from each other even though they lie in the same geographical regime.

3.5 Absorption Budget of Mandovi and Zuari estuaries

It was observed that the absorption coefficients of the three OAC varied between the three seasons and also between zones and estuaries. Such a large degree of variation between the two estuaries, which are geographically so close, shows that the estuaries are very dynamic in nature. Hence, the relative effect of the three OAC on total absorption of the water column was analysed. This was carried out by analysing the normalised absorption using ternary plots.

The normalised absorption for each OAC was computed as follows

$$a_{nor(x)}(\lambda) = a_x(\lambda) / a(\lambda) \tag{3.16}$$

Where,

$a_{nor(x)}(\lambda)$ is the normalised absorption for x, $a_x(\lambda)$ is the absorption coefficient for x, $a(\lambda)$ is the total absorption and x stands for c (Chl-a), s (TSM) and CDOM

The ternary plots were plotted for the selected wavelengths corresponding to Ocean colour monitor (OCM onboard Indian Remote Sensing Satellite – P4 – IRS-P4) bands. The seasonal characterisation of the normalised absorption is presented below.

3.5.1 Normalised absorption -pre-monsoon

The ternary plots for pre-monsoon season (Fig. 3.16) depict that the absorption in the season for both the estuaries was dominated by TSM and CDOM at all the wavelengths in consideration. The upper zone showed absorption mainly by TSM (greater than 50%) in Zuari estuary (Fig. 3.16(i)b). In Mandovi, the upper zone showed absorption by TSM and CDOM (Fig. 3.16(i)a). The absorption was observed to shift from TSM corner at upper zone to CDOM corner at the lower zone, more prominently in Zuari estuary.

Chlorophyll-a showed low absorption (less than 50%) at all the zones in both the estuaries. However, at wavelengths other than 670 nm, Chlorophyll-a displayed less than 30% absorption. In the middle zone of Mandovi, the TSM absorption was more than 50% (Fig. 3.16(ii)a), while in Zuari estuary the TSM absorption varied between 30% and 80% (Fig. 3.16(ii)b). Even at the lower zone, Mandovi displayed greater TSM absorption than Zuari estuary (Fig. 3.16(iii)). In Zuari, the CDOM absorption was greater than the Mandovi estuary.
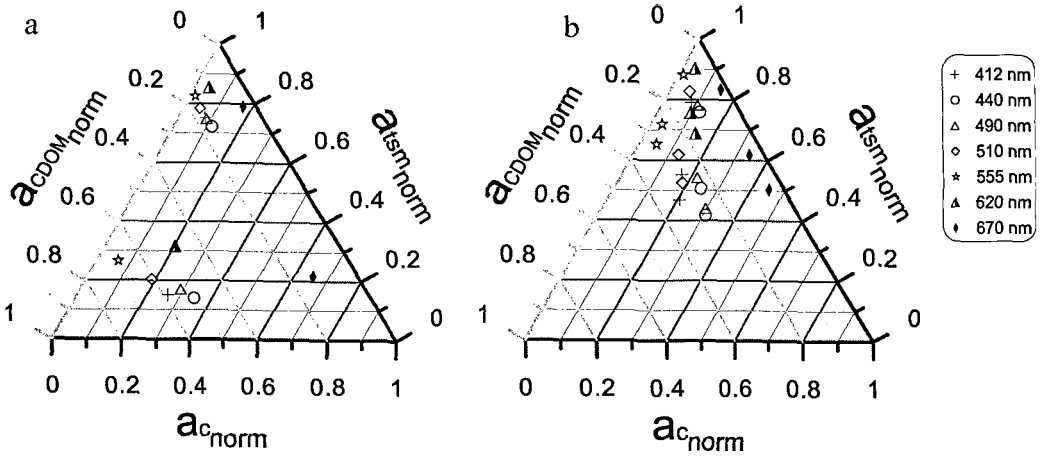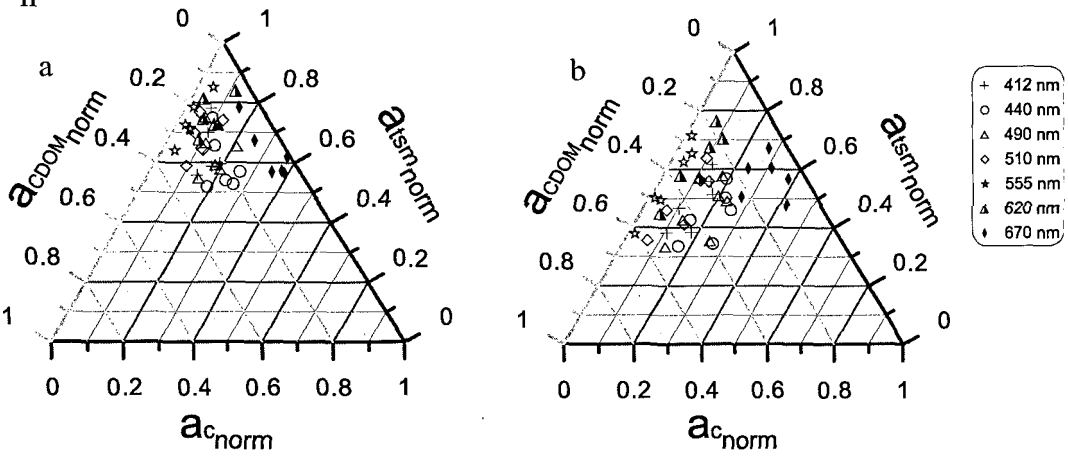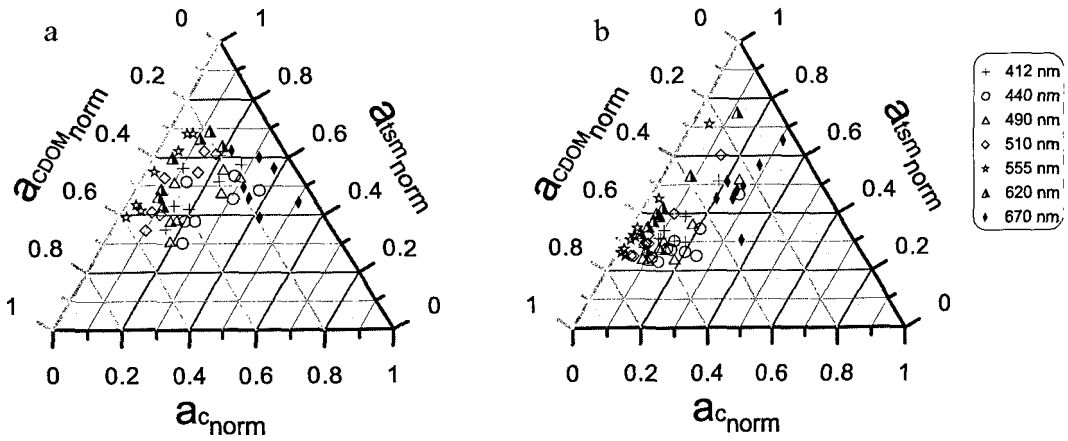
Fig. 3.16 Ternary plots for normalised absorption by the three OAC in Pre-monsoon at (i) upper (ii) middle zone and (iii) lower zone for (a) Mandovi and (b) Zuari estuaries.

53

3.5.2 Normalised absorption - monsoon
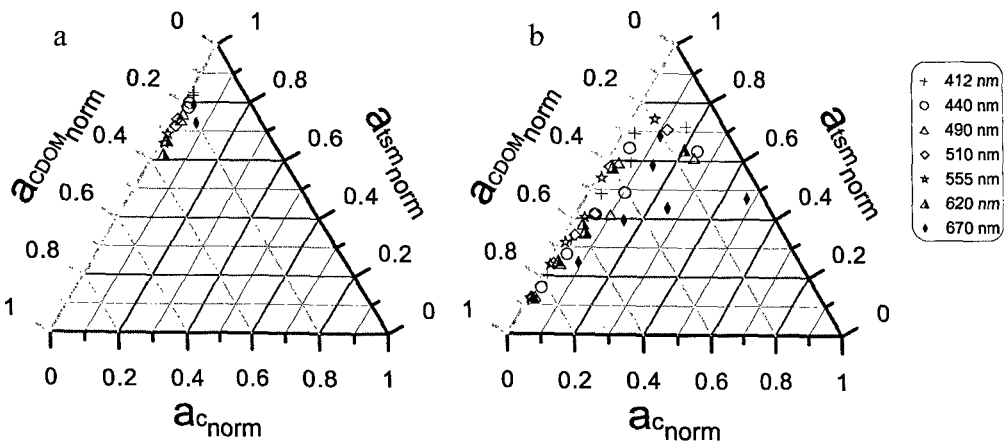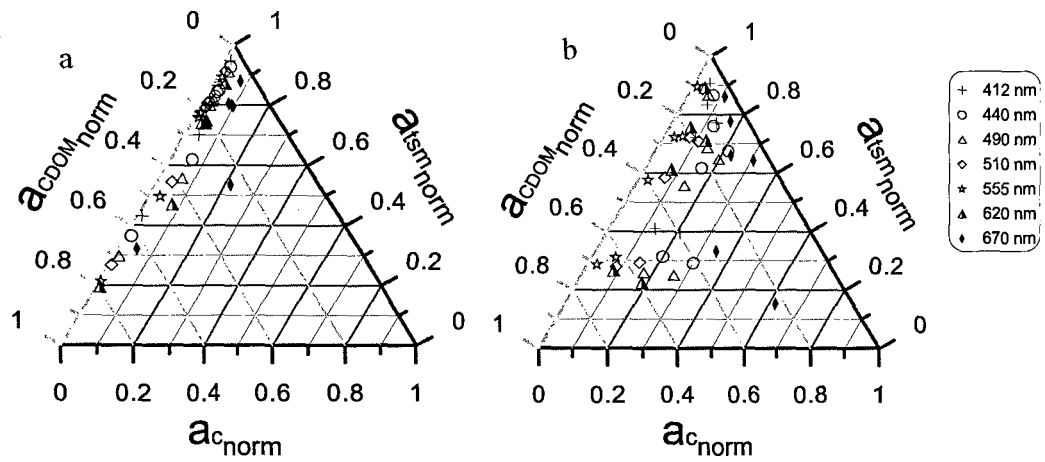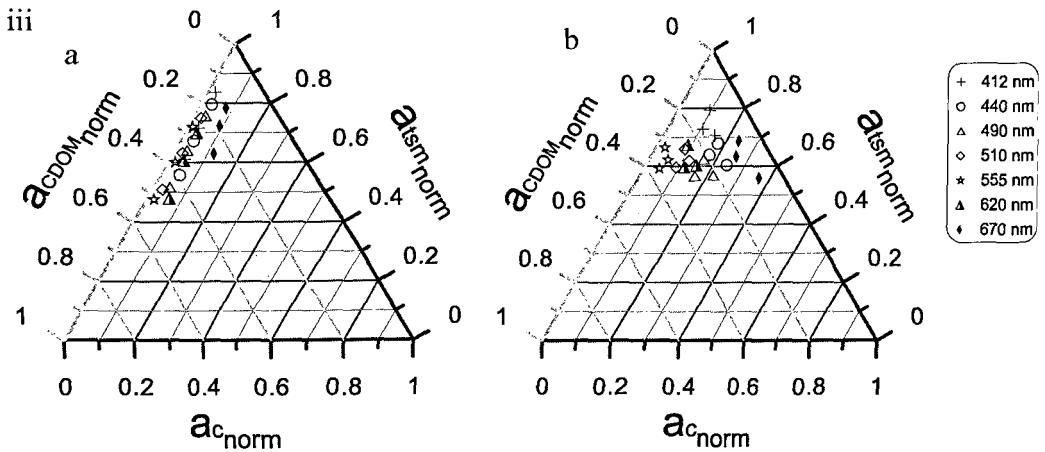
Fig. 3.17 Ternary plots for normalised absorption by the three OAC in Monsoon at (i) upper (ii) middle and (iii) lower zones for (a) Mandovi and (b) Zuari

Monsoon depicted a very interesting difference in the Mandovi and Zuari absorption characteristics. The Mandovi estuary consistently exhibited negligible Chlorophyll-a absorption in all the three zones. In the upper zone, the TSM absorption was greater than 60% (Fig. 3.17(i)a). In the middle zone, the effect of CDOM was observed with absorption by CDOM ranging from 10% to 80% (Fig. 3.17(ii)a). This reflects the dynamics of this zone with respect to CDOM. In the lower zone too, the TSM exhibited dominance in the absorption. The Zuari estuary depicted Chlorophyll-a absorption up to 30% in all three zones. The middle and lower zones displayed dominance of TSM absorption (Fig. 3.16(ii and iii)b) while upper zone showed considerable CDOM absorption (Fig. 3.16(i)b).

3.5.3 Normalised absorption – post-monsoon

During the post-monsoon season, the upper and middle zones of the two estuaries displayed dominance of TSM absorption. The lower zone also depicted high TSM absorption but the effect of the CDOM absorption was also visible. This was more prominent in the Zuari estuary where CDOM absorption reached up to 80%.

The ternary plots depicted the differential behaviour of the OAC absorption in the two estuaries. The Mandovi estuary was dominated by TSM absorption compared to Zuari estuary in all the three seasons. In Zuari however, the CDOM absorption was observed to be more prominent than in the Mandovi. In addition, the effect of CDOM was more profound towards the lower zone of the estuary. The upper zone depicted more absorption by TSM. This is consistent with the fact that the upper zone of the estuaries are dominated by the terrigeneous sediment which absorbs more light compared to the sediment in the lower zone. The lower zone depicts suspended

sediment of marine origin (sand and clay) (Bhaskar and Bhosale, 2008). Chlorophyll-a absorption was consistently less in all the three seasons in both the estuaries.
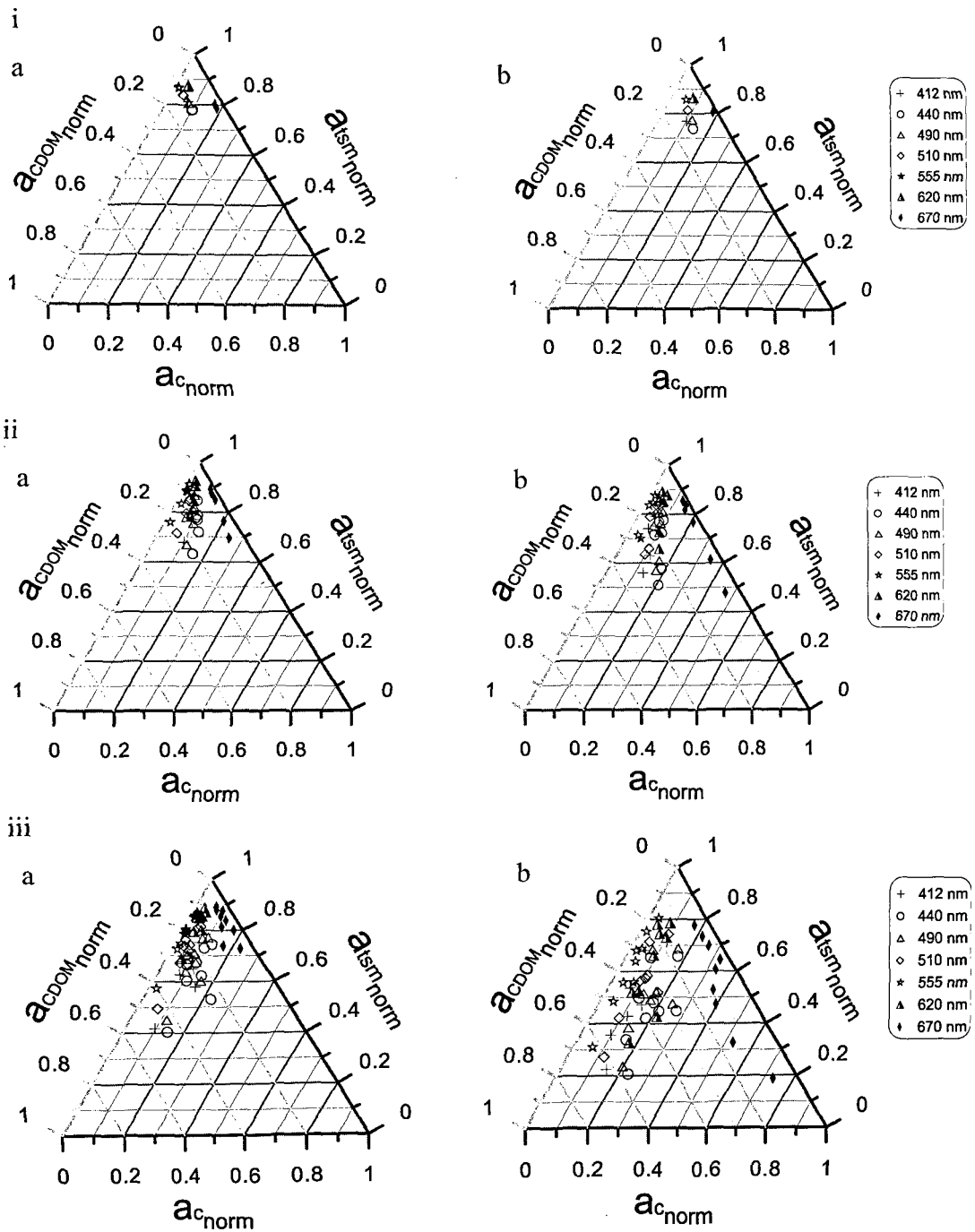
Fig. 3.18 Ternary plots for normalised absorption by the three OAC in Post-monsoon at (i) upper (ii) middle and (iii) lower zones for (a) Mandovi and (b) Zuari estuaries.

From the spectral and the ternary analysis of the absorption coefficient for both the estuaries it was clear that CDOM had a prominent effect on the absorption at shorter wavelengths, more so in the lower zones. Hence, the applicability of the ratio used previously to derive CDOM using OCM data in this region (Menon et al., 2006) was checked for the present set of data.
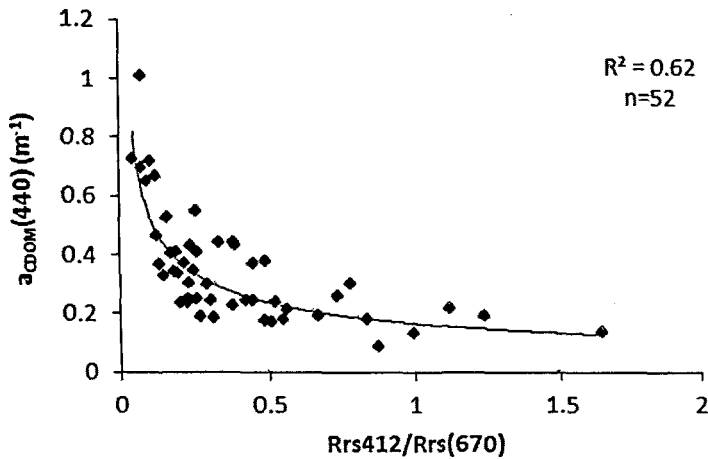
Fig. 3.19 Regression between $a_{CDOM}(440)$ and ratio $R_{rs}(412)/ R_{rs}(670)$

The ratio $R_{rs}(412)/ R_{rs}(670)$ was regressed with $a_{CDOM}(440)$ (Fig. 3.19). The regression revealed a good coefficient ($R^2=0.62$). Hence, the algorithm developed by Menon et al. (2006) was used to map CDOM from OCM data for the year 2005 and study the hydrodynamics of the estuarine system.

3.6 Derivative analysis

Derivative analysis is an effective tool for separating the contribution of various components of a composite spectrum of water (Chen et al., 1992, Goodin et al., 1993). It is also useful in separating the secondary absorption peak in regions of overlapping absorption (Aguirre-Gomez et al., 2001). A derivative plot indicates

more precisely the centre of absorption peaks with respect to the dependent variable under consideration. The inflection points in the first derivative can be resolved in the second derivative spectrum. However, all the peaks cannot be resolved. Hence, higher order derivatives can also be calculated to resolve the minute variations.

The R_{rs} of the water column depends on the water constituents in addition to the water molecules and hence a function of IOP.

Thus,

$$R_{rs}(\lambda) = F(a_w(\lambda), a_s(\lambda), a_c(\lambda), a_{CDOM}(\lambda))$$

Hence, derivative analysis (partial differentiation (∂R_{rs})) was carried out for R_{rs} with respect to the absorption coefficient by the three OAC derived for every 1 nm to understand the effect on the R_{rs} signal and to delineate the wavelength at which each OAC affects the R_{rs}.

The second and fourth order derivatives were analysed for the same. The derivative analysis did not reveal any absorption band for Chlorophyll-a. This may be attributed to the low absorption by Chlorophyll-a (3.16 to 3.18). Since, Chlorophyll-a absorption was observed to be very low, the partial derivative of R_{rs} with respect to Chlorophyll-a absorption could not reveal any effect on the R_{rs}. In other words, the effect of Chlorophyll-a was masked by the absorption of other two OAC.

The Mandovi – Zuari estuaries were observed to be dominated by absorption by both TSM and CDOM (Figs. 3.16 to 3.18). Thus, R_{rs} is bound to be affected to a greater extent by these two OAC. The second order derivative of the R_{rs} with respect to TSM absorption revealed absorption at 555 nm. The TSM absorbs more at the shorter wavelength (Fig.3.6), but the derivative analysis helps to delineate the wavelength affecting the parameter under consideration (Aguirre-Gomez *et al.*, 2001), in this case the R_{rs}. Since, the TSM reflects more in the longer wavelength regions

including NIR (Doxaran *et al.*, 2002a; Menon *et al.*, 2011), longer wavelengths were used in ratio with 555 nm to check the feasibility in deriving TS̄ː. The ratio of $R_{rs}(740)/ R_{rs}(555)$ was observed to correlate well with the TSM concentration (Fig. 3.20).
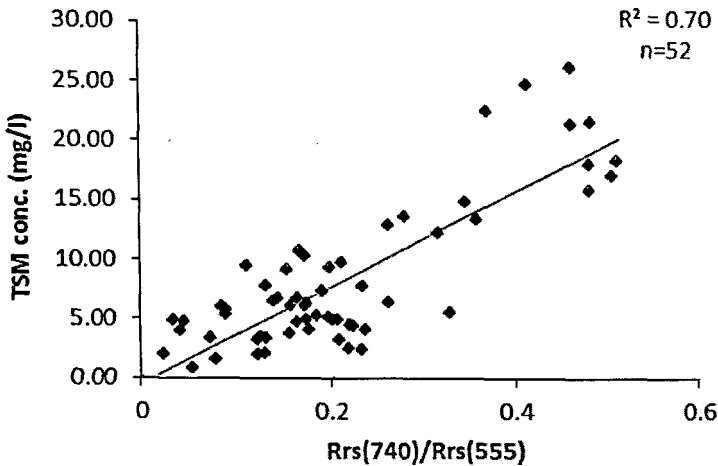
Fig. 3.20 Regression between $a_{CDOM}(440)$ and ratio $R_{rs}(740)/ R_{rs}(555)$

A good regression (R^2=0.70) was observed for the above relation (Fig. 3.20). The 555 nm band is available on both the sensors (OCM 1 and OCM 2) and 740 nm is available on OCM 2. However, the OCM 2 data shows high radiance. Hence, the relation has not been applied to the satellite data to derive TSM concentration.

3.7 Satellite retrieval of CDOM from OCM-I data.

The algorithm developed by Menon *et al.* (2006) was used to derive CDOM from OCM data for the year 2005.

$$a_{CDOM}(440) = 1.6032 \ (L_w(412)/ L_w(670))^{-1.906} \qquad (3.17)$$

The derived CDOM values were validated with the in-situ values (Fig. 3.21). The data sets were logarithmically transformed (base 10) to calculate RMS and bias. The RMS log error was 14.25% and log difference bias was 3.89%.
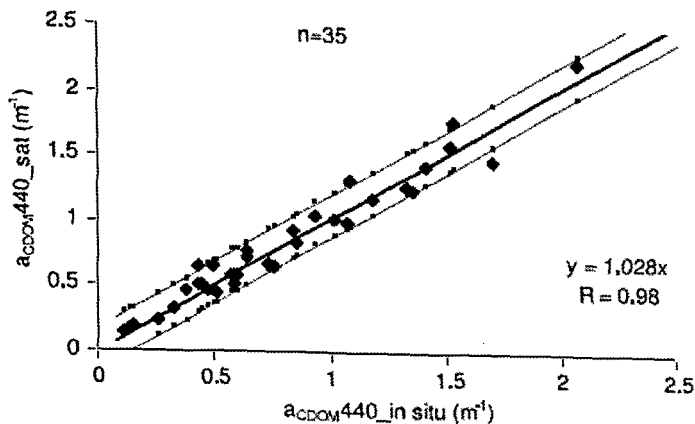
Fig. 3.21 Correlation between in-situ and satellite derived $a_{CDOM}(440)$ (the dotted line in the figure shows 95% confidence level).

The processed satellite images of 2005 for CDOM are presented in Fig. 3.22. Analysis of $a_{CDOM}(440)$ through satellite indicated an increase in its concentration in the lower zone of both the estuaries by the end of pre-monsoon season. The CDOM encountered during this season was less than that depicted during post-monsoon season. The pre-monsoon season depicts well mixed estuary. In a well-mixed estuary, CDOM concentration is expected to be greater than in a partially mixed estuary developed during post-monsoon season. However, this is not the case observed from the satellite images. In the pre-monsoon season, the region receives maximum irradiance and hence exhibits the highest sea surface temperature (SST) during April and May (Qasim, 2003). This might have resulted in the photo bleaching of CDOM and reduced CDOM concentration in both the estuaries.

There have been reports of *Trichodesmium* blooms in coastal waters of Goa during April (Devassy *et al.*, 1979). In addition, there are algal blooms along the west coast of India during the pre-monsoon season (Madhupratap *et al.*, 2001). This leads to the formation of the CDOM pool as the bloom degrades by May.

A reversal in the direction of the current, from poleward to equatorward might have advected CDOM rich waters to the Mandovi to a greater degree. Bhargava and

Dwivedi (1974) showed that an influx of neritic waters in the lower zone of both the estuaries render the region more productive during the pre-monsoon season. Hence, the advection of CDOM from the coastal region might be responsible for its greater incidence in the lower zones of the estuaries.
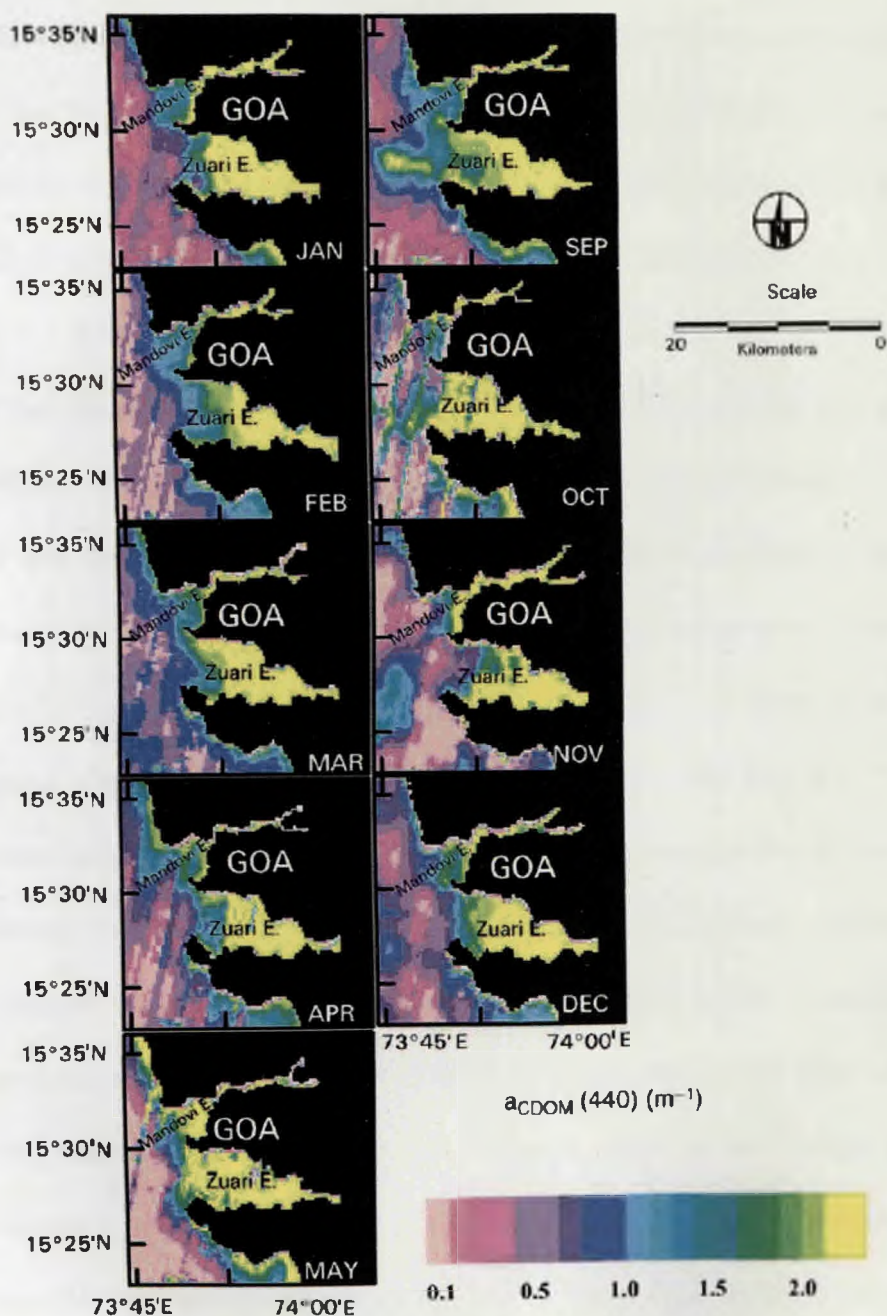
Fig. 3.22 Synoptic distribution of $a_{CDOM}(440)$ in Mandovi and Zuari estuaries during January - May 2005 and September - December 2005.

During the post-monsoon season, an elevated concentration of CDOM was observed in the middle zone, compared to that in the lower and upper zones of both the estuaries. This revealed that fresh water discharge was not the only source of CDOM during post-monsoon. The secondary mechanism to increase CDOM could be in-situ production through disintegration of Chlorophyll-a, resuspension of sediments or due to both these processes. However, phytoplankton does not produce CDOM directly but acts as a source of biomass which is transformed to CDOM through a microbially meditated process (Rochelle-Newall and Fisher, 2002).

Both the estuaries converge in the upstream and become narrow and shallow at the upper zone (Unnikrishnan et al., 1997). However, the converging degree is different for both estuaries. In the lower zone, the Mandovi estuary is 5.8 m deep and 3.2 km wide and decreases to 4.0 m depth and 0.8 km width in the middle zone. Similarly, the depth and width of the Zuari estuary decreases to 3.0 m and 1 km at the middle zone from 8.0 m depth and 5.5 km width at the lower zone. In the case of funnel shaped (converging type) estuaries like the Mandovi and Zuari, where the cross sectional area decreases upstream, the amplification due to convergence of the channel cancels decay due to friction, leaving the amplitude unchanged over long distances along the channels (Friedrichs and Aubrey, 1994). In such estuaries, when the monsoon recedes and fresh water discharge decreases, the effect of tide (sea water flux) becomes significant and the frictional effect at the bottom of the estuaries generates turbulence which is sufficient to break the monsoonal (salt-wedge) characteristics of the estuaries and convert them into partially mixed during post-monsoon. This mixing leads to resuspension of the bottom settled sediments which in turn induces release of CDOM in the middle zone of both the estuaries and augments its concentration during this season. The resuspension of sediments in the study area,

and clay) is fairly high, and on an average 25% of the particulate organic carbon sinking from the surface is derived from resuspended sediments (Bhaskar et al., 2000). This might also be responsible for the shedding of CDOM rich water from the middle zone of the Zuari estuary towards the offshore region. However, this type of secluded plume was not observed at the mouth of the Mandovi estuary. As the salt-wedge is formed in the lower zone (depth 5.8 m) of the Mandovi estuary, a momentum balance prevails between the fresh water (pressure-gradient) and friction. Hence, the tide generated bottom turbulence is not sufficient to break the wedge, which results in the gradual diffusion of CDOM from the lower zone of the Mandovi to the offshore region.

Apart from the estuarine region, OCM data also revealed the CDOM build up in the coastal inshore waters south of the Zuari estuary during October (Fig.3.23). Madhupratap et al. (2001) reported that the area between 8° N and 15° N. along the eastern Arabian sea is productive during the southwest monsoon During the fall inter-monsoon (October and November) period, CDOM concentration increased due to the disintegration of Chlorophyll-a. Moreover, the current reverses from equatorward to poleward during October. This might have acted as an agent to transport CDOM rich waters along the coastal inshore region south of the Zuari estuary. In their studies, Keith et al. (2002) indicated that phytoplankton utilise accessory pigments at longer wavelengths when the CDOM absorption is high and values of slope less than or equal to 0.02. This criterion holds well in the present case wherein the Mandovi estuary has higher CDOM concentration than the Zuari estuary. Published literature (Krishna Kumari et al., 2002) suggested that the Mandovi estuary is less productive than the Zuari estuary.

Analysis of CDOM using OCM data revealed that the seasonal hydrodynamics control the seasonal and spatial variability of CDOM in the Mandovi and Zuari estuaries. This is evident from the presence of more CDOM-rich waters in the lower zone and coastal inshore region of the estuaries by the end of pre-monsoon and accumulation of high CDOM waters in the middle zone of both the estuaries by the end of the post-monsoon season. Of the two estuaries, the Mandovi experiences a higher CDOM concentration and maximum variability. The study could also detect the secluded CDOM rich water (plume) in the offshore region during the initial phase of post-monsoon. It was observed that CDOM could be analysed synoptically through an optical sensor using a site-specific algorithm. Synoptic maps of CDOM can help in studying its temporal variation in estuaries. This in turn will help to monitor the discharge of dissolved organic matter.

Chapter 4.
Aerosol Variability and Atmospheric Correction

Atmospheric correction is a key factor in optical remote sensing of the oceanic waters. The atmospheric correction involves removal of aerosol and Rayleigh radiances (called path radiances) from each pixel of a satellite image. This is the most important step in satellite data processing as almost 85% of the radiance received by the sensor is contributed by atmosphere. In the open ocean waters, the radiance received by NIR bands is used for aerosol radiance correction as the water leaving radiance in these bands is zero owing to absorption of light by water at longer wavelengths. This is however, not the case for the coastal water bodies where the ←— longer wavelengths also contribute to L_w (Moore et al., 1999). This necessitates in-situ measurements of the aerosol optical thickness while dealing with remote sensing of coastal waters. The Rayleigh radiance (radiance from air molecules) can be correctly modeled from atmospheric pressure, sun zenith angle and azimuth angle (Gordon et al., 1988). However, modeling aerosol radiance is rather complicated due to the spatial and temporal variability of aerosol optical characteristics (Li and Ramanathan, 2002; Menon et al., 2011). The key component of the aerosol radiance is the aerosol optical thickness, which due to its variability over space and time has to be measured in-situ with hand held sunphotometer. There have been few successful attempts at mapping aerosol optical thickness synoptically using Mesosat-5 (Leon et al., 2001), NOAA - AVHRR (Rajeev and Ramanathan, 2002), MODIS - TERRA (Kaufman et al., 1997; Vinoj et al., 2004) and IRS - P4 - OCM (Das et al., 2002, Menon et al., 2011). These AOT maps can be used to apply correction for aerosol radiance and also to study the aerosol radiative forcing.

In the present study, the aerosol variability has been studied over the two estuaries. Since the satellite data of the year 2005 have been used to analyse the optically active constituent (OAC), the respective aerosol and Rayleigh radiances

65

have been computed for atmospheric correction. However, to explain the aerosol characterisitics, data derived during the year 2008 have been presented, this was done as many AOT measurements were possible which were uninterrupted by passing clouds.

4.1 Aerosol Optical Thickness

The spectral AOT ($\tau_a(\lambda)$) was measured at each station (clear skies) using a hand-held Microtops II Sunphotometer during all the field surveys. It has five bands (380±0.4 nm, 440±1.5 nm, 500±1.5 nm, 675±1.5 nm and 870±1.5 nm) and measures AOT with a field view of 2.5°. Through spectral analysis of AOT, aerosol size index (Ångström wavelength exponent, α) and Ångström turbidity factor (β) were derived using the following relation (Ångström, 1961, 1964).

$$\tau_a(\lambda) = \beta\lambda^{-\alpha} \tag{4.1}$$

hence,

$$\alpha = \ln\left[\tau_a(\lambda_1) / \tau_a(\lambda_2)\right] / \ln(\lambda_2 / \lambda_1) \tag{4.2}$$

Where, λ_1 and λ_2 are two different wavelengths on the exponentially decreasing curve of spectral AOT. In the present study, the two wavelengths selected were 675 nm and 870 nm.

The α is important for modeling the radiative effects of aerosol on any atmospheric layer retrieval of aerosol parameters from satellite remote sensing, atmospheric correction of satellite data and in identification of aeroso. source regions (O'Neill and Royer, 1993). The β, which accounts for the total atmospheric turbidity

due to aerosols, is also an important parameter in understanding the radiative processes in the atmosphere.
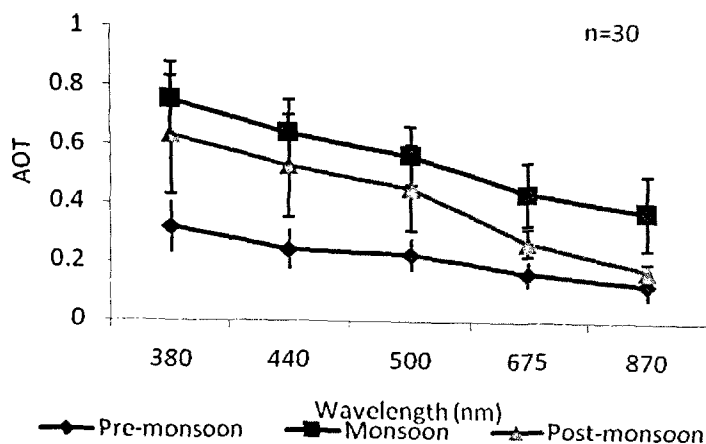
Fig. 4.1 Mean and standard deviation of spectral variation of AOT for three seasons. The vertical bars denote the standard deviation.

The AOT was measured for the field surveys carried out during the three seasons namely pre-monsoon, monsoon and post-monsoon. As Mandovi and Zuari estuaries are geographically very close to each other, one cannot expect a major difference in the aerosol properties over the two estuaries. Hence, the mean was taken over a season irrespective of the estuary surveyed.

The mean AOT showed a gradual decrease in the values from shorter to longer wavelengths. AOT values were the lowest in the pre-monsoon with mean AOT spectra ranging between 0.1 and 0.4 (Fig. 4.1). The AOT was the highest in the monsoon (AOT greater than 0.6 at all wavelengths) (Fig. 4.1). The post-monsoon season showed the values between 0.2 and 0.6 (Fig. 4.1). Comparison between the pre-monsoon and post-monsoon seasons revealed that the shorter wavelength (380 nm) values were two times higher in the post-monsoon than in the pre-monsoon, but

at the longer wavelength (875 nm) the values were almost similar. This means that fine mode aerosols are more pre-dominant in the post-monsoon than in pre-monsoon.

The general feature of AOT in clearest atmospheres is such that the AOT spectrum is flat and values are well below 0.1 at all wavelengths, whereas over turbid atmosphere close to coastal areas, the AOT shows a steep increase at shorter wavelengths resulting in a higher wavelength exponent, α (Jayaraman and Ramachandran, 2002). The same trend was observed in the present data.
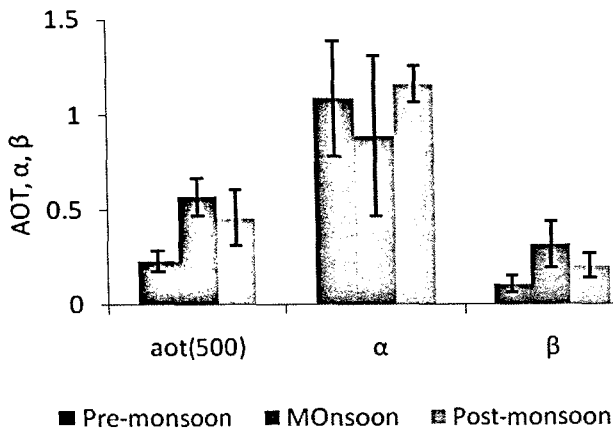
Fig. 4.2 Seasonal variation in mean AOT(500), α and β

It was observed that the Ångström wavelength exponent (α) varied inversely with the AOT while the Ångström turbidity factor (β) varied as per the AOT variation. The mean AOT was the highest in the monsoon (0.6±0.1) and lowest in pre-monsoon (0.24±0.04). Mean α was the highest in post-monsoon season (1.17±0.15) and lowest in the monsoon season (0.9±0.4) (Fig. 4.2). The mean β was the highest in the monsoon season (0.32±0.8) and lowest in the pre-monsoon season (0.1±0.03). The standard deviation of the AOT was the lowest in the pre-monsoon season and the same was observed for the β. However, the standard deviation of α is not small. α

68

depends on the slope of spectral decrease in the AOT. Therefore, it means that although the AOT values for the pre-monsoon season are close to each other, the variation at the shorter wavelengths is greater than at the longer wavelengths. This was observed from the standard deviation for the spectral AOT for the season (Fig. 4.1).

The lowest AOT values in the pre-monsoon are an indication of the clear skies in this season, followed by post-monsoon and then monsoon. Cloudy skies during the monsoon make it difficult to obtain accurate results and the high values can be attributed to the thin clouds or the hazy sky.

4.2 Aerosol and Rayleigh radiances

The atmospheric radiance is termed as path radiance (L_p (λ)) comprising both aerosol (L_a) and Rayleigh radiances (L_r, radiance from air molecules) and hence can be expressed as the sum of the two.

$$L_p (\lambda) = L_a (\lambda) + L_r (\lambda) \ [\mu w/cm^{-2}/nm/sr] \tag{4.3}$$

The equation for the path radiance was adopted from Gordon et al. (1988) as follows.

$$L_x = F_s. \ \tau_x \omega_{ox}. \ P_x \ / \ 4\pi \ cos \ (\theta_v) \ [\mu w/cm^2/nm/sr] \tag{4.4}$$

[x = a for aerosol and x = r for Rayleigh]

Where,

F_s (λ) is the extraterrestrial solar irradiance computed as per Doerffer (1992),

$$F_s (\lambda) = F_0 \ (1 + (0.0167* \ cos \ (2\pi \ (D-3)/TD)))^2 \tag{4.5}$$

F_0 is the average extraterrestrial irradiance for a year.

D = Julian day

TD = number of days in a year.

τ_x is the optical thickness,

τ_a was measured using the sunphotometer

$\tau_r = 0.0008735 \, \lambda^{-4.08} * P/1013.25$, P = atmospheric pressure

ω_{ox} is single scattering albedo ≈ 1

θ_v is the satellite view angle

P_x is the phase function computed as per Gordon *et al.* (1988) and Doerffer (1992).

$$P_x = P_x(\psi^-) + P_x(\psi^+) *(\rho\theta_v) + \rho \, \theta_s) \qquad (4.6)$$

P_a is a is the Two-term Henyey-Grenstein Phase function defined as

$$P_a(\psi\pm) = (1/4)\,[(1- g1^2)\,\alpha\,(1+ g1^2 - 2g1\,\cos\,\psi\pm)^{-1.5}+ (1- g2^2\,(1-\alpha)\,(1- g1^2+2$$

$$g2\,\cos\psi\pm)^{-1.5}]$$

g1, g2 are called the asymmetry factors taken as 0.8, 0.5 and α is constant equal to 0.98.

$P_r(\psi\pm) = 3/4\,(1 +\cos^2\,\psi\pm)$

$\psi\pm$ represents the forward and backward scattering angle,

$\cos(\psi\pm) = \pm\cos\theta_v\cos\theta_s - \sin\theta_v\sin\theta_s\cos\varphi$

θ_s is the sun zenith angle and φ is the azimuth angle.

ρ is the Fresnel's reflectance calculated as

$\rho(i) = 0.5\,[\{(\sin^2(i-j)/\sin^2(i+j)\} + \{\tan^2(i-j)/\tan^2(i+j)\}]$

Where, j is the angle of refraction derived from the equation sin (i)/sin (j)

=1.34 (refractive index of pure water).

The aerosol radiance and Rayleigh radiance were computed using a calibrated radiative transfer model (Menon, 2004).
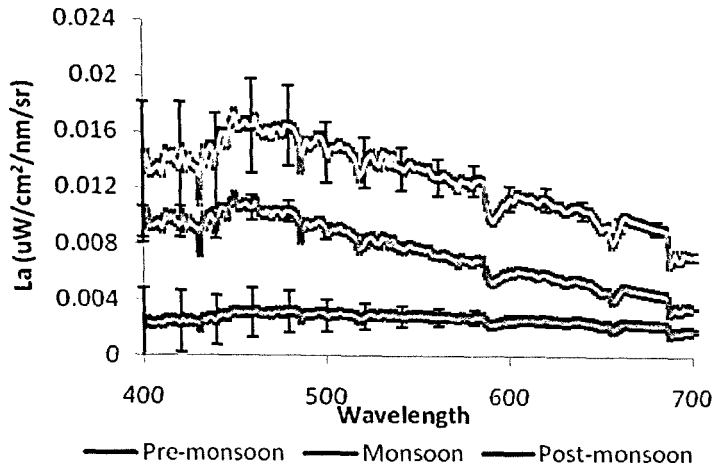
Fig. 4.3 Mean and Standard deviation of spectral variation of aerosol radiance (L_a) for pre-monsoon, monsoon and post-monsoon seasons

The aerosol radiance was minimum during the pre-monsoon season and maximum during the monsoon season. The spectral variation was similar for all the three seasons. The spectra showed a decrease from the shorter wavelength to longer wavelength region. The L_a for pre-monsoon ranged between 0.002 and 0.003 $\mu W/cm^2/nm/sr$; for monsoon between 0.006 and 0.016 $\mu W/cm^2/nm/sr$; for post-monsoon between 0.003 and 0.011 $\mu W/cm^2/nm/sr$. The maximum standard deviation was observed during monsoon season and minimum in post-monsoon season.
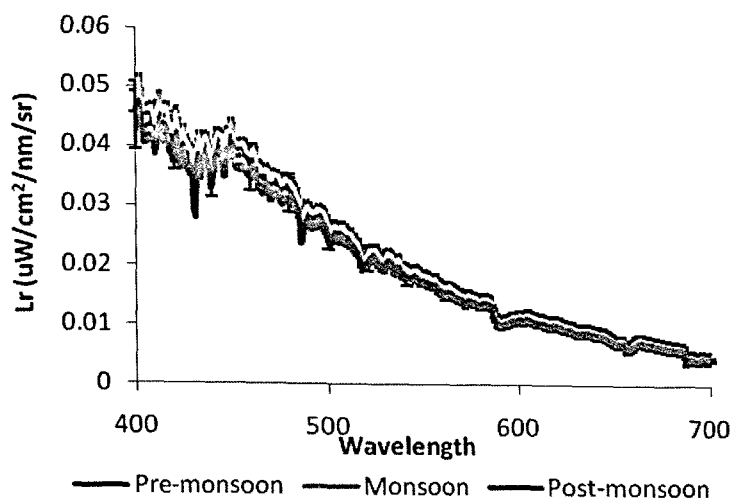
Fig. 4.4 Mean and standard deviation of spectral variation of Rayleigh radiance (L_r) during pre-monsoon, monsoon and post-monsoon seasons.

The Rayleigh radiance (L_r) for all the three seasons was in the similar range. L_r depends mainly on the atmospheric pressure. The atmospheric pressure does not vary much over a geographic location and hence the minor variations in the values. Thus the standard deviation was also very low.

The spectral variation was such that L_r decreased exponentially from the shorter wavelength to longer wavelength. The L_r for pre-monsoon ranged between 0.0046 and 0.042 $\mu W/cm^2/nm/sr$, for monsoon between 0.0047 and 0.013 $\mu W/cm^2/nm/sr$ and for post-monsoon between 0.0045 and 0.009 $\mu W/cm^2/nm/sr$ for post-monsoon seasons respectively.

Since the 2008 OCM data showed unusually high radiance values, the data could not be used for analyzing AOT. Hence, OCM data of the year 2005 was used.

The AOT and atmospheric pressure measurements were carried out during the 2005 field surveys. These values and other parameters described in section 4.2 were

calculated and were further used to compute the L_a and L_r using a calibrated radiative transfer model (Menon, 2004).

4.3 AOT retrieval from OCM data

An attempt was also made to map AOT from OCM data. The methodology adopted is as follows.

The radiance received by an optical sensor from turbid coastal waters at a specific band λ can be divided into different components as

$$L_t(\lambda) = L_p(\lambda) + t(\lambda) \times L_g(\lambda) + L_w(\lambda) \times T_d(\lambda) \tag{4.7}$$

$$\text{Where, } L_p(\lambda) = L_a(\lambda) + L_r(\lambda) \tag{4.8}$$

$L_p(\lambda)$ is the atmospheric path radiance, $L_g(\lambda)$ is the sun glint resulting from specular reflection from the sea surface and $L_w(\lambda)$ is the radiance leaving the water column. $T_d(\lambda)$ and $t(\lambda)$ are the diffuse and direct transmittance terms, respectively.

$L_r(\lambda)$ was removed from the $L_p(\lambda)$ of NIR bands of OCM. Theoretically, as water molecules absorb long-wave radiation, Rayleigh correction to pixels of NIR bands should yield L_a over oceanic waters. However, $L_w(\lambda)$ in NIR bands from the turbid coastal waters is non-zero (Moore *et al.*, 1999; Wang, 2007). In addition, radiance resulting from specular reflection [sun glint, $L_g(\lambda)$] contributes to radiance measured in the NIR bands. Therefore, $L_r(\lambda)$, $L_w(\lambda)$, and $L_g(\lambda)$ correction should be applied to NIR bands. $L_g(\lambda)$ correction was applied to the NIR bands as per Wang and Bailey (2001).

The water-leaving radiance correction to 765 nm pixels was applied using the remote-sensing reflectance at 765 nm [$R_{rs}(765)$], measured from the in-situ in-water radiometer measurements. The OAC effect on R_{rs} at 865 nm was computed using a

calibrated radiative transfer model (Menon, 2004) because the in-water radiometer does not have a band at this wavelength. The data revealed a direct relationship between reflectance and OAC concentration at 765 nm but not for 865nm band. Suspended organic and inorganic particles scatter and absorb light, whereas dissolved components only absorb it (Bricaud *et al.*, 1981; Menon *et al.*, 2005). A multiple regression analysis of $R_{rs}(765)$ with OAC revealed that neither Chlorophyll-a nor CDOM affects it, but that suspended sediment contributes to it at concentrations greater than 4 mg/l. Pixels with sediment concentration greater than 4 mg/l were corrected as follows. For pixels coinciding with station positions, the water-leaving radiance correction was applied by computing the respective radiance while for other pixels, the correction was applied to the mean of nine pixels adjacent to the station. Aerosol radiance (L_a) thus obtained could be expressed as

$$L_a(\lambda) = F_s(\lambda)\tau_a(\lambda)\omega_{oa} \times P_a/4\pi \cos(\theta_v) , \qquad (4.9)$$

Where, $F_s(\lambda)$ is the extraterrestrial solar irradiance,

$\tau_a(\lambda)=\beta\lambda^{-\alpha}$ is the AOT,

ω_{oa} the aerosol single-scattering albedo,

P_a the aerosol phase function, and

θ_v the satellite view angle.

Assuming that phase function and single-scattering albedo are spectrally invariant at a specific time over the short range of wavelength considered (765-865 nm), and taking the ratio of equation (4.9) for the two NIR bands of OCM, results in the following relation that can be used to map α from OCM:

$$\alpha = \log(L_a1/F_s1) - \log(L_a2/F_s2) \log(\lambda_2) - \log(\lambda_1) \qquad (4.10)$$

where,

L_a1 and L_a2 are aerosol radiances corresponding to 765 and 865 nm, respectively,

and

F_s1 and F_s2 are the respective extraterrestrial solar irradiances.

Another parameter required for the retrievalof AOT is β, the Ångström turbidity parameter. To retrieve β from OCM an algorithm was developed using results from a sensitivity analysis of a radiative transfer model (Menon, 2004), which is explained below.

Spectral (400-700 nm) aerosol radiances (L_a) were computed at 1 nm intervals for the range of β values (0.1–0.4) encountered over an Indian coastal station. While simulating aerosol radiances, the variables α, zenith angle, azimuthangle, atmospheric gaseous constituents, and OAC were held constant.Approximately 200 spectra of aerosol radiances were simulated for the wavelength range. The L_a corresponding to the least β was taken as the baseline spectrum; and all other L_a spectra were divided by this baseline. This demonstrated that maximum sensitivity to change in β was at 490 nm.
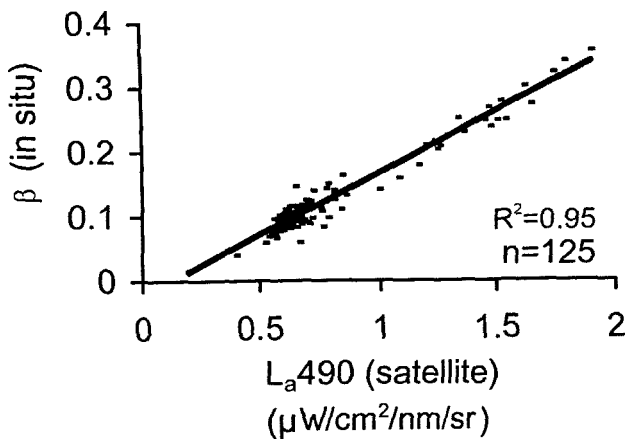
Fig. 4.5 Regression between in-situ β (Ångström turbidity parameter) and satellite-derived L_a 490 (aerosol radiance at 490 nm).

The following linear relationship was then obtained between satellite-derived $L_a(490)$ and in-situ derived β ($R^2 = 0.94$; Fig. 4.5):

$$\beta = 0.1925\ L_a(490) - 0.0242 \qquad (4.11)$$

In-situ data for alternate days were grouped into two sets and used for developing and validating the algorithm. Altogether, 125 observations were used. Subsequently, $L_a(490)$ from OCM was obtained by rearranging the ratio of equation (4.10) for 765 nm and shorter wavelengths, so as to allow computation of L_a for these wavelengths.

$$L_a(\lambda < 765nm) = L_a(765nm)\ [F_s(\lambda)/F_s(765nm)](\lambda/765)^{-\alpha} \qquad (4.12)$$

Where α is the value obtained using equation (4.10) derived from satellite data.
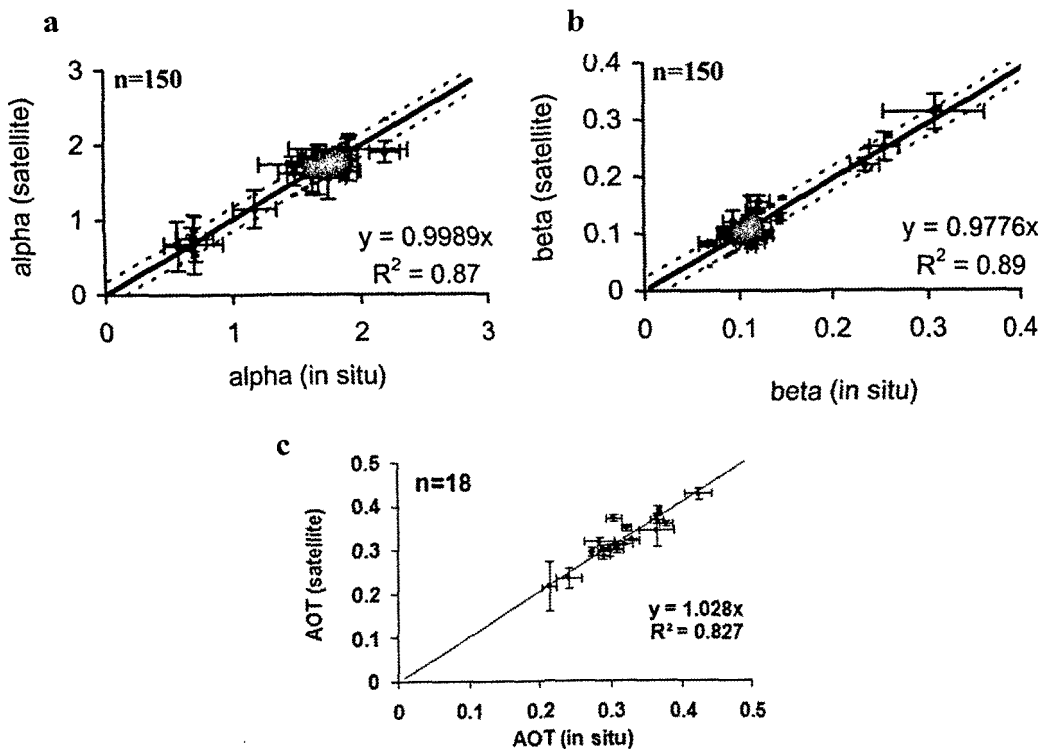
Fig. 4.6 Correlation between (a) satellite and in-situ derived alpha (α), (b) satellite-derived and in-situ beta (β), (c) satellite-derived and in-situ AOT values for validation. Dotted lines in (a) and (b) are the 95% confidence levels and vertical and horizontal bars representing the standard deviation.

OCM data for the year 2005 was processed to retrieve α and β parameters. The Ångström equation (Ångström, 1961) was then applied, and α and AOT values at 500 nm were retrieved. For validation of satellite-derived values, 150 observations were used. To avoid possible land interference in the estuarine region, only those observations taken at the mouth were considered for validation.

These results have given a new algorithm to retrieve aerosol parameters α and β from OCM to compute AOT over coastal turbid waters. These AOT values can be used to estimate aerosol radiance as a part of the complex atmospheric correction procedure.

Chapter 5.

Salinity retrieval from OCM data

Synoptic measurement of salinity from the coastal and estuarine waters is very important in the context of studies related to bio-geo-chemical cycles. It enables analysis of coupling between the estuarine mouth and the continental shelf and acts as a boundary condition in numerical simulation. Moreover, salinity acts as an important control on various types of pathogenic organisms and invasive species that inhabit a coastal waterway, plankton species that may occur in algal blooms (Kirst, 1995; Chan and Hamilton, 2001) and on the activity of nitrifying and denitrifying bacteria (Ryssgard et al., 1999). Increase in salinity also helps in reducing metal concentration by flocculation of clay minerals, which have high settling rate and can be studied to understand settling of suspended matter and clearing of water column (Elder, 1988). Therefore, it is quite evident that spatial distribution of salinity has multiple applications and hence, an attempt has been made to retrieve salinity from OCM data (OCM – I) to obtain a synoptic picture.

The method adopted doesn't generate salinity directly from the pixels of OCM data, rather it is an indirect way of using satellite-derived chromophoric dissolved organic matter (CDOM), one of the colour components, as a proxy to salinity (Nieke et al., 1997). Study of spatial distribution of CDOM and the associated dynamics in the coastal and estuarine waters is important in the context of optical remote sensing of water quality and the light climate in the water column. When the primary source of CDOM is riverine input, it behaves conservatively in the estuary. However, the conservative behaviour is not a universal feature. The departures from a linear CDOM-salinity curve may indicate mid-estuarine production (concave down) or removal (concave up) (Sholkovitz, 1978). This non-linearity may also be observed in case of temporal variations in the river input (Cifuentes et al., 1990). CDOM and

salinity relationship has been studied extensively in areas where the estuary displays a conservative behavior (Nieke *et al.*, 1997; Ferrari and Dowell, 1998; Bowers *et al.*, 2000; Gardner *et al.*, 2005; Kowalczuk *et al.*, 2010). This includes relationship of salinity with either CDOM absorption at 440 nm or 380 nm as per the area under consideration or CDOM fluorescence. An algorithm to retrieve CDOM from OCM was developed by Menon *et al.* (2006) and the same relation has been used to generate salinity from OCM

5.1 Salinity retrieval from the Mandovi and Zuari estuaries

As a first attempt, 2005 data set was used to check the feasibility for using satellite-derived CDOM to retrieve salinity. Here, absorption of CDOM at 440 nm ($a_{CDOM}(440)$) was used as a proxy to CDOM concentration.

Derivation of salinity from CDOM necessitated verification of the relation between them. Hence, regression was carried out between the two parameters (Fig. 5.1) using 40 data points. A good regression coefficient was obtained between salinity and CDOM (R^2=0.76, Fig. 5.1). The relationship observed between salinity and CDOM was:

$$Salinity = (- 2.5355 \times a_{CDOM}(440)) + 34.68 \tag{5.1}$$

The range of salinity values used to develop this relation was between 26 and 35 PSU as in the area covered for in-situ observation in 2005 (stations 07 to 18 in both estuaries) encountered these values.
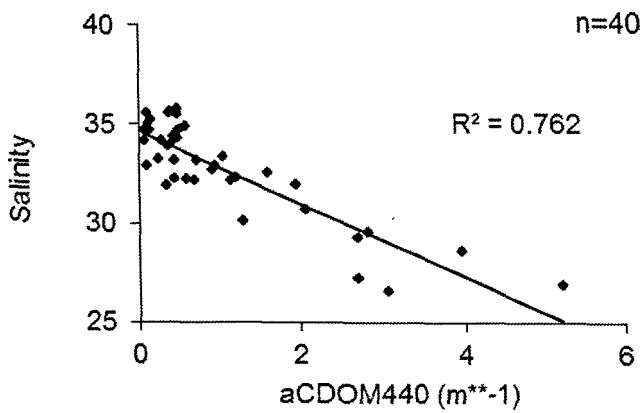
Fig. 5.1 Regression between CDOM and Salinity for 2005 data

From Fig. 5.1, it can be stated that the CDOM behaves conservatively in this study area and can be used to retrieve salinity from OCM data.

The algorithm developed by Menon *et al.* (2006) for CDOM retrieval was applied to the 2005 satellite data.

$$a_{CDOM} (440) = 2.9393 \ (L_w412/L_w670)^{-2.2486} \qquad (5.2)$$

$L_w(412)$ and $L_w(670)$ are water leaving radiances at 412 nm and 670 nm, respectively

Validation of in-situ and satellite-derived CDOM values was observed to be good (R^2=0.86, RMS log error=14.25% and bias=3.89%) (Fig. 5.2)
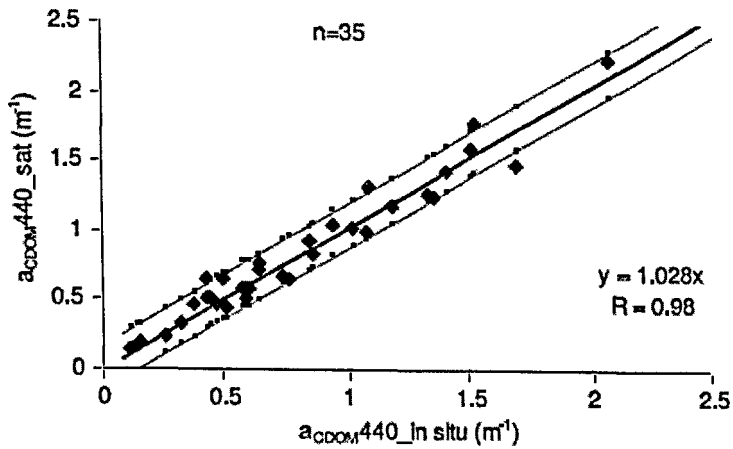
Fig. 5.2 Validation of satellite derived salinity with in-situ values for the year 2005.

Subsequently, equation 5.1 was applied to the CDOM values of each pixel in the satellite image to retrieve and map salinity.
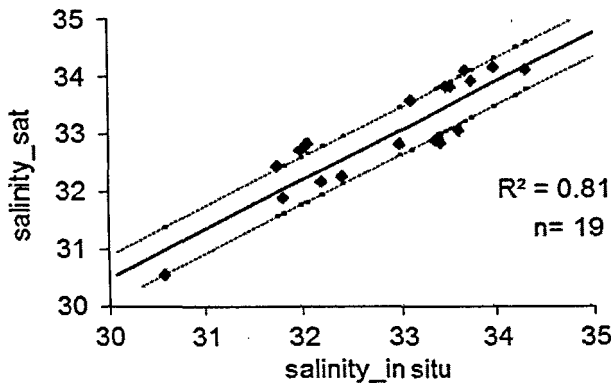
Fig. 5.3 Validation of satellite derived salinity with in-situ values for the year 2005.

For the validation of the derived salinity values, the data points were chosen from the area of the estuaries where the width of the stations was more than 3 times the spatial resolution of OCM (360 m). This was done to avoid interference of land pixels. Hence, the validation could be applied to salinity ranging from 30 PSU to 35 PSU. A good correlation ($R^2=0.81$, Fig. 5.3) between salinity retrieved from OCM

81

and in-situ values was observed. Further, a RMS log error of 14.25% and bias of 3.89% was observed for the relation. This revealed the strength of salinity algorithm (Menon and Sangekar, 2010).

Salinity for the entire 2005 year, except monsoon season, was retrieved from OCM data (Fig.5.3). Cloud-free scenes of OCM on 8th January, 12th February, 18th March, 13th April, 11th May, 23rd September , 6th October, 11th November and 9th December of the year 2005 were used to retrieve salinity and to study the spatial and temporal variability. However, due to cloud cover, the images for the monsoon season (June-August) could not be processed.

Fig. 5.4 shows satellite images of salinity of lower and middle zones of the estuaries for each month of the year 2005. The images clearly show the transformation in the salinity patterns between the months and seasons. The month of September represents the receding monsoon. The pre-monsoon season (February to May) displays the change in the salinity structure from partially mixed in February to completely homogeneous in May. This is also evident from the in-situ salinity profiles (Figs. 2.2 and 2.3). In the pre-monsoon, the fresh water flow is very low, and becomes negligible towards the end of the season. The satellite images match with the in-situ surface salinity where the lower zone shows higher values (32-35 PSU) and the upper-zone shows low values (less than 32 PSU).

Fig. 5.4 Spatial distribution of the Salinity using OCM images for different months of 2005.

In September, surface variability of salinity from the middle zone to the lower zone was observed in the satellite image in concurrence with the salinity profile (Fig. 2.3b). In addition, a small pool of low saline water was observed in the offshore waters.

After the monsoon, the salinity profile changed gradually to partially mixed type (September-October). In November, however, the salinity was observed to increase slightly towards the hinterland. In December, the partially mixed feature was observed again. This change in feature is due to the decreasing amount of the fresh water flow.

The image depicted values between 28 PSU - 34 PSU from the middle zone to the estuarine mouth in satellite data (Fig. 5.4). The same range was observed in the in-situ surface salinity (Figs. 2.1 and 2.3). It was also observed that the two estuaries behaved in a similar fashion throughout the year, although minor differences in salinity values could not be differentiated from the satellite data.

The synoptic picture of the salinity identified the gradual increase in salinity from head to mouth of both the estuaries. It also shows the change in estuarine mixing process from partially mixed in the post-monsoon to fully mixed in pre-monsoon season

This study was carried out as an extended part of the studies carried out by Menon *et al.* (2006) and observed to successfully retrieve salinity from the lower zone of the estuaries (Menon and Sangekar, 2010). The drawback of the study was that the low salinity values could not be validated. This is because the estuaries are converging type which makes them very narrow after just a few kilometres from the

lower zone, so that there is a possibility of contamination in the pixel radiance due to proximity of the land pixel (spatial resolution of the sensor is 360 m).

Overall, the algorithm proved to be helpful in deducing the surface salinity, but the main drawback was that it broke down in identifying values below 28 PSU -30 PSU. In view of this, the next step was to develop a relation (algorithm) for full range of salinity of the area. This is discussed in the following section.

5.2 Salinity retrieval for entire range (0 – 35 PSU) of the estuary

To derive the entire range of salinity for the two estuaries, the 2008 data set was used. As the OCM data for the year 2008 showed unusually high radiance values, it was not used to map salinity. Hence the analysis was carried out using in-situ data. Since salinity was derived from satellite-derived CDOM, it was necessary to highlight CDOM as a significant light absorbing component in the estuaries. This was examined through multiple regression analysis between (coefficient of downwelling irradiance at 490 nm) $k_d(490)$ and CDOM, Chlorophyll-a and TSM.

The high beta value and $p<0.001$ for the CDOM (for all the above three cases) (Table 5.1) shows that it was significantly responsible for attenuating the light in the water column. As CDOM only absorbs and does not scatter, it can be stated that CDOM is a significant absorbing component in these estuaries.

Table 5.1 Details of Multiple regression analysis between $k_d(490)$ and chlorophyll-a, TSM and CDOM for a) Mandovi, b) Zuari, c) Both estuaries

a)

Mandovi		St. Err.		St. Err.		
	Beta	of Beta	B	of B	t(110)	p-level
Intercept			0.6489	0.2442	2.6575	0.009045
CDOM	0.8777	0.0608	0.8877	0.0614	14.448	3.62E-27
Chlorophyll-a	0.0868	0.0588	0.0882	0.0598	1.4751	0.143034
TSM	0.0389	0.0198	0.0278	0.0142	1.9617	0.052317

b)

Zuari		St. Err. of		St. Err.		
	Beta	BETA	B	of B	t(122)	p-level
Intercept			-1.9055	0.9343	-2.0394	0.0436
CDOM	0.493	0.0955	0.4050	0.0784	5.1665	9.4E-07
Chlorophyll-a	0.445	0.0545	0.3669	0.0449	8.1649	3.3E-13
TSM	0.044	0.0896	0.0356	0.0721	0.4937	0.6224

c)

Both		St. Err.		St. Err.		
	Beta	of BETA	B	of B	t(231)	p-level
Intercept			-0.3225	0.4179	-0.7716	0.441127
CDOM	0.4886	0.0611	0.3443	0.0431	7.9968	6.12E-14
Chlorophyll-a	0.3955	0.0464	0.2696	0.0317	8.5169	2.12E-15
TSM	0.0349	0.0576	0.0186	0.0307	0.6059	0.545207

As observed in the table 5.1, CDOM behaves conservatively in the Mandovi and Zuari estuaries. However, the CDOM concentration from the river input (0 PSU) is not always constant and the slope of the regression line obtained can change seasonally. In addition, it can change geographically. To remove the effect of this variability, the normalized CDOM values, which is the ratio of $a_{CDOM}(440)$ to

normalized CDOM values, which is the ratio of $a_{CDOM}(440)$ to $a_{CDOM}(440)$ at 0 PSU needs to be used to develop relation between CDOM and salinity.

To develop a relation between CDOM and salinity and for further validation of the derived salinity, the entire data set was divided into two sets, one to establish relationship between salinity and normalized CDOM, and between salinity and CDOM and the other for validation.
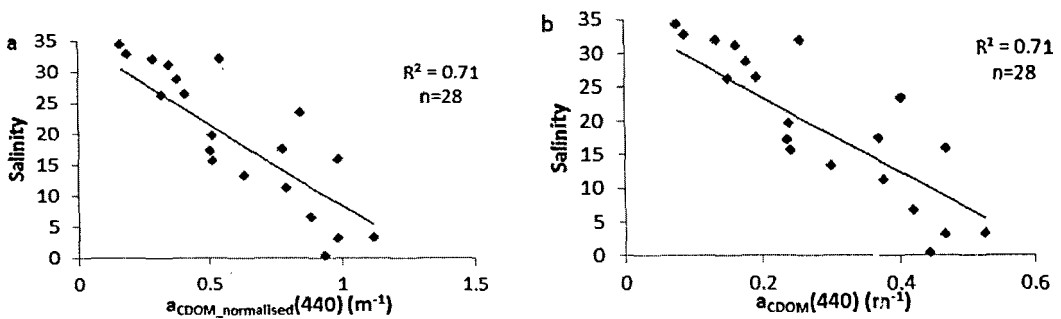
Fig. 5.5. Regression between a) salinity and normalized CDOM and b) salinity and CDOM

Fig. 5.5 shows the regression between salinity and CDOM for Mandovi and Zuari estuaries. A good correlation coefficient (R^2= 0.71) was obtained.

The equations are

$$\text{Salinity} = -26.108 * a_{CDOM}(440)_{normalised} + 34.68 \qquad (5.3)$$

$$\text{Salinity} = -55.372 * a_{CDOM}(440) + 34.68 \qquad (5.4)$$

The difference between equations 5.3 and 5.4 lies only in the coefficient of the equation.

The above equations were applied to $a_{CDOM\_normalized}(440)$ and $a_{CDOM}(440)$ of the second set to obtain salinity. The derived salinity values were compared with the in-situ values (Fig. 5.5)
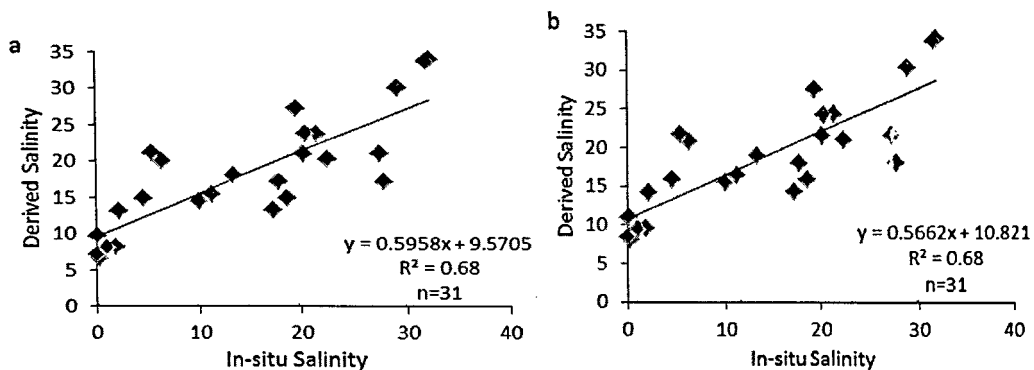
Fig. 5.5 Regression between derived salinity and in-situ salinity derived from a) $a_{CDOM\_normalized}(440)$ (normalized) and b) $a_{CDOM}(440)$

The good regression coefficient ($R^2=0.68$) shows that CDOM can be used to derive salinity for the entire range of salinity. In addition, the RMS error and the log normal bias obtained were 18.43% and 24.12%, respectively which accentuates the relationship. The only difference obtained between using normalized and non-normalized CDOM values to derive salinity was the difference in the offset.

For the salinity-CDOM relation to work, it was necessary that CDOM absorbs significantly in a water body. From the multiple regression between $k_d(490)$ and CDOM, Chlorophyll-a and TSM it was evident that CDOM absorbs significantly in the water column. Thus, the feasibility of using CDOM to retrieve salinity for the entire range in the estuary was established.

The relationship obtained depicted an offset in the derived values. The offset is due to the over-estimation of the low salinity values. The off-set was also observed for the normalized CDOM relation. By normalizing CDOM with the zero salinity

value, the effect of the difference in the CDOM values at the zero-salinity is removed. However, the mixing of the CDOM in the water needs to be studied more precisely, so as to know if the CDOM mixing is conservative in each zone of the estuary, especially the upper zone where most of the discrepancy was observed in the derived salinity. This necessitates extensive studies of CDOM mixing in the study area.

However, due to the exceptionally high OCM radiance during the year 2008, the CDOM–salinity relationship could not be retrieved from OCM values of this year.

Chapter 6.
Summary and Conclusion

6.1 Summary

The study was undertaken in the Mandovi and Zuari estuaries owing to their optical complexity and lack of detailed study of optical characterisation. The study area covered region up to 35 km and 40 km from the mouth of Mandovi and Zuari estuaries respectively and it was divided into three zones on the basis of the hydrodynamics prevailing in the water-column. The measurements were carried out to facilitate optical characterisation of the estuaries, derive L_a and L_r for atmospheric correction, map AOT using OCM data and map salinity using OCM data. In-water radiometric measurements were carried out using hyperspectral radiometer to generate AOP, while water sample analyses were carried out to derive IOP.

The analysis of OAC revealed seasonal variability in their concentrations and absorption spectra. The Zuari estuary displayed high chlorophyll-a values compared to Mandovi in all three seasons. The pre-monsoon TSM concentration was high in the lower and the middle zones as compared to Mandovi, while in the lower zone, concentrations were in the similar range. The monsoon season exhibited high TSM concentration in Zuari, while post-monsoon season exhibited similar concentration in both the estuaries. The CDOM absorption in Mandovi during the pre-monsoon exhibited high concentrations in the upper and lower zone, while during the monsoon season the concentration was high in the upper zone and decreased towards the lower zone. The post-monsoon season showed similar values in all three zones. The Zuari estuary did not show any zonal variability. However, pre-monsoon season displayed highest values and the other two seasons showed values in similar range.

The R_{rs} was used to optically characterise the two estuaries with the help of absorption budgeting and concentrations of the OAC. The optical complexity was well-evident both within the estuary and between the two estuaries. Both the estuaries displayed highly diverse optical environment. The influence of monsoon on the optical signature (R_{rs}) was clearly demonstrated especially in the upper zone of the Mandovi estuary where the peak is observed at 690 nm and the peak value co-varied with the TSM concentration in that zone. In Zuari estuary, however, this feature was not observed though the concentration of TSM was greater than in Mandovi. Another interesting feature observed was the flat spectrum at three stations (M13, M14 and M15) in the lower zone of Mandovi estuary during post-monsoon season. These three stations exhibited high TSM concentration in the zone which was attributed to resuspension of the bottom sediments. All the spectra in the lower zone exhibited typical coastal water characteristics with a peak at 586 nm and suggested the absence of the material present in the upper zone.

It was observed that the seasonal and spatial variation in the R_{rs} was evident more from its spectral characteristics instead of its magnitude. The two estuaries displayed highly diverse R_{rs} characteristics. It was thus shown that the optical environment of the two estuaries is highly complex though the two estuaries lie in the same geographical regime.

The analyses of the normalised absorption by the three OAC revealed the differential behaviour of the OAC absorption in the two estuaries. The Mandovi estuary was more dominated with TSM absorption compared to Zuari estuary in all the three seasons. In Zuari, however, the CDOM absorption was observed to be more prominent than the Mandovi. In addition, the effect of CDOM was more towards the lower zone of the estuary. The upper zone depicted more absorption by TSM.

Derivative analysis (partial differentiation (∂R_{rs}) was carried out for R_{rs} with respect to the absorption coefficient by the three OAC. The derivative analysis did not reveal any absorption band for chlorophyll-a due the very low absorption displayed by chlorophyll-a. The second order derivative of the R_{rs} with respect to TSM absorption revealed absorption at 555 nm. The ratio of $R_{rs}(740)/ R_{rs}(555)$ was observed to correlate well with the TSM concentration. However the same could not be validated using satellite data.

The ratio $R_{rs}(412)/ R_{rs}(670)$ was regressed with $a_{CDOM}(440)$ for the present data set and it revealed a good coefficient ($R^2=0.62$). Hence, the algorithm developed by Menon et al. (2006) was used to map CDOM from OCM data for the year 2005 and study the hydrodynamics of the estuarine system. The derived CDOM values validated well with the in-situ values ($R^2 = 0.98$, RMS log error $= 14.25\%$ and log difference bias $= 3.89\%$). It was observed that CDOM can be analysed synoptically through an optical sensor using a site-specific algorithm.

The seasonal AOT, α, β, L_a and L_r were studied for the study area. The highest AOT and L_a were observed in the monsoon season and least in the pre-monsoon season. An attempt was made to derive AOT from the OCM data. The results have given a new algorithm to retrieve aerosol parameters α and β from OCM to compute AOT over coastal turbid waters. The satellite derived and in-situ α, β and AOT validated well with the in-situ values.

A successful attempt was made to derive salinity from OCM data using CDOM as proxy for a range (26 - 35 PSU). The algorithm proved to be helpful in deducing the surface salinity and study the hydrodynamics of the estuaries. An attempt was made to develop a relation for the entire range of salinity observed in the estuaries (0- 35 PSU). In this case, though the relationship could be obtained, the

derived values showed and offset from the actual values. To reduce this offset, further investigation is required to understand the source and conservative behaviour of CDOM on which the relation is based.

6.2 Conclusion

The Mandovi and Zuari are the two most important rivers of Goa. Large scale iron ore mining is carried out in Goa and the ore transport is mainly carried out using barges through Mandovi and Zuari. The Mandovi estuary has heavy traffic of ships used for recreation (hotels, joy rides, casinos). The Marmugao port is at the mouth of the Zuari estuary. Owing to all the above factors, both the estuaries are prone to heavy pollution even though the reports state that these are two of the least polluted estuaries of India. The estuaries are also a house for a large number of species of both flora and fauna. This study was able to establish the optical complexity of the two estuaries for the first time.

The regular monitoring is thus necessary on a synoptic scale to maintain and improve the health of these estuaries. The study revealed the ability of the optical sensor (OCM) in deriving AOT. The study also revealed the ability of using CDOM as a proxy to derive salinity from OCM data. The optical remote sensing has emerged as a promising tool to facilitate the monitoring of these estuaries.

The optical environment of the estuaries was observed to be affected more by TSM and CDOM. The reflectance characteristics of the water column are seen to display the changes due to the difference in the suspended matter. The in-situ hyperspectral measurements combined with hyperspectral satellite sensors will be

able to derive the TSM concentrations and the R_{rs} signals may pave way to distinguish at least the general types of suspended material types.

Bibliography

Aguirre-Gomez R., Weeks A.R. and Boxall S.R. (2001) The identification of phytoplankton pigments from absorption spectra; International Journal of Remote Sensing, 22(2&3), 315 - 338.

Ångström A. (1961) Techniques of determining the turbidity of the atmosphere; Tellus, 13, 214 - 223.

Ångström A. (1964) The parameters of atmospheric turbidity; Tellus, 16, 64 - 75.

Atkins W.R.G. and Poole H.H. (1933) The photoelectric measurement of penetration of light of various wavelength into the sea and the physiological bearing of the results; Philosophical Transactions of the Royal Society, London, Series B, 222, 129.

Baker K.S. and Smith R.C. (1979) Quasi-inherent characteristics of the diffuse attenuation coefficient for irradiance; Society for Photo-Optical Instrumentation Engineering, 208, 60 - 63.

Bhargava R.M.S. and Dwivedi S.N. (1974) Diurnal variation in phytoplankton pigment in Zuari estuary, Goa; Indian Journal of Marine Sciences, 3, 142 - 145.

Bhaskar P.V., Cardozo E., Giriyan A., Garg A. and Bhosle N.B. (2000) Sedimentation of particulate matter in the Dona Paula Bay, West Coast of India during November to May 1995-1997; Estuaries, 23, 722 - 734.

Bhaskar P.V and Bhosle N.B. (2008) Bacterial production, glucosidase activity and particle-associated carbohydrates in Dona Paula bay, west coast of India; Estuarine, Coastal and Shelf Science, 80, 413 - 424.

Bouman H.A., Platt T., Kraay G.W., Sathyendranath S. and Irwin B.D. (2000) Bio-optical properties of the subtropical North Atlantic. 1. Vertical variability; Marine Ecology Progress Series, 200, 3 - 18.

Bowers D.G., Harker G.E.L., Smith P.S.D. and Tett P. (2000) Optical properties of a region of freshwater influence (the Clyde Sea); Estuarine, Coastal and Shelf Science, 50, 717 - 726.

Bricaud A., Morel A. and Prieur L. (1981) Absorption by dissolved organic matter of the sea (yellow substance) in the UV and visible domains; Limnology and Oceanography, 26, 43 - 53.

Bukhari S.S. and Nayak G.N. (1996) Clay minerals in identification of provenance of sediments in Mandovi Estuary, Goa, West coast of India; Indian Journal of Marine Sciences, 25, 341 - 345.

Carder K.L., Reinersman P.H., Chen R.F. and Muller-Karger F. (1993) AVIRIS calibration and application in coastal oceanic environments; Remote sensing of Environment, 44, 205 - 216.

Chan T.U. and Hamilton D.P. (2001) Effect of freshwater flow on the succession and biomass of phytoplankton in a seasonal estuary; Marine and Freshwater Research, 52, 869 - 884.

Chen Z., Curran P. and Hansom J. (1992) Derivative reflectance spectroscopy to estimate suspended sediment concentration; Remote Sensing of Environment, 40, 67 - 77.

Cifuentes L.A., Schemel L.E. and Sharp J.H. (1990) Qualitative and numerical analyses of the effects of river inflow variations on mixing diagrams in estuaries; Estuarine, Coastal and Shelf Science, 30, 411 - 427.

Clarke G.L. (1933) Observation on penetration of daylight into mid-Atlantic and coastal waters; Biological Bulletin, 65, 317 - 337.

Cleveland J.S. and Weidemann A.D. (1993) Quantifying absorption by aquatic particles: Multiple Scattering correction for glass fibre filter; Limnology and Oceanography, 38 (6), 1321 - 1327.

Das I., Mohan M. and Krishnamoorthy K. (2002) Detection of marine aerosols with IRS - P4 - Ocean Colour Monitor; Proceedings of the Indian Academy of Sciences (Earth and Planetary Science), 111 (4), 425 - 435.

Darecki M., Olszewski J. and Kowalczuk P. (1995) A preliminary study of the spectral characteristics of the upward radiance field in the surface layer of the Baltic - an empirical algorithm for remote detection of chlorophyll concentration; Studies in Material Oceanology, 68, 27 - 49.

Darecki M., Weeks A., Sagan S., Kowalczuk P. and Kaczmarek S. (2003) Optical characteristics of two contrasting Case 2 waters and their influence on remote sensing algorithms; Continental Shelf Research, 23, 237 - 250.

Darecki M. and Stramski D. (2004) An evaluation of MODIS and SeaWiFS bio-optical algorithms in Baltic Sea; Remote Sensing of Environment, 89, 326 - 350.

Devassy V.P., Bhattathiri P.M. and Qazim S.Z. (1979) *Trichodesmium* phenomenon; Indian Journal of Marine Sciences, 8 (June), 89 - 93.

Doerffer R. (1992) Imaging Spectroscopy for Detection of Chlorophyll and Suspended Matter; In GKSS 92/E/54, 215 - 257.

Dowell M.D. (1998) Optical characterisation and reflectance modelling in Case II waters: quantitative tools for investigations of coastal environments; Ph.D., University of Southampton, Southampton, UK, 192 p.

Doxaran D., Froidefond J.M., Lavender S. and Castaing P. (2002a) Spectral signature of highly turbid waters - Application with SPOT data to quantify suspended particulate matter concentrations; Remote Sensing of Environment, 81, 149 - 161.

Doxaran D., Froidefond J.M. and Castaing P. (2002b). A reflectance band ratio used to estimate suspended matter concentrations in coastal sediment-dominated waters; International Journal of Remote Sensing, 23: 5079 - 5085.

Doxaran D., Froidefond J.M. and Castaing P. (2003) Remote-sensing reflectance of turbid sediment dominated waters. Reduction of sediment type variations and changing illumination conditions effects by use of reflectance ratios; Applied Optics, 42 (15), 2623 - 2634.

Doxaran D., Chrukuru R.C.N. and Lavender S.J. (2005) Use of reflectance band ratios to estimate suspended and dissolved matter concentrations in estuarine waters; International Journal of Remote Sensing, 26 (8), 1763 - 1769.

Elder J.F. (1988) Metal Biogeochemistry in Surface-Water Systems - A Review of Principles and Concepts. U.S. Geological Survey Circular 1013.

Ferrari G.M. and Dowell M.D. (1998) CDOM Absorption Characteristics with Relation to Fluorescence and Salinity in Coastal Areas of the Southern Baltic Sea; Estuarine, Coastal and Shelf Science, 47 (1), 91 - 105.

Ferrari G.M., Bo F.G. and Babin M. (2003) Geo-chemical and optical characterizations of suspended matter in European coastal waters; Estuarine, Coastal and Shelf Science, 57, 17 - 24.

Friedrichs C.T. and Aubrey D.G. (1994) Tidal propagation in strongly convergent channels; Journal of Geophysical Research, 99, 3321 - 3336.

Froidefond J.M., Castaing P., Mirmand M. and Ruch P. (1991) Analysis of the turbid plume of the Gironde (France) based on SPOT radiometric data; Remote Sensing of Environment, 36, 149 - 163.

Froidefond J.M., Gardel L., Guiral D., Parra M. and Ternon J.F. (2002) Spectral remote sensing reflectances of coastal waters in French Guiana under the Amazon influence; Remote Sensing of Environment, 80, 225 - 232.

Gardner L.R., Thombs L. and Nelson D. (1989) Time series analysis of Suspended Sediment concentrations at North Inlet, South Carolina; Estuaries, 12 (4), 211 - 221.

Gardner G.B., Chen R.F. and Berry A. (2005) High-resolution measurements of chromophoric dissolved organic matter (CDOM) in the Neponset River Estuary, Boston Harbor, Massachusetts; Marine Chemistry, 96 (1-2), 137 - 154.

Gershun A. (1936) O fotometrii mutnykk sredin; Trudy Gosudarstvennogo Okeanograficeskogo Instituta, 11, 99.

Gershun A. (1939) The light field; Journal of Mathematical Physics, 18, 51 - 151.

Goodin D.G., Fraser R.N., Rundquist, D.C. and Stebbins W.A. (193) Analysis of suspended solids in water using remotely sensed high resolution derivative spectra; Photogrammetric engineering and remote sensing, 59, 505 - 510.

Gordon H.R. and McCluney W.R. (1975) Estimation of the Depth of Sunlight Penetration in the Sea for Remote Sensing; Applied Optics, 14, 413 - 416.

Gordon H.R. and Morel A. (1983) Remote Assessment of Ocean Color for Interpretation of Satellite Visible Imagery: A Review, New York: Springer-Verlag, 114 p.

Gordon H.R., Brown J.W. and Evans R.H. (1988) Exact Rayleigh scattering calculations for use with the Nimbus-7 Coastal Zone Color Scanner; Applied Optics, 27, 862 - 871.

Green S. and Blough N. (1994) Optical absorption and fluorescence properties of chromophoric dissolved organic matter in the natural waters; Limnology and Oceanography, 39, 1903 - 1916.

Hallegraeff G.M. (1993) A review of harmful algal blooms and their apparent global increase; Phycology, 32, 79 - 99.

Hoge F.E. and Swift R.N. (1987) Ocean color spectral variability studies using solar-induced chlorophyll fluorescence; Applied Optics, 26 (1), 18 - 21.
doi: 10.1364/AO.26.000018

Jayaraman A. and Ramachandran S. (2002) In situ study of aerosol characteristics over the Arabian Sea and Indian Ocean of relevance to correction of satellite remote sensed data; Advances in Space Research, 25 (5), 1045 - 1049.

Jerlov N.G. and Liljequist G. (1938) On the angular distribution of submarine daylight and the total submarine illumination; Svenska Hydrografisk-biologiska Kommissiones, Skrifter. Ny serie: Hydrografi, 14, 15.

Jerlov N.G. (1976) Marine Optics, Elsevier Oceanography Series 14. 2nd Edition. Amsterdam, Oxford, New York: Elsevier Scientific Publishing Company, 231p.

Kalle K. (1938) Zum problem der Meereswasserfarbe; Annal der Hydrologie u Marine Meteorologie, 66, 1 - 13.

Kaufman Y.J., Tanre D., Gordon H.R., Nakajima T., Lenoble J., Frouin R., Grassl H., Herman B.M., King M.D., Teillet P.M. (1997) Passive remote sensing of tropospheric aerosol and atmospheric correction for the aerosol effect. Journal of Geophysical Research, 102 (D4), 16815 - 16830.

Keith D.J., Yoder J.A., Freeman S.A. (2002) Spatial and temporal distribution of coloured dissolved organic matter (CDOM) in Narragansett Bay, Rhode Island: implications for Phytoplankton in coastal waters; Estuarine, Coastal and Shelf Science, 55 (5), 705 - 717.

Kessarkar P.M., Rao V.P., Shynu R., Mehra P., Viegas B.E. (2010) The nature and distribution of particulate matter in the Mandovi Estuary, Central West coast of India; Estuaries and Coasts, 33, 30 - 44.

Kirk J.T.O. (1994) Light and Photosynthesis in aquatic ecosystem. Cambridge: Cambridge University Press, 509 p.

Kirst G.O. (1995) Influence of salinity on algal ecosystems. In: W. Wiessner, E. Schepf and C. Starr (Eds.), Algae, Environment and Human Affairs, Bristol, England: Biopress, pp. 123 - 142.

Knudsen M. (1922) On measurement of penetration of light into the sea; Conseil Permanent International pour L'exploration de la Mer, Publications de Circonstance, 76, 1 - 16.

Kostadinov T.S., Siegel D.D., Marimorena S. and Guillocheau N. (2007) Ocean color observations and modeling for an optically complex site: Santa Barbara Channel, California, USA; Journal of Geophysical Research, 112, C07011. doi: 10.1029/2006JC003526.

Kowalczuk P. and Kaczmarek S. (1996) Analysis of temporal and spatial variability of Yellow Substance absorption in the southern Baltic; Oceanologia, 38 (1), 3 - 32.

Kowalczuk P., Sagan S., Olszewski J., Darecki M. and Hapter R. (1999) Seasonal changes in selected optical parameters in the Pomeranian bay in 1996-1997; Oceanologia, 41 (3), 309 - 334.

Kowalczuk P., Zablocka M., Sagan S. and Kulinski K. (2010) Fluorescence measured in situ as a proxy of CDOM absorption and DOC concentration in the Baltic Sea; Oceanologia, 52 (3), 431 - 471.

Krishna Kumari L., Bhattathiri P.M.A., Matondkar S.G.P. and John J. (2002) Primary productiviy in Mandovi-Zuari estuaries in Goa; Journal of Marine Biological Association of India, 44, 1 - 13.

Kratzer S., Bowers D. and Tett P.B. (2000) Seasonal changes in colour ratios and optically active constituents in optical Case II waters of Menai Strait, North Wales; International Journal of Remote Sensing, 21 (11), 2225 - 2246.

Leon J.F., Chazette P., Dulac F., Pelon J., Flamant C., Bonazzola M., Foret G., Alfaro S.C., Cachier H., Cautenet S., Hamonou E., Gaudichet A., Gomes L., Rajot J.L., Lavenu F., Inamdar S.R., Sarode P.R., Kadadevarmath J.S. (2001) Large-scale advection of continental aerosols during INDOEX; Journal of Geophysical Research, 106 (D22), 28427 - 28439.

Li F. and Ramanathan V. (2002) Winter to Summer Monsoon Variation of Aerosol Optical Depth Over the Tropical Indian Ocean; Journal of Geophysical Research (Atmospheres); 107(D16), 4284, doi: 10.1029/2001JD000949, AAC 2-1 to AAC 2 - 13.

Liew S.C., Lin I.-I., Kwoh L.K., Holmes M., Teo S., Gin K. and Lim H. (1999) Spectral reflectance signatures of Case II waters: Potential for tropical algal bloom monitoring using satellite ocean colour sensors; Presented at 10th JSPS/VCC joint seminar on Marine and Fisheries Sciences, Melaka, Malaysia, 29 Nov - 1 Dec 1999.

Madhupratap M., Nair K.N.V., Gopalakrishnan T.C., Haridas, P., Nair, K.K.C., Venugopal, P. and Gauns M (2001) Arabian sea oceanography and fisheries of the west coast of India; Current Science 81 (4), 355 - 361.

Magnuson A., Harding L.W. Jr., Mallonee M.E. and Adolf J.E. (2004) Bio-optical model for Chesapeake Bay and the Middle Atlantic Bight; Estuarine, Coastal and Shelf Science, 61, 403 - 424.

Menon H.B. (2004) Calibration of an optical equation to analyse the atmospheric turbidity and water quality of an estuarine environment; Photonirvachak, Journal of Indian Society of Remote Sensing, 32, 287 - 300.

Menon H.B., Lotliker A.A. and Nayak S.R. (2005) Pre-monsoon bio-optical properties in estuarine, coastal and Lakshadweep waters; Estuarine Coastal and Shelf Science, 63, 211 - 223.

Menon H.B., Lotliker A.A. and Nayak S.R. (2006) Analysis of estuarine colour components during non-monsoon period through Ocean Colour Monitor; Estuarine, Coastal and Shelf Science, 66, 523 - 531.

Menon H.B. and Sangekar N.P. (2010) Measurement of salinity of Mandovi and Zuari estuarine waters from OCM data; Indian Journal of Geo-Marine Sciences, 39 (4), 504 - 508.

Menon H.B., Sangekar N.P., Lotliker A.A., Krishnamoorthy K. and Ponnumani V. (2011) Aerosol optical thickness and spatial variability along coastal and offshore waters of the eastern Arabian sea; ICES Journal of Marine Science, 68 (4), 745 - 750. doi:10.1093/icesjms/fsq191.

Miller R.L., Del Castillo C.E. and McKee B.A. (2005) Remote sensing of coastal aquatic environments: technologies, techniques and applications; Dordrecht: Springer, 355 p.

Moore G.F., Aiken J. and Lavender S.J. (1999) The atmospheric correction of water colour and the quantitative retrieval of suspended particulate matter in case 2 waters applications to MERIS; International Journal of Remote Sensing (MERIS Special Issue), 20, 1713 - 1737.

Morel A. and Prieur L. (1977) Analysis of variations in ocean colour; Limnology and Oceanography, 22, 709 - 722.

Morel A. (1988) Optical modelling of the upper ocean in relation to its biogenous matter content (case I waters); Journal of Geophysical Research, 93 (C9), 10749 - 10768.

Morel A. and Ahn Y.H. (1991) Optics of heterotrophic nanoflagellates and ciliates: a tentative assessment of their scattering role in oceanic waters compared to those of bacterial and algal cells; Journal of marine Research, 49, 177 - 202.

Morel A. and Antoine D. (1997) Pigment index retrieval in Case 1 waters; ATBD 2.9 - MERIS Workshop, Villefranche-sur-mer, 2-3 Oct 1997.

Morris A.W. and Howarth M.J. (1998) Bed stress induced sediment resuspension (SERE 88/89); Continental Shelf Research, 18, 1203 - 1213.

Muller J.L. and Austin R.W. (1995) Ocean Optics protocols for SeaWiFs validation, Revision 1. In: S.B. Hooker, E.R. Firestone and J.G. Acker (Eds.) NASA technical Memorandum 104566, 25, Greenbelt, MD: NASA, pp. 1 - 67.

Murthy C.S., Das P.K., Nair R.R., Veerayya M. and Varadachari V.V.R. (1976) Circulation and sedimentation process in and around the Aguada bar; Indian Journal of Marine Sciences, 5, 9 - 17.

Naqvi S.M. (2005) Geology and evolution of the Indian Plate (from Hadean to Holocene-4 Ga to 4 Ka); New Delhi: Capital Press, 450 p.

Nieke B., Reuter R., Heuermann R., Wang H., Babin M. and Therriault J.C. (1997) Light absorption and fluorescence properties of chromophoric dissolved organic matter (CDOM) in the St. Lawrence estuary (case 2 waters); Continental Shelf Research, 17, 235 - 252.

Olszewski J., Kowalczuk P. and Darecki M. (1999) In-water remote sensing algorithms for chlorophyll and yellow substances in the Pomeranian bay; Oceanologia, 41 (3), 461 - 474.

O'Neill N. and Royer A. (1993) Extraction of bimodal aerosol-size distribution radii from spectral and angular slope (Ångström) coefficients; Applied Optics, 32(9), 1642 - 1645.

O'Reilly J.E., Maritorena S., Mitchell B.G., Siegel D.A., Carder K.L. and Garver S. A. (1998) Ocean color chlorophyll algorithms for SeaWiFS; Journal of Geophysical Research, 103, 24937 - 24953.

O'Reilly J.E., Maritorena S., Siegel D., O'Brien M.C., Toole D., Mitchell B.G., Kahru M., Chavez F.P., Strutton P., Cota G., Hooker S.B., McClain C.R., Carder K.L., Muller-Karger F., Harding L., Magnuson A., Phinney D., Moore G.F., Aiken J., Arrigo K.R., Letelier R. and Culver M. (2000). Ocean color chlorophyll a algorithms for SeaWiFS, OC2, and OC4: Version 4. In: S.B. Hooker and E.R. Firestone (Eds.), SeaWiFS Postlaunch Technical Report Series, Volume 11, SeaWiFS Postlaunch Calibration and Validation Analyses, Part 3; Greenbelt, Maryland: NASA, Goddard Space Flight Center, pp. 9 - 23.

Petus C., Chust G., Gohin F., Doxaran D., Froidefond J.M. and Sagarminaga Y. (2010). Estimating turbidity and total suspended matter in the Adour Rives Plume (South Bay of Biscay) using MODIS 250-m imagery; Continental Shelf Research, 30, 379 - 392.

Pope R.M. and Fry E.S. (1997) Absorption spectrum (380 - 700 nm) of pure water II integrated cavity measurement; Applied Optics, 36, 8710 - 8723.

Prabhu Matondkar S.G., Gomes H.R., Parab S.G., Pednekar S. and Goes J.I. (2007) Chapter 6 - Phytoplankton diversity, biomass, and production. In: S.R. Shetye, M.D. Kumar and D. Shankar (Eds.), The Mandovi and Zuari estuaries; Goa, India: National Institute of Oceanography, pp. 67 - 82.

Prieur L. and Sathyendranath S. (1981) An optical classification of coastal and oceanic waters based on the specific spectral absorption curves of phytoplankton pigments, dissolved organic matter, and other particulate materials; Limnology and Oceanography, 26, 671 - 689.

Qasim S.Z. and Sengupta R. (1981) Environmental characteristics of the Mandovi-Zuari estuarine system in Goa; Estuarine, Coastal and Marine Science, 13, 557 - 578.

Qasim S.Z. (2003) Mandovi-Zuari System; In: S.Z. Qasim (Ed.), Indian Estuaries; New Delhi: Allied Publishers, 277 p.

Rajeev K. and Ramanathan V. (2002) The Indian Ocean Experiment: aerosol forcing obtained from satellite data; Advances in Space Research, 29, 1731 - 1740.

Rochelle-Newall E.J., Fisher T.R. (2002). Production of chromophoric dissolved organic matter fluorescence environment in marine and estuarine environment: in investigation into the role of phytoplankton; Marine Chemistry, 77 (1), 7 - 22.

Roux L.L., Roux S. and Appriou P. (1998) Behaviour and Speciation of Metallic Species Cu, Cd, Mn and Fe during Estuarine Mixing; Marine Pollution Bulletin, 36 (1), 56 - 64.

Rysgaard S., Thastum P., Dalsgaard T., Bondo Christensen P. and Sloth N.P. (1999) Effects of salinity on NH_4^+ adsorption capacity, nitrification, and denitrification in Danish Estuarine sediments; Estuaries, 22 (1), 21 - 30.

Sathyendranath S. and Morel A. (1983) Light emerging from the sea - interpretation and uses in remote sensing. In: A.P. Cracknell (Ed.), Remote sensing aplications in marine science and technology; Dordrecht: D Reidel Publishing Company, pp. 323 - 357.

Sathyendranath S., Lazzara L. and Prieur L. (1987) Variations in the spectral values of specific absorption of phytoplankton; Limnology and Oceanography, 32, 403 - 415.

Sathyendranath S., Prieur L. and Morel A. (1989) A three component model of ocean colour and its application to remote sensing of phytoplankton pigments in coastal waters; International Journal of Remote Sensing, 10 (8), 1373 - 1394.

Sathyendranath S. (2000) Remote sensing of ocean colour in coastal, and other optically-complex waters. In: S. Sathyendranath (Ed.), Report of International Ocean Colour Coordinating Group, No. 3, IOCCG, Dartmouth, Canada, 140 p.

Schofield O., Arnone R.A., Bissett W.P., Dickey T.D., Davis C.O., Finkel Z., Oliver M., Moline M.A. (2004) Water colors in the Coastal Zone: What can we see?; Oceanography, 17(2), 25 - 31.

Shelford V.E. and Gail F.W. (1922) A study of light penetration into seawater made with the Kunz photoelectric cell with particular reference to the distribution of plants; Publications Puget Sound Biological Station, 3, 141 - 176.

Shetye S.R., Gouveia A.D., Singbal S.Y., Naik C.G., Sundar D., Michael G.S. and Nampoothiri G. (1995) Propagation of tides in the Mandovi-Zuari estuarine network; Proceedings of the Indian Academy of Sciences (Earth and Planetary Sciences), 104, 667 - 682.

Shetye S.R., Shankar D., Neetu S., Suprit K., Michael G.S. and Chandramohan P. (2007a) The environment that conditions Mandovi and Zuari. In: S.R. Shetye, M. Dileep Kumar and D. Shankar (Eds.), The Mandovi and Zuari Estuaries; Goa, India: National Institute of Oceanography, pp. 3 - 28.

Shetye S.R., Michael G.S. and Pradnya Vishwas C. (2007b) Mixing and intrusion of salt. In: S.R. Shetye, M. Dileep Kumar and D. Shankar (Eds.), The Mandovi and Zuari Estuaries; Goa, India: National Institute of Oceanography, pp. 49 - 58.

Sholkovitz E.R (1978) The flocculation of the Fe, Mn, Al, Cu, Ni, Co and Cd during estuarine mixing; Earth and Planetary Science Letters, 41, 77 - 86.

Shuleikin V.V. (1923) On the colour of the sea; Physical Review, 22, 86 - 100.

Shuleikin V.V. (1933) Data on optics of a strongly scattering medium applied to sea water, fog and cloud; Geofizika, 3, 3 - 5.

Siegel H., Gerth M. and Mutzke A. (1999) Dynamics of the Oder river plume in the Southern Baltic Sea: satellite data and numerical modelling; Continental Shelf Reasearch, 19, 1143 - 1159.

Stedmon C.A. and Markager S. (2003) Behaviour of the optical properties of coloured dissolved organic matter under conservative mixing; Estuarine, Coastal and Shelf Science, 57, 1 - 7.

Stramski D. and Kiefer D.A. (1991) Light scattering by microorganisms in the open ocean; Progress in Oceanography, 28, 343 - 383.

Strickland J.D. and Parsons T.R. (1972) A Practical handbook of Seawater Analysis; Bulletin of Fishery Research Board of Canada, 167, 310 p.

Stumpf R.P. and Pennock J.R. (1991) Remote estimation of the diffuse attenuation coefficient in a moderately turbid estuary; Remote Sensing of Environment, 38, 183 - 191.

Suprit K. and Shankar D. (2008) Resolving orographic rainfall on the Indian West Coast; International Journal of Climatology, 28, 643 - 657. doi: 10.1002/joc.1566

Szekielda K.H., Gobler C., Gross B., Moshary F. and Ahmed S. (2003) Spectral reflectance measurements of estuarine waters; Ocean Dynamics, 53, 98 - 102, doi: 10.1007/s10236-003-0027-x.

Takenouti Y. (1940) Angular distribution of submarine solar radiations and the effect of the altitude of the sun upon the vertical extinction coefficient. Bulletin of the Japanese Society for the Science of Fish ("Nippon Suisan Gakkaishi" in Japanese), 8, 213 - 219.

Tassan S. (1994) Local algorithms using SeaWiFS data for the retrieval of phytoplankton pigments, suspended sediments and yellow substance in coastal waters; Applied Optics, 33 (12), 2369 - 2378.

Tassan S. and Ferrari G.M. (1995) An alternative approach to absorption measurements of Aquatic particles retained on filter; Limnology and Oceanography, 40 (8), 1358 - 1368.

Tilstone G.H., Moore G.F., Sorensen K., Doerffer R., Rottgers R., Ruddick K.G., Pasterkamp R. and Jorgensen P.V. (2002) REVAMP, Regional Validation of MERIS Chlorophyll products in North Sea Coastal Waters, REVAMP Methodologies EVG1 - CT - 2001 - 00049.

Tzortziou M., Osburn C.L. and Neale P.J. (2007) Photobleaching of dissolved organic material from a tidal marsh-estuarine system of the Chesapeake Bay; Photochemistry and Photobiology, 83, 782 - 792.

Ulloa O., Sathyendranath S., Platt T. and Quinones R.A. (1992) Light scattering by marine heterotrophic bacteria; Journal of Geophysical Research, 97, 9619 - 9629.

Uncles R.J., Lavender S.J. and Stephens J.A. (2001) Remotely sensed observations of the turbidity maximum in the highly turbid Humber Estuary, UK; Estuaries, 24 (5), 745 - 755.

Unnikrishnan A.S., Shetye S. R. and Gouveia A.D. (1997) Tidal propagation in the Mandovi-Zuari Estuarine Network, West Coast of India: Impact of fresh water Influx; Estuarine, Coastal and Shelf Science, 45, 737 - 744.

Van der Linde D.W. (1998) Protocol for determination of total suspended matter in oceans and coastal zones, CEC - JRC - Ispra, Technical note no. I 98, 182 p.

Vinoj V., Babu S.S., Satheesh S.K., Moorthy K.K. and Kaufman Y.J. (2004) Radiative forcing by aerosols over the Bay of Bengal region derived from ship borne, island-based and satellite (Moderate-Resolution Imaging Spectroradiometer) observations; Journal of Geophysical Research, 109, D05203.

Voss R.J., Brummelhuis P.J.G. and Gerritsen H. (2000) Integrated data-modelling approach for suspended sediment transport in a regional scale; Coastal Engineering, 41, 177 - 200.

Wadia D.N. (1975). Geology of India (4th Edition); New Delhi: Tata McGraw-Hill Publishing Company Limited, 508 p.

Wang M. and Bailey S.W. (2001) Correction of sun-glint contamination on the SeaWiFS ocean and atmosphere products; Applied Optics, 40, 4790 - 4798.

Wang M. (2007) Remote sensing of the ocean contributions from ultraviolet to near-infrared using the shortwave infrared bands: simulations; Applied Optics, 46 (9), 1535 - 1547.

Whitney L.V. (1941) The angular distribution of characteristic diffuse light in natural waters; Journal of Marine Research, 4, 122 - 131.

Publications

Contents lists available at ScienceDirect

ISPRS Journal of Photogrammetry and Remote Sensing

journal homepage: www.elsevier.com/locate/isprsjprs

Dynamics of chromophoric dissolved organic matter in Mandovi and Zuari estuaries — A study through *in situ* and satellite data

Harilal B. Menon [a,*], Nutan P. Sangekar [a], Aneesh A. Lotliker [b], P. Vethamony [c]

[a] *Department of Marine Science, Goa University, P.O., 403 206, Goa state, India*
[b] *Indian National Centre for Ocean Information Services, Hyderabad, Andhrapradesh State, 500055, India*
[c] *National Institute of Oceanography, Dona Paula, Goa State, 403 003, India*

ARTICLE INFO

ABSTRACT

The spatial and temporal distribution of absorption of chromophoric dissolved organic matter at 440 nm ($a_{CDOM}(440)$) in the Mandovi and Zuari estuaries situated along the west coast of India, has been analysed. The study was carried out using remotely sensed data, obtained from the Ocean Colour Monitor (OCM) on board the Indian Remote Sensing satellite — P4, together with *in situ* data during the period January to December 2005. Satellite retrieval of CDOM absorption was carried out by applying an algorithm developed for the site. A good correlation ($R = 0.98$) was obtained between satellite derived CDOM and *in situ* data. Time series analysis revealed that spatial distribution of CDOM has a direct link with the seasonal hydrodynamics of the estuaries. The effect of remnant fresh water on CDOM distribution could be analysed by delineating a plume in the offshore region of the Zuari estuary. Though fresh water flux from terrestrial input plays a major role in the distribution of CDOM throughout the Mandovi estuary, its role in the Zuari estuary is significant up to the middle zone. Other processes responsible for feeding CDOM in both the estuaries are coastal advection, *in situ* production and resuspension of bottom settled sediments. The highest value of $a_{CDOM}(440)$ was observed in the middle zone of the Mandovi estuary during the post-monsoon season. The relation between $a_{CDOM}(440)$ and S (spectral slope coefficient of CDOM) could differentiate CDOM introduced in to estuaries through multiple sources. The algorithm developed for the Mandovi estuary is $S = 0.003 [a_{CDOM}(440)^{-0.7091}]$ while for the Zuari estuary, $S = 0.0031 [a_{CDOM}(440)^{-0.777}]$, respectively.

© 2011 International Society for Photogrammetry and Remote Sensing, Inc. (ISPRS). Published by Elsevier B.V. All rights reserved.

1. Introduction

Chromophoric dissolved organic matter (CDOM), commonly referred to as yellow substance, is one of the optically active substances responsible for the absorption of light, thus affecting the bio-optical properties of coastal and estuarine waters (Bricaud et al., 1981; Hojerslev and Aas, 2001; Menon et al., 2005; Foden et al., 2008). Having been introduced into the coastal environment through *in situ* production (decomposition of aquatic plants) and land drainage, CDOM significantly attenuates Photosynthetically Available Radiation (PAR) and thus affects the productivity of the area (Carder et al., 1989; Arenz et al., 1996; Vodacek et al., 1997; Magnuson et al., 2004; Odriozolaa et al., 2007). The effect of CDOM concentration can prevail in up to 650 nm of the optical spectrum of electromagnetic radiation, if it exists in a high concentration (Menon et al., 2005). Interest in the study of CDOM in coastal and estuarine waters has increased substantially in the recent past due to the role of CDOM as an indicator of areas which are a perennial source of CO_2 (Muller-Karger et al., 2005; Menon et al., 2006b). In the present context, this point is valid as the waters of the western Indian coast are identified as a region of hypoxia (Naqvi et al., 2000). Since the estuaries discharge to the western margin of the Indian subcontinent, it is pertinent to understand the spatial and temporal variation of CDOM in these estuaries. Data generated onboard trawlers in these estuaries were used for decades to characterise the phytoplankton and inorganic suspended matter dynamics (Singbal, 1973; Devassy and Goes, 1989; Padmavati and Goswami, 1996; Krishna Kumari et al., 2002). But these studies were often limited to a specific season with limited spatial coverage. A solution to this under-sampling is optical remote sensing of the estuarine waters. Menon et al. (2006a) were successful in developing algorithms to retrieve estuarine colour components, such as chlorophyll_a, sediment, and CDOM, from Ocean Colour Monitor (OCM) data. Though it is known that seasonal rainfall is the major contributor of CDOM to the Mandovi and Zuari estuaries, as the dynamics of the estuarine waters differ from season to season,

* Corresponding author. Tel.: +91 8326519350; fax: +91 832 2451184.
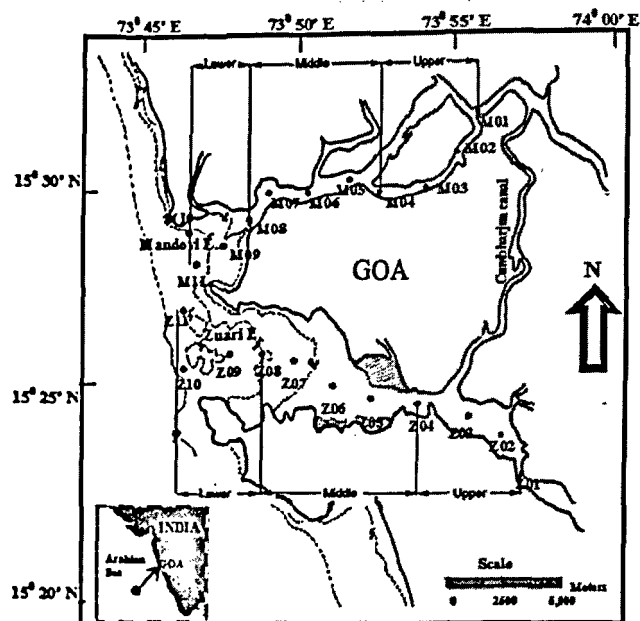 *E-mail addresses:* menonhb@bsnl.in, harilalm@gmail.com (H.B. Menon).

Fig. 1. Map of the study area showing hydrographic stations in different zones of Mandovi–Zuari estuaries of Goa.

it is imperative to know the augmented effect of these dynamics on the CDOM distribution. Nevertheless, no rigorous efforts were made in this direction until now. The present study is carried out with the following objectives:

(1) to analyse the temporal and spatial variability of CDOM in Mandovi and Zuari estuaries based on satellite and *in situ* data over a year.
(2) to characterise CDOM optical properties in water end-members in the study area through relations between CDOM absorption at 440 nm ($a_{CDOM}(440)$) and slope coefficient (S).

2. Data and methods

2.1. Study area

The Mandovi and Zuari estuaries in the state of Goa are complex ecosystems joining the Arabian Sea at the central west coast of India (Fig. 1). Estuarine hydrodynamics along the Indian coast is controlled by both river runoff and tides during the monsoon (June–September) season. After the withdrawal of the monsoon, runoff decreases rapidly and by November it reaches negligible levels. Subsequently, the flow propagated by the tide (semi-diurnal with a range 0.2–2 m), at the mouth, becomes the sole driving force of transport into the estuarine network. This initiates different hydrodynamic processes between dry (non-monsoon) and wet (monsoon) seasons, resulting in the formation of homogenous, salt-wedge and partially mixed estuaries during pre-monsoon (February–May), monsoon (June–September) and post-monsoon (October–January) seasons, respectively (Qasim, 2003). The cross-sectional area of both the estuaries decreases up-stream, classifying them under the converging category. This results in the influence of tides up to a distance of 50 km upstream (Shetye et al., 1995). As the catchment area of the Mandovi estuary is 1150 km², twice the area of the Zuari estuary (550 km²), the annual average fresh water discharge in the Mandovi is almost double that of the Zuari. Though the estuaries are interconnected by the Cumbarjua canal, its cross sectional area is too small to have any impact on the estuarine characteristics (Shetye et al., 1995).

2.2. In situ observations

Observations were carried out on 22 hydrographic stations on 12th February, 18th March, 13th April and 11th May (pre-monsoon), 15th August and 17th September (monsoon), on 11th November and 9th December (post-monsoon) seasons during the year 2005 (Fig. 1). Two water samples of 5 L each were collected from the subsurface of each station along the axis of the estuaries. Among these samples, one was used for the analysis of suspended matters such as chlorophyll_a and sediment and the other for CDOM. Along with the collection of water samples, observations were also carried out using a Secchi disk, Conductivity, Temperature and Depth (CTD) instrument, Microtops II sunphotometer, temperature and humidity meter at each station. The sampling details, selection of stations and the precautions taken in the field are discussed in Menon et al. (2005, 2006a).

2.3. Water sample analysis

The coefficient of CDOM absorption was determined by analysing the water samples as per the method used by Kowalczuk and Kaczmarek (1996). The samples were filtered through 0.2 μm Whatman cellulose membrane filters and the sample transparency was measured using a Perkin Elmer Lambda 35 UV/VIS spectrophotometer over the spectral range 400–700 nm with an interval of 1 nm against distilled water as a blank. Absorption coefficients were corrected for backscattering of small particles and colloids which pass through filters, as per Green and Blough (1994):

$$a_{corr}(\lambda) = a(\lambda) - a_{700}(\lambda/700) \qquad (1)$$

where $a_{corr}(\lambda)$ is the corrected absorption at a given wavelength λ and a_{700} is the measured absorption at 700 nm. The reference wavelength used to calculate $a_{CDOM}(\lambda)$ was 440 nm:

$$a_{CDOM}(\lambda) = a_{CDOM}(440) \exp(-S(\lambda - 440))(m^{-1}) \qquad (2)$$

where S is the slope coefficient, calculated as the slope of the curve resulting by plotting logarithm of $a_{CDOM}(\lambda)$ against wavelengths in the range 400–550 nm. The magnitude of $a_{CDOM}(440)$ was used as a proxy to the concentration of CDOM.

For estimating chlorophyll_a concentration, one sample from each station was filtered through glass fiber filter of 0.45 μm pore size. The pigment was extracted using 90% acetone in the dark at a low temperature. The Optical Density (OD) was then measured through a spectrophotometer, using a 1 cm cell, in the spectral range of 400–700 nm, with an interval of 1 nm, against the cell containing 90% acetone as a blank. The chlorophyll_a concentration was then calculated using trichometric equations as per Strickland and Parsons (1972).

Suspended sediment concentration was calculated using the method suggested by Strickland and Parsons (1972). Samples for estimating suspended sediments were filtered in the laboratory through a pre-weighed 0.45 μm Whatman membrane filter. The filters were dried in a hot air oven at 70 °C for 6 h and weighed again. Subsequently the concentrations were estimated.

2.4. Zonation of the estuaries

Spatial variability of salinity in the estuaries is the rationale behind the zonation. A haline front formed due to the convergence of sea water and river water is a permanent feature in the estuarine hydrodynamics. Hence, the characteristics and source of CDOM on the seaward side and riverward side of the front are different. Since the fronts migrate forwards and backwards during monsoon and non-monsoon seasons, an average position of the frontal zone is considered as the middle zone. In short, the seaward side of the front is the lower zone and riverward side of the front is the upper zone while the frontal zone itself is the middle zone (Fig. 1).
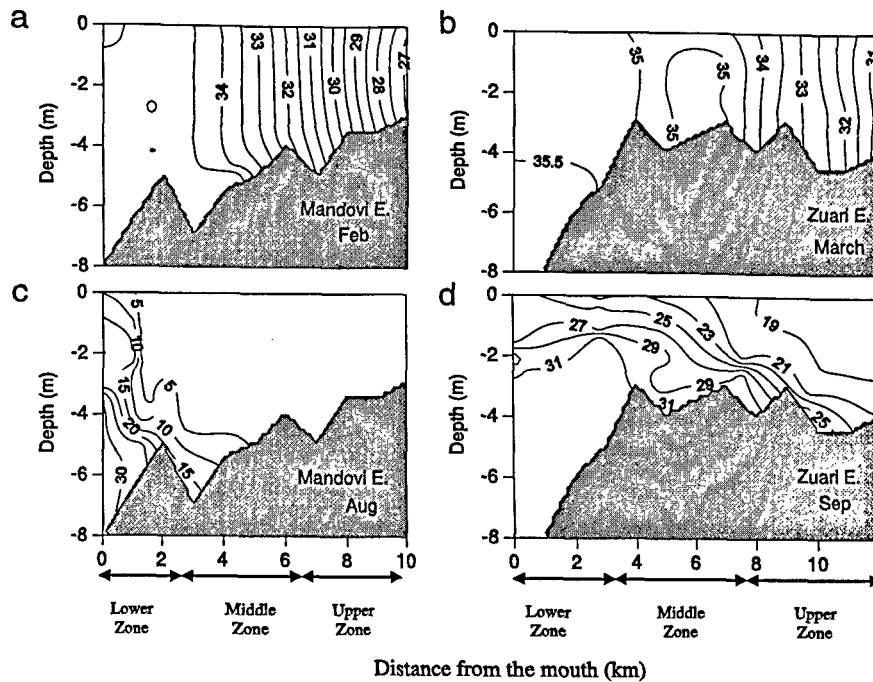
Fig. 2. Vertical sections of salinity along the axis of (a) Mandovi and (b) Zuari estuary during Pre-monsoon and (c) Mandovi and (d) Zuari estuary during Monsoon season.

2.5. Satellite data processing

Synoptic analysis of CDOM was carried out using the data obtained from the Ocean Colour Monitor (OCM) on board Indian Remote Sensing satellite-P4 (IRS-P4). OCM has six visible and two NIR bands in the range 402–885 nm centered at 412, 443, 490, 510, 555, 670, 765 and 865 nm. The spatial resolution and band-width of the visible bands of OCM are 360 m and 20 nm respectively. The images were geo-referenced using ground control points and the study area was extracted from the full scene through ERDAS Imagine 8.4. Atmospheric correction of remotely sensed data involves the elimination of Rayleigh and aerosol components. The Rayleigh component was computed and removed from each pixel using Doerffer's method (1992). As water in the study area was turbid, pixels of NIR bands of OCM could not be used to remove aerosol path radiance. Hence, aerosol radiance was computed by deriving aerosol optical depth (AOD) using a sunphotometer (Chylek et al., 2003) having filters at 380, 440, 500, 675 and 870 nm. Subsequently, aerosol correction was carried out on each pixel of OCM and water leaving radiance was derived for selected bands. Then the algorithm developed by Menon et al. (2006a) was applied to retrieve $a_{CDOM}(440)$ from OCM. This was carried out through a calibrated radiative transfer model (Menon, 2004; Menon et al., 2005). The algorithm developed to extract CDOM from the area of study was:

$$a_{CDOM}(440) = 2.9393(L_w412/L_w670)^{-2.2486} \qquad (3)$$

where, L_w412 and L_w670 are the water leaving radiances at 412 nm and 670 nm, respectively. Pixels from the upper zones of both the estuaries were contaminated by land radiance (widths of the estuaries are less than three times the spatial resolution of the OCM sensor). To analyse CDOM from this zone, in situ data supplemented satellite data. Similarly, in situ data were used to derive CDOM variability during the monsoon season. Cloud free scenes of OCM on 8th January, 12th February, 18th March, 13th April, 11th May, 23rd September, 6th October, 11th November and 9th December of the year 2005 were used to study the spatial and temporal variability of CDOM absorption.

3. Results

3.1. Seasonal distribution of salinity in the Mandovi and Zuari estuaries

3.1.1. Pre-monsoon season

The orientation of isohalines revealed that both Mandovi and Zuari estuaries are vertically homogeneous. Salinity encountered at the lower zone of Mandovi estuary was 34.5 while that at the corresponding zone of Zuari estuary was 35.5 PSU (Fig. 2(a) and 2(b)), indicating the dominance of sea water flux due to tide. A notable difference between the two estuaries is the gradient in salinity between middle and lower zones of the estuaries. The magnitudes of these gradients are 8 PSU and 4 PSU in the Mandovi and Zuari estuaries respectively.

3.1.2. Monsoon season

Fig. 2(c) clearly indicates the dominance of fresh water in the Mandovi estuary during this season. Fresh water is present between the lower and upper zones of Mandovi estuary and the salinity prevailing at the lower zone is 5 PSU. A wedge of sea water is seen intruding into the lower zone and exchange of water is restricted to the wedge. Salinity distribution at the bottom of the middle zone (4 km upstream from the mouth) shows stratification with a vertical gradient of 10 PSU.

Salinity profiles in the Zuari estuary are distinctly different from those in the Mandovi estuary. At the lower zone, the surface salinity is around 25 PSU (Fig. 2(d)). Saline water intrusion is up to the middle zone of the Zuari estuary. A vertical gradient of salinity with magnitude 8 is observed below 1 m from the surface and 10 km upstream from the lower zone.

Thus the changes in seasonal hydrodynamics of the estuaries are clear from their transformation from homogeneous into salt-wedge estuaries. Also, circulation in the Mandovi estuary is more fresh water dominant than that in the Zuari estuary.

3.2. OCM–in situ comparison

In order to validate satellite retrieved CDOM, in situ data were chosen in such a way that widths of the stations were more than

Table 1
Mean and Standard deviation of a_{CDOM}(440) at upper, middle and lower zones of Mandovi and Zuari estuaries. 24 data points, derived seasonally for each zone of the two estuaries were used for the analysis.

		Mandovi E.			Zuari E.		
		Upper	Middle	Lower	Upper	Middle	Lower
Pre-monsoon	Mean	0.67	0.67	1.02	0.71	0.67	0.86
	Stdev	0.44	0.48	1.00	0.26	0.26	0.47
Monsoon	Mean	0.66	0.66	0.66	0.38	0.53	0.11
	Stdev	0.19	0.19	0.49	0.07	0.49	0.08
Post-monsoon	Mean	0.71	2.00	1.40	0.73	1.69	0.49
	Stdev	0.43	1.80	0.85	0.45	0.60	0.45
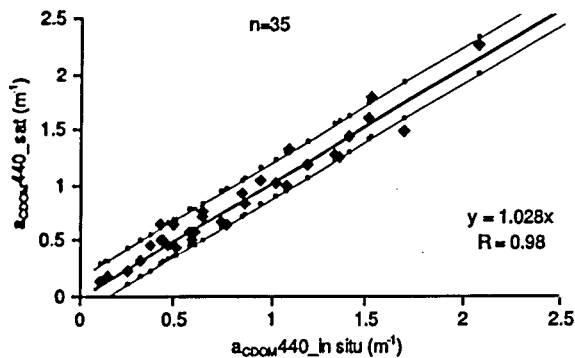
Fig. 3. Correlation between in situ and satellite derived a_{CDOM}(440) (the dotted line in the figure shows 95% confidence level).

three times 360 m, the spatial resolution of OCM. This precaution was taken to avoid overlapping of water pixels with land pixels. Along with the correlation analysis, root mean square (RMS) and bias of the data were also calculated. The data sets were logarithmically transformed (base 10) to calculate RMS and bias. The RMS log error is 14.25% and log difference bias is 3.89%. A good correlation, R equals 0.98 (Fig. 3), less error and bias further explained the ability of the algorithm to retrieve the sequential variation of CDOM concentration in association with the seasonally varying hydrodynamics of the estuaries.

3.3. CDOM optical properties

Mean values of a_{CDOM}(440) in the upper, middle and lower zones of both the estuaries along with the corresponding standard deviations are given in Table 1. From the table, it is apparent that the middle zones of both the estuaries encountered maximum CDOM absorption with highest standard deviations during the post-monsoon season. But during the pre-monsoon season, maximum absorption was seen at lower zones of both the estuaries and the standard deviation encountered at the lower zone of the Mandovi was three times that in the respective zone of the Zuari estuary. In short, the Mandovi estuary encounters more CDOM absorption than the Zuari estuary during all the seasons.

3.4. Spatial and temporal variability of CDOM through OCM data

An algorithm (Eq. (3)) to analyse CDOM from OCM, was developed for typical CDOM absorption variability range in the study area (0.1–2.2 m^{-1}). It worked well in this study except in December 2005, when exceptionally high values of a_{CDOM}(440) were recorded in the middle zone of both the estuaries (5.5 m^{-1} and 3.37 m^{-1} at stations M07 and Z05).

3.4.1. Pre-monsoon

The pre-monsoon distribution of CDOM is explained through OCM data of February, March, April and May (Fig. 4). By the end of the season (May), the lower zones of both the estuaries and coastal inshore region, north of the Mandovi and south of the

Zuari estuaries, encountered high CDOM. At the middle zone of the Mandovi estuary, CDOM decreased between March and May and absorption was around 0.6 m^{-1} in May. But the same was not observed in the Zuari estuary. Moreover, CDOM retrieved during May was found to be an overestimation in the Zuari estuary.

An important feature of the geometry of fairway channels of the estuaries is that their cross-sectional area and depth decreases rapidly in the upstream direction (Unnikrishnan et al., 1997). Hence, in a tidally controlled estuary during pre-monsoon, shoaling across the fairway channel (navigation channel) generates more turbulence and mixing, resulting in a homogenous estuary, as seen in Fig. 2(a) and (b). An overlapping of radiance from shoaling and those from the bottom of fairway channel might have resulted in an overestimation.

3.4.2. Post-monsoon

To study the effect of remnant fresh water on CDOM distribution, OCM data, during the period of receding phase of monsoon (September), were analysed. Fig. 4 depicts a uniform CDOM distribution between the upper and middle zone of the Mandovi estuary and thereafter decreases towards the lower zone. Though a similar pattern was exhibited between upper and middle zones of Zuari estuary, the distribution was different beyond the middle zone. Depiction of a sharp gradient in a_{CDOM}(440) at the middle zone and a secluded plume in the offshore region were the two distinct features.

During October, the lower zone of Zuari estuary encountered high CDOM absorption but in the respective zone of the Mandovi estuary it is low. It is also worth mentioning the CDOM build up at the coastal inshore waters south of the Zuari estuary during this month.

In November, there was a clear depiction of an increase in CDOM at the middle zones of both the estuaries. It also increased at the southern bank of the Mandovi estuary. But in the lower zone of the Zuari estuary, CDOM concentration is reduced considerably compared to earlier months. The plume observed at the offshore region of the Zuari estuary during September had diffused in November. In December, CDOM distribution showed highs and lows along the Mandovi estuary with a clear depiction of CDOM rich waters at the middle zone. Though CDOM concentration in the lower zones of both the estuaries increased compared to the previous month, the rate of increase was more in the Mandovi than in the Zuari estuary. During January, CDOM concentration in the lower zones decreased and showed uniform distribution at the middle and upper zones.

Overall, a distinct well defined variation in CDOM was not observed in the Zuari estuary and it was not possible to distinguish CDOM between the upper and middle zones of the Zuari estuary in December and January.

4. Discussion

The analysis revealed an intra-seasonal and inter-seasonal variability in the spatial distribution of CDOM between the two estuaries. Though situated adjacently in the same latitudinal belt, a discrepancy was seen in the absorption of CDOM between the
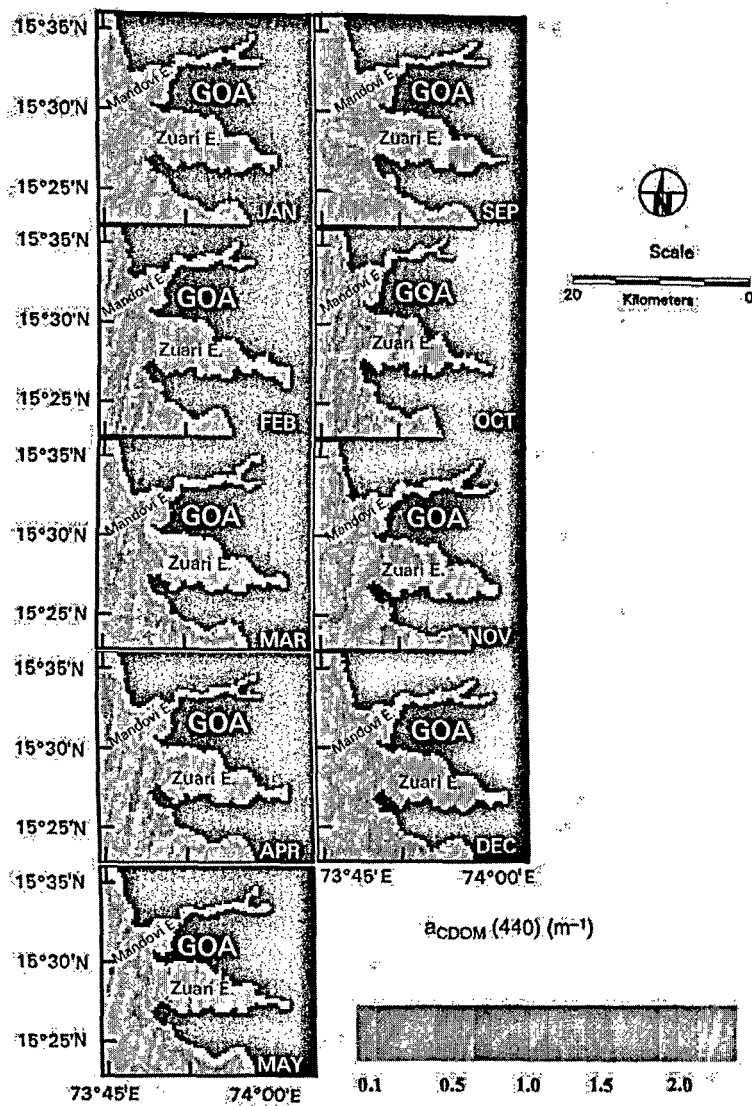
Fig. 4. Synoptic distribution of a_{CDOM}(440) in Mandovi and Zuari estuaries from January to May and September to December 2005.

two estuaries. To investigate this further, it is necessary to identify different processes (river input, advection and *in situ* production) acting as mechanisms to feed CDOM into each estuary. This was carried out by examining the relation between S, a proxy to the composition of CDOM, and a_{CDOM}(440), an index of concentration of CDOM. The relation is found to be different and the respective algorithm in each estuary is as follows:

In Mandovi estuary, $S = 0.003(a_{CDOM}(440))^{-0.7091}$ (4)

While in Zuari estuary, $S = 0.0031(a_{CDOM}(440))^{-0.777}$. (5)

The relation between S and CDOM absorption at 440 nm is inverse and exponential in both the estuaries ($R = -0.78$ in Zuari and $R = -0.78$ in Mandovi), (Fig. 5(a), (b)).

The maximum S observed in the Mandovi estuary is 0.022 nm^{-1} while in the Zuari estuary it is 0.044 nm^{-1}. An increase in S is due to the transformation of terrestrially derived CDOM and/or its replacement by *in situ* production of CDOM (Carder et al., 1989; Vodacek et al., 1997). Further, they pointed out that a change in the stratification of the area, during the period of the field survey, could also change S. Vodacek et al. (1997) explained that when terrestrially derived CDOM is present in surface waters under conservative mixing condition, S is less than or equal to 0.02 nm^{-1}.

4.1. Pre-monsoon

Analysis of a_{CDOM}(440) through satellite and *in situ* observations indicates an increase in its concentration in the lower zone of both the estuaries by the end of pre-monsoon season (May). Also, during this season, CDOM encountered at different zones of both the estuaries was less than that depicted during post-monsoon season. Table 2 gives the mean concentrations of chlorophyll_a and sediment encountered at lower, middle and upper zones during different seasons.

An examination of the contribution of chlorophyll_a and sediment to CDOM revealed that though a_{CDOM}(440) has a positive relation with chlorophyll_a and sediment in Mandovi estuary, the respective coefficients are poor (Table 3). This is clear from the weak negative relation of S with chlorophyll_a ($R = -0.37$) and sediment (-0.29). But the scenario prevailing in the Zuari estuary is different. Here a_{CDOM}(440) has a negative relation with chlorophyll_a ($R = -0.42$) and a weak positive relation with sediment ($R = +0.38$). The effect of sediment on CDOM could be ascertained from its strong negative linear relation with S ($R = -0.69$). This is also evident from the concentration of sediment prevailing in different zones of the estuaries during this season (Table 2).

Fig. 5. Regression between a_{CDOM}(440) and slope coefficient (S) in (a) Mandovi and (b) Zuari estuary.

Table 2
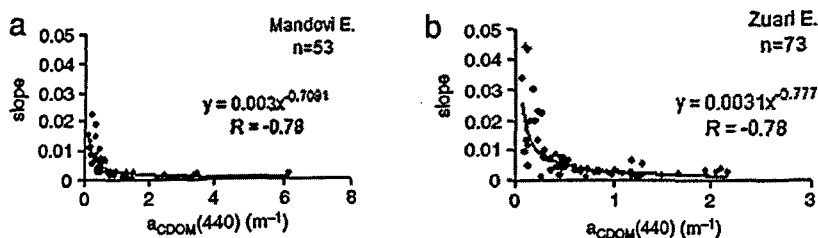Mean and standard deviation of chlorophyll_a and sediment concentrations at upper, middle and lower zones of the Mandovi and Zuari estuaries during different seasons. 24 data points, derived seasonally for each zone of the two estuaries were used for the analysis.

| | | Mandovi E. | | | | | | Zuari E. | | | | | |
| | | Chlorophyll (ug/L) | | | Sediment (mg/L) | | | Chlorophyll (ug/L) | | | Sediment (mg/L) | | |
		Upper	Middle	Lower	Upper	Middle	Lower	Upper	Middle	Lower	Upper	Middle	Lower
Pre-monsoon	Mean	9.70	6.32	3.72	13.95	20.37	16.03	6.68	5.95	3.63	22.82	22.72	14.45
	Stdev	6.07	2.35	1.08	3.30	4.11	6.44	3.33	2.55	1.68	7.41	10.71	3.85
Monsoon	Mean	7.00	2.45	4.59	18.63	18.13	14.00	6.61	3.68	4.88	18.20	18.00	12.00
	Stdev	0.14	1.03	0.08	2.11	0.35	0.18	1.48	2.80	0.18	5.83	0.20	0.80
Post-monsoon	Mean	3.13	2.90	1.50	5.48	8.41	10.15	2.37	2.14	1.41	10.21	16.74	8.27
	Stdev	2.51	1.13	0.95	2.49	1.35	1.56	2.01	0.97	1.01	3.63	6.30	3.67

Table 3
Regression coefficients, (R), between different parameters derived during pre-monsoon and post-monsoon seasons. Regression of a_{CDOM}(440) with sediment and chlorophyll_a and regression of slope coefficient (S) with salinity, sediment and chlorophyll_a.

| Parameters | Pre-monsoon | | Post-monsoon | |
	Mandovi	Zuari	Mandovi	Zuari
$a_{CDOM(440)}$ vs. sediment	$R = 0.12$ $n = 20$ Linear	$R = 0.38$ $n = 20$ Linear	$R = 0.81$ $n = 14$ Power	$R = 0.81$ $n = 14$ Linear
$a_{CDOM(440)}$ vs. chlorophyll a	$R = 0.23$ $n = 20$ Linear	$R = -0.42$ $n = 20$ Linear	$R = 0.72$ $n = 14$ Power	$R = 0.85$ $n = 14$ Linear
Slope vs. salinity	$R = -0.83$ $n = 20$ Linear	$R = 0.69$ $n = 17$ Linear	$R = -0.75$ $n = 14$ Linear	$R = 0.48$ $n = 14$ Linear
Slope vs. sediment	$R = -0.29$ $n = 20$ Linear	$R = -0.69$ $n = 20$ Linear	$R = -0.44$ $n = 14$ Linear	$R = -0.59$ $n = 14$ Linear
Slope vs. chlorophyll a	$R = -0.37$ $n = 20$ Linear	$R = 0.10$ $n = 20$ Linear	$R = -0.74$ $n = 14$ Linear	$R = -0.84$ $n = 14$ Linear

The salinity pattern along the axis of the estuaries categorises them under homogeneous estuaries during this season (Fig. 2(a) and (b)). In a well mixed estuary, CDOM should have been more than in a partially mixed estuary developed during post-monsoon season (Table 1). But this is not true in the present case. During the pre-monsoon season, being a period of clear sky, the area receives maximum irradiance and hence the highest sea surface temperature during April and May (Qasim, 2003). Therefore, photo bleaching during this season might have reduced CDOM concentration in both the estuaries.

An entirely different relation is seen between the estuaries with respect to the relation of S with salinity. In the Mandovi, the regression is linear and negative ($R = -0.83$) but in the Zuari, though the relation is linear, it is positive ($R = 0.69$). This means advection of coastal saline waters brings CDOM into the lower zone of Mandovi to a greater degree, but in the Zuari estuary this contribution is not significant. This might be the reason for high mean CDOM in the lower zone of the Mandovi than in the respective zone of the Zuari estuary. This is also evident from the large standard deviation in the lower zone of the Mandovi estuary during this period.

Devassy et al. (1979) reported trichodesmium blooms along the coastal waters of Goa (around 16° N) during April. In their studies, Madhupratap et al. (2001) reported that along the west coast of India (north of 15° N) algal blooms are formed during the pre-monsoon season. Hence CDOM pool builds up as the bloom senescence in May. A reversal in the direction of the current, from poleward to equatorward, might have advected CDOM rich waters to the Mandovi to a greater degree. Bhargava and Dwivedi (1974) showed that an influx of neritic waters in the lower zone of both the estuaries make the region more productive during the pre-monsoon season. Hence the advection of CDOM from the coastal region might be responsible for its greater incidence in the lower zones of the estuaries.

The advection of neritic waters is the sole source of CDOM in the lower zone of Zuari estuary while terrestrial input along with the advection of neritic waters are the sources of CDOM in the lower zone of the Mandovi. In their observations on CDOM dispersion over the Florida shelf, Del Castillo et al. (2000) had indicated the role of mixing in the distribution of CDOM. The above discussion has clearly revealed that the spatial and temporal variations of CDOM in these estuaries are controlled by the mixing process.
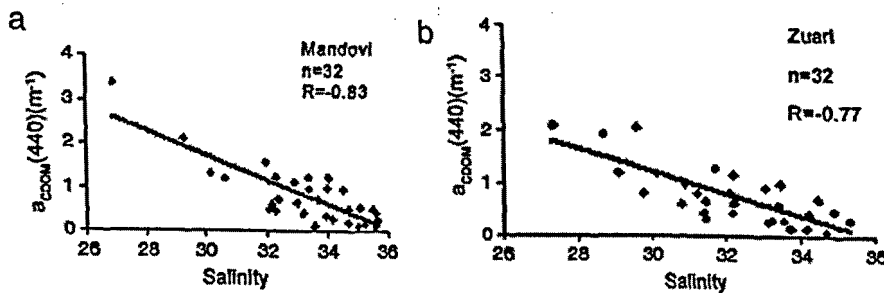
Fig. 6. Regression between $a_{CDOM}(440)$ and salinity in (a) Mandovi and (b) Zuari estuaries.

4.2. Monsoon

During the monsoon, the whole basin of the Mandovi is filled with fresh water and mixing with sea water takes place at the lower zone (salinity is 5 PSU). But in the Zuari estuary, mixing is at the middle zone and the salinity is 19 PSU (Fig. 2(c), (d)). Researchers found that the limit of seaward extent of terrestrially originated CDOM varies seasonally depending upon the magnitude of the fresh water (Vodacek et al., 1997; Rochelle-Newall and Fisher, 2002b). Uniform $a_{CDOM}(440)$ throughout the Mandovi estuary and a non-uniform distribution in the Zuari estuary is a clear indication that river discharge is the major mechanism to distribute terrestrially originated CDOM throughout the Mandovi estuary and up to the middle zone of the Zuari estuary.

An inverse linear relation between $a_{CDOM}(440)$ and salinity, with correlation coefficients −0.83 and −0.77 in the Mandovi and Zuari estuaries respectively further confirms the role of terrestrial input of CDOM in both the estuaries (Fig. 6(a), (b)).

4.3. Post-monsoon

An elevated concentration of CDOM in the middle zone, compared to that in the lower and upper zones of both the estuaries, revealed that fresh water discharge is not the only source of CDOM during post-monsoon. The secondary mechanism to increase CDOM could be in situ production through disintegration of chlorophyll_a, resuspension of sediments or due to both the processes.

A good relation of $a_{CDOM}(440)$ with chlorophyll_a ($R = 0.72$) and sediment ($R = 0.81$) in the Mandovi estuary and a strong linear relation with both chlorophyll_a ($R = 0.85$) and sediment ($R = 0.81$) in the Zuari estuary explicitly explains that both chlorophyll_a and sediment could contribute to CDOM absorption in both these estuaries (Table 3). Further, analysis revealed a negative linear relation between S and chlorophyll_a in the Mandovi ($R = -0.74$) and Zuari ($R = -0.84$) estuaries. Better regression of S with sediment ($R = -0.59$) in Zuari than in Mandovi ($R = -0.44$) is also observed. This indicates that sediment can act as an additional source of CDOM in the Zuari estuary.

On local scales, in situ production from phytoplankton decomposition and extraction from bottom sediments may be an important source of CDOM (Twardowski and Donaghay, 2001; Boss et al., 2001). However, in their studies, Rochelle-Newall and Fisher (2002a) showed that CDOM absorption doesn't correlate with chlorophyll_a content. Hence it has been proposed that phytoplankton does not produce CDOM directly but acts as a source of biomass which is transformed to CDOM via a microbially mediated process. This is also vivid from Table 2. If the aforementioned processes are responsible for the increase of CDOM in the middle zones of both the estuaries, it is important to know the physical processes augmenting resuspension of bottom settled sediments at this zone.

Since the estuaries converge in the upstream, they are narrow and shallow at the upper zone (Unnikrishnan et al., 1997). But the degree of decrease of depth and width of the estuaries from the lower to middle zone is different. At the lower zone, the Mandovi estuary is 5.8 m deep and 3.2 km wide. It decreases to 4.0 m and 0.8 km at the middle zone. Similarly, the depth and width of the Zuari estuary decreases to 3.0 m and 1 km at the middle zone from 8.0 m depth and 5.5 km width at the lower zone. The momentum balance in a shallow estuary is pressure gradient and friction. In the case of funnel shaped (converging type) estuaries like the Mandovi and Zuari, where the cross sectional area decreases upstream, the amplification due to convergence of the channel cancels decay due to friction, leaving the amplitude unchanged over long distances along the channels (Friedrichs and Aubrey, 1994). In such estuaries when the fresh water discharge decreases, as monsoon recedes, the effect of tide (sea water flux) becomes significant and the frictional effect at the bottom of the estuaries generates turbulence which is sufficient to break the monsoonal (salt-wedge) characteristics of the estuaries and convert them into partially mixed during post-monsoon. This mixing helps in resuspension of the bottom settled sediments which in turn induces CDOM in the middle zone of both the estuaries and augments the concentration during this season.

This might also be responsible for the shedding of CDOM rich water from the middle zone of the Zuari estuary (Fig. 4) towards the offshore region (the salt-wedge extends up to the middle zone in the Zuari estuary). But this type of a secluded plume is not seen at the mouth of the Mandovi estuary. As the salt-wedge is formed at the lower zone (depth 5.8 m) of the Mandovi estuary, a momentum balance exists between the fresh water (pressure gradient) and friction. Hence the tide generated bottom turbulence is not sufficient to break the wedge and that results in the gradual diffusion of CDOM from the lower zone of the Mandovi to the offshore region.

In their studies, Boss et al. (2001) suggested that sediment resuspension events driven by storms have also been observed to contribute to CDOM in bottom waters. In their attempt to analyse estuarine colour components during pre-monsoon season, Menon et al. (2006a) had observed high incidence of CDOM in the region of sediment plumes.

It is interesting to note an opposite relation of S with salinity between the Mandovi and Zuari estuaries during this season. In the Mandovi, the relation is negative and the regression coefficient is −0.75, while in the Zuari it is positive and the coefficient is 0.48. This means coastal advection of saline waters is yet another source of CDOM contributing significantly to the lower zone of the Mandovi estuary. Hence the combined effect of coastal advection, terrestrial input and in situ production caused the lower zone of the Mandovi estuary to have more CDOM than the respective zone of the the Zuari estuary during this season.

4.4. Reversal of current direction

Apart from the estuarine region, OCM data also revealed the CDOM build up at the coastal inshore waters south of the Zuari

estuary during October (Fig. 4). It was reported that the area between 8 and 15° N (south of 15° N), along the eastern Arabian sea, is productive during the southwest monsoon (Madhupratap et al., 2001). During the fall inter-monsoon (October and November) period, CDOM concentration increases due to the disintegration of chlorophyll_a. Moreover, the current reverses from equatorward to poleward during October. This might have acted as an agent to transport CDOM rich waters along the coastal inshore region south of the Zuari estuary.

In their studies, Keith et al. (2002) indicated that phytoplankton utilises accessory pigments at longer wavelengths when the CDOM absorption is high and values of S less than or equal to 0.02. This criterion holds well in the present case wherein the Mandovi estuary has more CDOM concentration than the Zuari estuary. It was reported that the Mandovi estuary is less productive than the Zuari estuary (Krishna Kumari et al., 2002).

5. Conclusion

Remote analysis of CDOM using OCM data revealed that temporal and spatial variability of CDOM in the Mandovi and Zuari estuaries is controlled by seasonal hydrodynamics. This is evident from the presence of more CDOM-rich waters in the lower zone and coastal inshore region of the estuaries by the end of pre-monsoon and accumulation of high CDOM waters in the middle zone of both the estuaries by the end of the post-monsoon season. This is the first time that CDOM in these estuaries has been remotely analysed for an entire year through an optical sensor having a spatial resolution of 360 m. Of the two estuaries, the Mandovi experiences a higher CDOM concentration and maximum variability. The study could also assess the fate of secluded CDOM rich water (plume) in the offshore region during the initial phase of post-monsoon. Though monsoonal fresh water flux is the major source of CDOM in both the estuaries, its contribution is more predominant in the Mandovi estuary than in the Zuari estuary. The study revealed that it is possible to analyse the fate of CDOM synoptically through an optical sensor, if equipped with a good site- specific algorithm. Success in mapping CDOM and studying its temporal variation in estuaries will help in developing a basic tool to understand and monitor the discharge of dissolved organic matter from non-point sources which is responsible for making a coastal region hypoxic.

Acknowledgements

References

Arenz, R.F., Lewis, W.M., d Saunders, J.F., 1996. Determination of chlorophyll and dissolved organic carbon from reflectance data for Colorado reservoir. International Journal of Remote Sensing 17 (8), 1547–1566.

Bhargava, R.M.S., Dwivedi, S.N., 1974. Diurnal variation in phytoplankton pigment in Zuari estuary, Goa. Indian Journal of Marine Science 3 (December), 142–145.

Boss, E., Pegau, W.S., Zaneveld, J.R.V., Barnard, A.H., 2001. Spatial and temporal variability of absorption by dissolved material at a continental shelf. Journal of Geophysical Research 106 (C5), 9499–9507.

Bricaud, A., Morel, A., Prieur, L., 1981. Absorption by dissolved organic matter of the sea (yellow substance) in the UV and visible domains. Limnology and Oceanography 26 (1), 43–53.

Carder, K.L., Steward, R.G., Harvey, G.R., Ortner, P.B., 1989. Marine humic and fulvic acids: their effects on remote sensing of ocean chlorophyll. Limnology and Oceanography 34 (1), 68–81.

Chylek, P., Henderson, B., Mischchenko, M., 2003. Aerosol radiative forcing and the accuracy of satellite aerosol optical depth retrieval. Journal of Geophysical Research 108, 4764. doi:10.1029/2003JD004044.

Del Castillo, C.E., Gilbes, F., Coble, P.G., Muller-Karger, F.E., 2000. On the dispersal of riverine colored dissolved organic matter over the West Florida Shelf. Limnology and Oceanography 45 (6), 1425–1432.

Devassy, V.P., Bhattathiri, P.M., Qazim, S.Z., 1979. Trichodesmium phenomenon. Indian Journal of Marine Science 8 (June), 89–93.

Devassy, V.P., Goes, J.I., 1989. Seasonal patterns of phytoplankton biomass and productivity in tropical estuarine complex (west coast of India). Proceedings of the Indian Academy of sciences: Plant Sciences 99, 485–501.

Doerffer, R., 1992. Imaging spectroscopy for detection of chlorophyll and suspended matter. In: GKSS 92/E/54, pp. 215–257.

Foden, J., Sivyer, D.B., Mills, D.K., Devlin, M.J., 2008. Spatial and temporal distribution of chromophoric dissolved organic matter (CDOM) fluorescence and it contribution to light attenuation in UK water bodies. Estuarine, Coastal and Shelf Science 79 (4), 707–717.

Friedrichs, C.T., Aubrey, D.G., 1994. Tidal propagation in strongly convergent channels. Journal of Geophysical Research 99 (C2), 3321–3336. doi:10.1029/93JC03219.

Green, S., Blough, N., 1994. Optical absorption and fluorescence properties of chromophoric dissolved organic matter in the natural waters. Limnology and Oceanography 39 (8), 1903–1916.

Hojerslev, N.K., Aas, E., 2001. Spectral light absorption by yellow substance in the Kattegat-Skagerrak area. Oceanologia 43 (1), 39–60.

Keith, D.J., Yoder, J.A., Freeman, S.A., 2002. Spatial and temporal distribution of coloured dissolved organic matter (CDOM) in Narragansett Bay, Rhode Island: implications for Phytoplankton in coastal waters. Estuarine, Coastal and Shelf Science 55 (5), 705–717.

Kowalczuk, P., Kaczmarek, S., 1996. Analysis of temporal and spatial variability of 'yellow substance' absorption in the Southern Baltic. Oceanologia 38 (1), 3–32.

Krishna Kumari, L., Bhattathiri, P.M.A., Matondkar, S.G.P., John, Julie, 2002. Primary productivity in Mandovi–Zuari estuaries in Goa. Journal of Marine biological Association of India 44 (1–2), 1–13.

Madhupratap, M., Nair, K.N.V., Gopalakrishnan, T.C., Haridas, P., Nair, K.K.C., Venugopal, P., Mangesh Gauns, 2001. Arabian sea oceanography and fisheries of the west coast of India. Current Science 81 (4), 355–361.

Magnuson, A., Harding Jr., L.W., Mallonee, M.E., Adolf, J.E., 2004. Bio-optical model for Chesapeake Bay and the Middle Atlantic Bight. Estuarine, Coastal and Shelf Science 61 (3), 403–424.

Menon, H.B., 2004. Calibration of an optical equation to analyse the atmospheric turbidity and water quality of an estuarine environment. Photonirvachak 32 (3), 287–300.

Menon, H.B., Lotliker, A., Nayak, S.R., 2005. Pre-monsoon bio-optical properties in estuarine, coastal and Lakshadweep waters. Estuarine, Coastal and Shelf Science 63 (1–2), 211–223.

Menon, H.B., Lotliker, A, A., Nayak, S.R., 2006a. Analysis of estuarine colour components during non-monsoon period through Ocean Colour Monitor. Estuarine, Coastal and Shelf Science 66 (3–4), 523–531.

Menon, H.B., Lotliker, A.A., Krishna Moorthy, K., Nayak, S.R., 2006b. Variability of remote sensing reflectance and implications for optical remote sensing—a study along the eastern and north eastern waters of Arabian Sea. Geophysical Research Letters 33, L15602. doi:10.1029/2006 GL 026026.

Muller-Karger, F.E., Varela, R., Thunell, R., Luerssen, R., Hu, C., Walsh, J.J., 2005. The importance of continental margins in the global carbon cycle. Geophysical Research Letters 32, L01602.

Naqvi, S.W.A., Jayakumar, D.A., Narvekar, P.V., Naik, H., Sarma, V.V.S.S., D'Souza, W., Joseph, S, George, M.D., 2000. Increased marine production of N_2O due to intensifying anoxia on the Indian continental shelf. Nature 408, 346–349.

Odriozolaa, A.L., Varelab, R., Hua, C., Astorb, Y., Lorenzonia, L., Muller-Karger, F.E., 2007. On the absorption of light in the Orinoco river plume. Continental Shelf Research 27 (10–11), 1447–1464.

Padmavati, G., Goswami, S.C., 1996. Zooplankton ecology in the Mandovi–Zuari estuarine system of Goa, West coast of India. Indian Journal of Marine Science 25 (September), 268–273.

Qasim, S.Z., 2003. Indian Estuaries. Allied Publishers Pvt. Ltd., New Delhi.

Rochelle-Newall, E.J., Fisher, T.R., 2002a. Chromophoric dissolved organic matter and dissolved organic carbon in Chesapeake Bay. Marine Chemistry 77 (1), 23–42.

Rochelle-Newall, E.J., Fisher, T.R., 2002b. Production of chromophoric dissolved organic matter fluorescence environment in marine and estuarine environment: in investigation into the role of phytoplankton. Marine Chemistry 77 (1), 7–22.

Shetye, S.R., Gouveia, A.D., Singbal, S.Y.S., Naik, C.G., Sundar, D., Michael, G.S., Nampoothiri, G., 1995. Propagation of tides in the Mandovi–Zuari estuarine network. Proceedings of the Indian Academy of Sciences 104, 667–682.

Singbal, S.Y.S., 1973. Diurnal variation of some Physico-chemical factors in the Zuari Estuary of Goa. Indian Journal of Marine Sciences 2 (June), 90–93.

Strickland, J.D.H., Parsons, T.R., 1972. A Practical Handbook of Seawater Analysis. Fisheries Board of Canada, pp. 295–300, Bulletin 167, 2nd ed.

Twardowski, M.S., Donaghay, P.L., 2001. Separating in situ and terrigenous sources of absorption by dissolved materials in coastal waters. Journal of Geophysical Research 106 (C2), 2545–2560.

Unnikrishnan, A.S., Shetye, S.R., Gouveia, A.D., 1997. Tidal propagation in the Mandovi–Zuari estuarine network, west coast of India: impact of fresh water influx. Estuarine, Coastal and Shelf Science 45 (6), 737–744.

Vodacek, A., Blough, N.V., DeGrandpre, M.D., Peltzer, E.T., Nelson, R.K., 1997. Seasonal variation of CDOM and DOC in the Middle Atlantic Bight: terrestrial inputs and photooxidation. Limnology and Oceanography 42 (4), 674–686.

Aerosol optical thickness and spatial variability along coastal and offshore waters of the eastern Arabian Sea

Harilal B. Menon[1]*, Nutan Sangekar[1], Aneesh Lotliker[1], Krishnaswamy Krishnamoorthy[2], and Ponnumani Vethamony[3]

[1]Department of Marine Sciences, Goa University, University PO, Goa 403206, India
[2]Space Physics Laboratory, Vikram Sarabhai Space Centre, Thiruvananthapuram, Kerala, India
[3]National Institute of Oceanography, Dona-Paula, Goa 403004, India

*Corresponding Author: tel: +91 832 651 9350; fax: +91 832 245 1184; e-mail: harilalm@gmail.com.

Data from the ocean-colour monitor (OCM) on board the Indian Remote Sensing Satellite P4 were used to analyse the spatial and temporal distribution of aerosol optical thickness (AOT) over the coastal and offshore waters of the eastern Arabian Sea. Zero water-leaving radiance from the near infrared (NIR) region was assumed for oceanic (open ocean) waters, because of the absorption of long-wave radiation by water molecules. As this assumption fails in coastal waters, it was necessary to correct for water-leaving radiance and sun glint to the NIR bands. The aerosol size-distribution parameter (α) was derived from a relationship between two NIR bands. The Ångström turbidity parameter (β) was obtained using an algorithm relating in situ hand-held, sun-photometer measurements and aerosol radiance (L_a) at 490 nm. The relationship between β and L_a (490) was derived with a sensitivity analysis, using a calibrated radiative transfer model. AOTs were retrieved for each pixel of 500 nm. The algorithm's performance was tested by comparing OCM-derived AOT values with in situ AOT and MODIS-derived values. Aerosol maps thus generated from January to December 2005 demonstrate the potential of this new retrieval method for producing AOT climatology from OCM data over coastal waters.

Keywords: aerosol optical thickness, coastal waters, eastern Arabian Sea, offshore, spatial variability.

Introduction

The atmosphere above the North Indian Ocean is subject to aerosol radiative forcing resulting from seasonally reversing summer (southwest) and winter (northeast) monsoon winds. Several Indian programmes have been initiated to understand the direct and indirect effect of these aerosols on climate. Analysis of data from the Indian Ocean Experiment (INDOEX, 1997–1999; Ramanathan et al., 2001) revealed northeast monsoon winds as the main agent transporting anthropogenic aerosols over the Arabian Sea. These aerosols, unlike natural maritime aerosols, not only scatter incoming solar radiation, but also absorb it (Satheesh and Ramanathan, 2000; Eck et al., 2001; Li and Ramanathan, 2002) and augment the greenhouse effect. This disclosure motivated an extensive field campaign, the Integrated Campaign for Aerosols, Gases, and Radiation Budget (ICARB) in 2006 (Krishnamoorthy et al., 2008). The combined effect of natural and anthropogenic aerosols could contribute to atmospheric and ecological imbalances in the eastern Arabian Sea. This underlines the need for a synoptic understanding of the atmosphere over the eastern Arabian Sea, including the Ångström turbidity parameter (β), aerosol-size distribution parameter (α), and subsequently aerosol optical thickness (AOT), a quantity required for determining aerosol radiative forcing at the top of the atmosphere.

The role of aerosols in climate change remains uncertain. Although the theory behind their effect on outgoing terrestrial and incoming solar radiations is well understood, spatial and temporal variability make it difficult to assess their magnitude with in situ observations. Satellite remote sensing is the only means of providing the synoptic coverage needed for analysing aerosol radiative forcing at the top of the atmosphere. Rajeev and Ramanathan (2002) discussed the spatial distribution of AOT over the open ocean (Arabian Sea and Bay of Bengal) at a spatial resolution of 1.1 km, using data for the 630-nm band of Advanced Very High-Resolution Radiometer (AVHRR) on board the National Oceanic and Atmospheric Administration (NOAA) satellite. However, an analysis of the small-scale features associated with aerosol distribution over optically complex areas, such as the coastal waters of the eastern Arabian Sea, requires sensors with higher temporal and spatial resolution. The ocean-colour monitor (OCM) on board the Indian Remote Sensing Satellite (IRS) P4 provides spatial and temporal resolutions of 360 m and 2 d, respectively. Previous attempts to retrieve AOT from OCM data over the eastern Arabian Sea (Das et al., 2002; Dey et al., 2004; Chauhan et al., 2009) assumed that sensor radiance of NIR bands resulted entirely from atmospheric backscattering. However, this assumption holds only in oceanic and not in turbid coastal waters. The current study aims to formulate a technique to derive AOT from OCM over coastal waters and to demonstrate the method's potential for analysing aerosol distribution along the eastern coastal Arabian Sea. In a fisheries context, these AOT values could be used to estimate aerosol

radiance as a part of the complex atmospheric correction procedure, resulting in more accurate values of chlorophyll *a*.

Material and methods
Study area and data collection
The AOT over oceanic and coastal regions of the eastern Arabian Sea (Figure 1), including the estuaries of Mandovi and Zuari (Goa, India), was studied as part of the Indian Space Research Organization's Geosphere Biosphere Programme. Oceanic observations were obtained from the RV "Sagar Kanya" in an area bounded by 14°20′–22°35′N and 65°–73°34′E during the period 4–18 December 2004. Coastal waters were surveyed by the RV "Sagar Purvi" from 23 to 28 November 2004. Six estuarine surveys were conducted using a fishing vessel on 12 February, 18 March, 13 April, 11 May, 11 November, and 9 December 2005.

A Microtops II hand-held sun photometer, with bands at 380, 440, 500, 675, and 870 nm, was used to measure AOT (full field view of 2.5°). A global positioning system interfaced with the Microtops II provided accurate time and position of each station. During all field surveys, AOTs were measured between 09:00 and 16:00 at 30 min intervals, in association with the IRS P4 satellite pass (12:00). This provided a total of 210, 78, and 90 observations for the oceanic, coastal, and estuarine surveys, respectively.

Predetermined stations (Figure 1) for *in situ* observations were located between depths of 30 and 1000 m (8–700 km from shore) to prevent water-pixel contamination from land radiance. Profiles of downwelling irradiance and upwelling radiances were obtained with a Satlantic in-water radiometer at all stations. In addition, surface water samples were collected to determine the concentration of optically active substances (OASs), including suspended organic matter (chlorophyll *a*), inorganic matter (sediment), and chromophoric dissolved organic matter (CDOM), using

methods described by Menon *et al.* (2005). Radiometer measurements and water-sample collection were carried out simultaneously from the sunlit side of the ship to avoid any discrepancy in the computation of water-leaving radiance resulting from a change in the sun's zenith angle.

Generation of α and β from *in situ* measurements
According to Ångström (1961), the spectral variation of AOT is expressed as

$$\tau_a(\lambda) = \beta\lambda^{-\alpha}, \tag{1}$$

where $\tau_a(\lambda)$ is the AOT, β (often referred to as the Ångström turbidity parameter; Ångström, 1964) represents the AOT at the reference wavelength (i.e. $\lambda = 1$), which may be viewed as an indicator of total aerosols present in the atmosphere, and α is the Ångström coefficient, which depends on the size distribution of the aerosol. Each spectral measurement of AOT was fitted to Equation (1) using linear least-squares fitting of log-transformed data to obtain α as the slope of the regression line and log β as the intercept. Low and high values of α indicate coarse (maritime) and fine (continental) aerosol particle sizes, respectively.

OCM characteristics and data processing
OCM data from the IRS P4 satellite were analysed to retrieve AOT. OCM has eight bands; six visible and two near infrared (NIR), centred at 412, 443, 490, 510, 555, 670, 765, and 865 nm. The first six bands are used for analysing the OAS (ocean-colour components) in the water column and the remaining two for measuring path radiance (aerosol and Rayleigh radiances) to apply atmospheric correction for ocean-colour analysis. The spectral resolution of the visible and NIR bands are 20 and 40 nm, respectively.
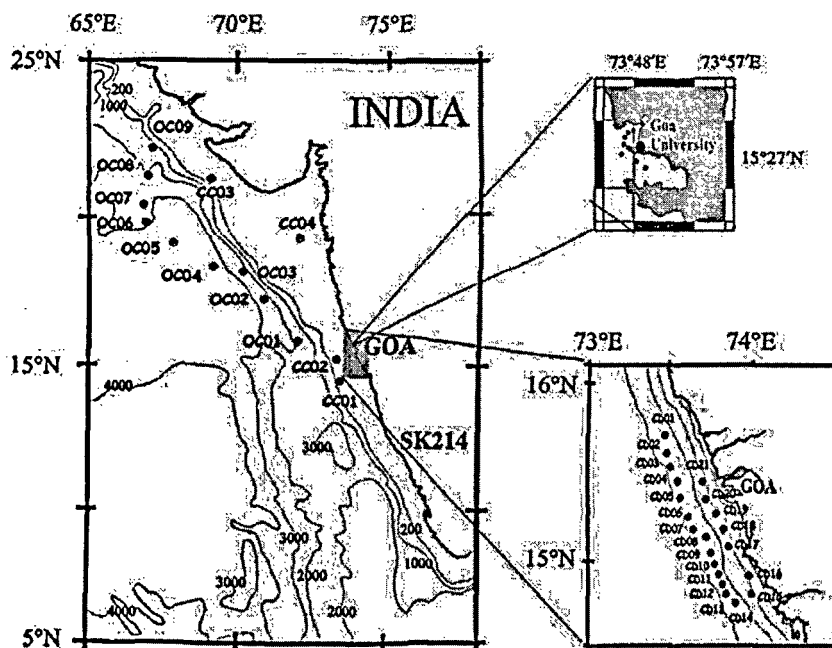
Figure 1. Map of the study area showing the *in situ* sampling locations and depth contours. Main panel: oceanic observations, RV "Sagar Kanya"; top inset: estuarine observations, fishing trawler; bottom inset: coastal observations, RV "Sagar Purvi".

Images were georeferenced using ground control points and the study area was extracted using image processing software. During the months November–January, because the aerosol plume builds around 22°N, two OCM images were processed to include the area between 10 and 23°N. For the other months, only one image, covering the area between 5 and 20°N, was processed. Cloud cover prevented analysis of aerosol parameters during the period June–August. To validate the AOT retrieval method from OCM further, AOTs derived seasonally from OCM pixels over oceanic waters (8–15°N) were compared with AOTs from MODIS. This comparison was made between the mean of nine adjacent pixels of AOT from OCM and the corresponding pixels of MODIS.

Aerosol retrieval from OCM data

The radiance received by a space-borne optical sensor from a turbid coastal waterbody in a specific band λ can be divided into different components as

$$L_t(\lambda) = L_p(\lambda) + t(\lambda) \times L_g(\lambda) + L_w(\lambda) \times T_d(\lambda), \quad (2)$$

where $L_p(\lambda)$ is the path radiance resulting from aerosol and Rayleigh scattering in the atmosphere, $L_g(\lambda)$ the sun glint resulting from specular reflection from the sea surface, and $L_w(\lambda)$ the radiance leaving the water column. $T_d(\lambda)$ and $t(\lambda)$ are the diffuse and direct transmittance terms, respectively.

Aerosol radiance, a component of path radiance, contains information on the atmospheric aerosol. To retrieve β from aerosol radiance, the atmospheric path radiance L_p of NIR bands needs to be partitioned into aerosol (L_a) and Rayleigh (L_r), radiances as follows:

$$L_p(\lambda) = L_a(\lambda) + L_r(\lambda). \quad (3)$$

Rayleigh radiance [$L_r(\lambda)$] was computed as per Gordon *et al.* (1988) and removed from the L_p of NIR bands. As water molecules absorb long-wave radiation, Rayleigh correction to pixels of NIR bands should yield L_a over oceanic waters. However, $L_w(\lambda)$ in NIR bands from the turbid coastal waters is non-zero (Moore *et al.*, 1999). In addition, radiance resulting from specular reflection [sun glint, $L_g(\lambda)$] contributes to radiance measured in the NIR bands. Therefore, $L_r(\lambda)$, $L_w(\lambda)$, and $L_g(\lambda)$ correction should be applied to NIR bands. $L_g(\lambda)$ correction was applied to the NIR bands as per Wang and Bailey (2001). Wind velocity for the computation of sun glint was measured using an automatic weather station installed on board ship.

The water-leaving radiance correction to 765 nm pixels was applied using the remote-sensing reflectance (R_{rs}) at 765 nm [$R_{rs}(765)$], measured from the *in situ* radiometer measurements. The OAS effect on R_{rs} at 865 nm was computed using a calibrated radiative-transfer model (Menon, 2004) because the Satlantic radiometer does not have a band at this wavelength. Although the data revealed a direct relationship between reflectance and OAS concentration at 765 nm, this was not the case for the 865-nm band. Suspended organic and inorganic particles scatter and absorb light, whereas dissolved components only absorb it (Bricaud *et al.*, 1981; Menon *et al.*, 2005). A multiple regression analysis of $R_{rs}(765)$ with OAS components revealed that neither chlorophyll *a* nor CDOM affects it, but that suspended sediment contributes to it at concentrations >4 mg l^{-1}. The water-leaving radiance at 4 mg l^{-1} is 0.0184 μW m^{-2} nm^{-1} sr^{-1}. At 765 nm,

this gives

$$L_u(0^+, 765) = R_{rs}(0^+, 765) \times E_d(0^+, 765), \quad (4)$$

where $L_u(0^+, 765)$ is the upwelling radiance at the water surface, $R_{rs}(0^+, 765)$ the remote-sensing reflectance, and $E_d(0^+, 765)$ the downwelling irradiance at 765 nm at the water surface. $E_d(0^+, 765)$ and $L_u(0^+, 765)$ were obtained from the Satlantic radiometer.

Pixels with sediment concentration >4 mg l^{-1} were corrected as follows. For pixels coinciding with station positions, the water-leaving radiance correction was applied by computing the respective radiance; for other pixels, the correction was applied to the mean of nine pixels adjacent to the station. Aerosol radiance (L_a) thus obtained could be expressed as

$$L_a(\lambda) = F_s(\lambda) \tau_a(\lambda) \omega_{oa} \times \frac{P_a}{4\pi\cos(\theta_v)}, \quad (5)$$

where $F_s(\lambda)$ is the extraterrestrial solar irradiance, $\tau_a(\lambda) = \beta\lambda^{-\alpha}$ is the AOT, ω_{oa} the aerosol single-scattering albedo, P_a the aerosol phase function, and θ_v the satellite view angle. Assuming that phase function and single-scattering albedo are spectrally invariant at a specific time over the short range of wavelength considered (765–865 nm), and taking the ratio of Equation (5) for the two NIR bands of OCM, results in the following relation that can be used to map α from OCM:

$$\alpha = \frac{\log(L_{a1}/F_{s1}) - \log(L_{a2}/F_{s2})}{\log(\lambda_2) - \log(\lambda_1)}, \quad (6)$$

where L_{a1} and L_{a2} are aerosol radiances corresponding to 765 and 865 nm, respectively, and F_{s1} and F_{s2} are the respective extraterrestrial solar irradiances. Another parameter required for the retrieval of AOT is β, the Ångström turbidity parameter.

An algorithm was developed using results from a sensitivity analysis of a radiative-transfer model (Menon, 2004) to retrieve β from OCM, as follows. Spectral (400–700 nm) aerosol radiances (L_a) were computed at 1-nm intervals for the range of β values (0.1–0.4) encountered over an Indian coastal station. While simulating aerosol radiances, the variables α, zenith angle, azimuth angle, atmospheric gaseous constituents, and OAS were held constant. Approximately 200 spectra of aerosol radiances were simulated for the wavelength range. The L_a corresponding to the least β was taken as the baseline spectrum; all other L_a spectra were
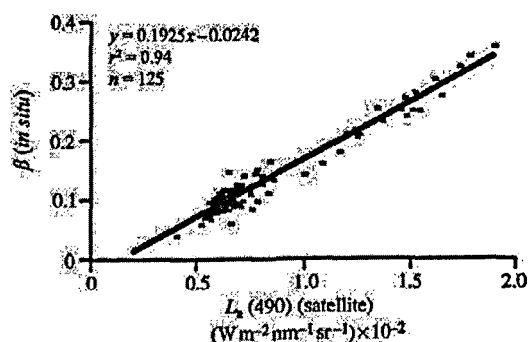

Figure 2. Regression between *in situ* β (Ångström turbidity parameter) and satellite-derived L_a 490 (aerosol radiance at 490 nm).

then divided by this baseline. This demonstrated that maximum sensitivity to change in β was at 490 nm. The following linear relationship was then obtained between satellite-derived L_a (490) and *in situ*-derived β ($r^2 = 0.95$; Figure 2):

$$\beta = 0.1925L_a(490) - 0.0242. \qquad (7)$$

In situ data for alternate days were grouped into two sets and used for developing and validating the algorithm. Altogether, 125 observations were used. Of these, 75 were generated during the RV "Sagar Kanya" survey and 25 each from the RV "Sagar Purvi" and fishing vessel surveys. Next, $L_a(490)$ from OCM was obtained by rearranging the ratio of Equation (6) for 765 nm and shorter wavelengths, so allowing computation of L_a for these wavelengths:

$$L_a(\lambda < 765\,\text{nm}) = L_a(765\,\text{nm})\left[\frac{F_s(\lambda)}{F_s(765\,\text{nm})}\right]\left(\frac{\lambda}{765}\right)^{-\alpha}, \qquad (8)$$

where α is the value obtained using Equation (6) derived from satellite data.

Nine OCM images (10 January, 12 February, 18 March, 11 April, 11 May, 20 September, 6 October, 25 November, and 12 December 2005) were then processed to retrieve α and β parameters. The Ångström (1961) equation was then applied, and AOTs and α at 500 nm were mapped.

Validation

In all, 150 observations (90, 45, and 15 from the RV "Sagar Kanya", RV "Sagar Purvi", and fishing vessel surveys, respectively) were used for validation of satellite-derived values. Each pixel contained more than one *in situ* value. Hence, averages of α and β were compared with the mean values of the adjacent nine pixels in the satellite imagery. To avoid possible land interference (estuarine width decreases upstream), only those observations taken at the mouth were considered for validation.

To authenticate the method further, AOTs derived seasonally from OCM cloud-free pixels in an open-ocean region between 8 and 15°N (not in the area of *in situ* observations) were compared
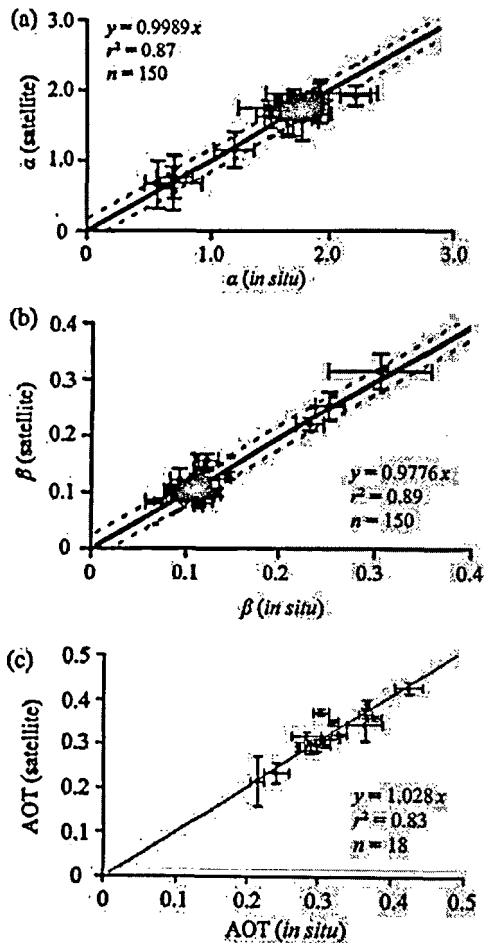

Figure 3. Correlation between (a) satellite- and *in situ*-derived α (aerosol size distribution parameter), (b) satellite-derived and *in situ* β (Ångström turbidity parameter), and (c) satellite-derived AOT and *in situ* values for validation. Dotted lines in (a) and (b) are the 95% confidence levels, and vertical and horizontal bars the s.d.
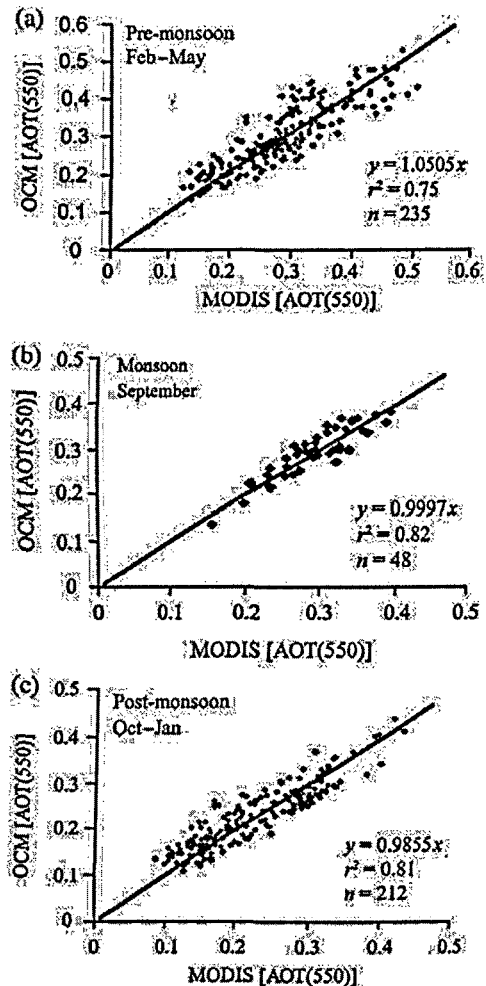
Figure 4. Correlation between AOT at 550 nm derived from OCM and MODIS for (a) pre-monsoon, (b) monsoon, and (c) post-monsoon seasons.

with AOTs from MODIS. MODIS has a 550-nm band; consequently, AOTs from OCM-derived α and β at 550 nm were used for the comparison.

Results and discussion

Validation

In general, OCM-derived products and *in situ* observations are in good agreement and in the same range (Figure 3a–c). In particular, there was good agreement between satellite-derived and *in situ* AOT values (Figure 3c). The confidence level, RMS error, and mean difference bias were computed for this relationship, and were 95, 2.267, and 0.965%, respectively. Moreover, the zero offset and slope close to unity supports the accuracy of the retrieval. There was also good agreement between OCM- and MODIS-derived AOTs during the pre-monsoon (February–May), end of monsoon (September), and post-monsoon (October–January) seasons (Figure 4a–c).

Aerosol distribution

The spatial distribution of satellite-derived AOT during the months January–December (Figure 5a) reveals an inter- and intraseasonal variability over the study area. AOT is significantly higher during the pre- (January–May) than in the post-monsoon (September–December) season. Aerosol plumes originating at the western margin of the Indian subcontinent extend deep into the offshore region during the pre-monsoon, with AOT ranging from 0.2 to 0.5.

A low AOT (0.15) in the northeastern region and a high AOT (0.4) along the coast between 15 and 20°N are significant features

during January. AOT values increased farther offshore during this month, and by February formed an offshore aerosol plume. Except for this localized plume, aerosol distribution was spatially uniform (~0.3) in February. During March, aerosol in the inshore region around 20°N 72°E increased, and the offshore plume strengthened further. Three hotspots were then evident, one inshore and two offshore, all orientated northeast–southwest in narrow plumes. By April, these had merged into a single elongated plume with the same orientation. By May, this plume had dissipated into patches of intermittent low and high values along the coast and offshore. Examination of wind patterns from NCEP/NCAR reanalysis data (a joint product from the US National Centers for Environmental Prediction and the National Center for Atmospheric Research) revealed that the northerly winds during January had changed to northeasterly by April, suggesting that changes in wind direction caused these changes in aerosol distribution. During winter, strong northeast monsoon winds maintain a vertical moisture gradient by bringing dry, continental air over the eastern Arabian Sea, so allowing continued intense evaporation (Prasannakumar *et al.*, 2001). This results in increased atmospheric humidity and subsequent atmospheric convection. Increased humidity increases aerosol particle size because of hygroscopic growth (Im *et al.*, 2001). This augments scattering, resulting in increased optical thickness. This process might cause the high AOT (0.5) values at the plume's core. In their studies, Li and Ramanathan (2002) noted that AOT is high over both the Arabian Sea and the Bay of Bengal during the northeast monsoon. They observed aerosol plumes over the Arabian Sea
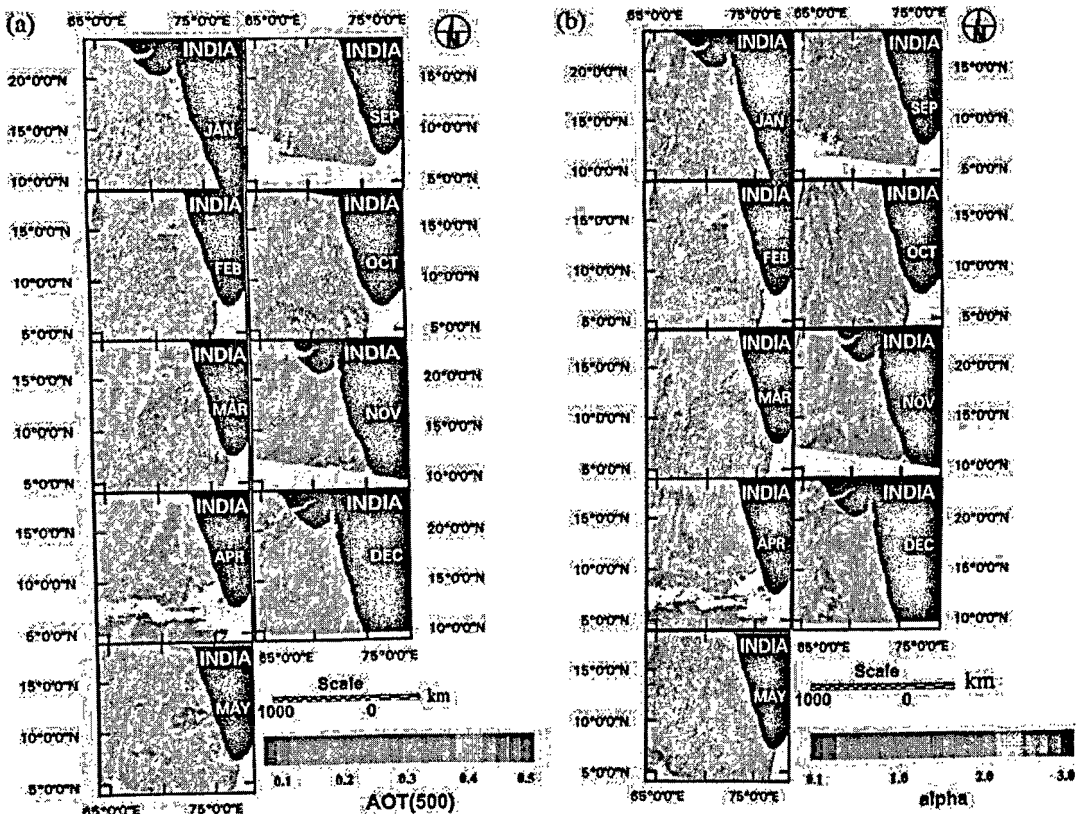
Figure 5. Spatial distribution of (a) AOT at 500 nm, and (b) α derived with OCM data for 10 January, 12 February, 18 March, 11 April, 11 May, 20 September, 6 October, 26 November, and 10 December 2005.

and attributed them to the advection of continental anthropogenic emissions. Similar results were obtained in a study examining the role of synoptic and mesoscale weather patterns on aerosol spectral optical depths and size characteristics at a coastal industrial site in India (Niranjan *et al.*, 2004).

The aerosol pattern during May could be explained based on changing wind direction. The Findlater Jet (also known as the Somali Jet) originates around 10°S and progresses northwards as the southwest monsoon advances. It then becomes southwesterly to westerly while crossing the equator (Menon, 1989), intensifying by May and beginning to blow from the African continent in a southwesterly–westerly direction, resulting in the observed redistribution of aerosol along the coast. Studies in the southern Arabian Sea demonstrated that during May, southwesterly–westerly winds bring mineral dust from Arabia and North Africa (Li and Ramanathan, 2002). The type of aerosol over the study area is indicated by the temporal distribution of the aerosol size distribution parameter (α; Figure 5b). Low values of α and the large optical thickness along the coast clearly indicate enhanced loading of mineral dust aerosols during May compared with earlier months. However, this could be supplemented by coarse mode marine aerosols generated and transported by westerly winds, which increase as the monsoon approaches.

The removal of aerosol because of widespread monsoonal rains from June to August depletes the AOT by September. Wind patterns are intermediate in October, during the initial phase of the transition from southwest to northeast monsoons. This causes an uneven distribution of aerosol along the coast during October (Figure 5a). By the end of November, northeast monsoon winds become more unidirectional, resulting in the concentration of aerosol off 22°N 68°E (Figure 5a). Although AOT decreases gradually towards the south, a patch of aerosol with AOT = 0.5 is seen around 7°N, which could be attributed to sea-salt aerosol. In their studies, Li and Ramanathan (2002) indicated an enhancement in the production of sea salt because of wind. In December, the wind pattern becomes uniform and the plume seen off 22°N and 68°E further strengthens and concentrates in a northeasterly–southwesterly direction.

Conclusions

In a fisheries context, satellite remote sensing of phytoplankton biomass and its temporal and spatial variability in Indian coastal waters are essential to the country's potential fishing zone programme and other initiatives in fishery oceanography using ocean-colour data. However, to obtain the accurate measurements of chlorophyll *a* as an index of phytoplankton biomass from an optical sensor, corrections for atmospheric effects need to be implemented. The current study develops a new algorithm to retrieve aerosol parameters α and β from OCM to compute AOT over coastal turbid waters. These AOT values can be used to estimate aerosol radiance as a part of the complex atmospheric correction procedure resulting in more accurate chlorophyll *a* values.

Acknowledgements

References

Ångström, A. 1961. Techniques of determining the turbidity of the atmosphere. Tellus, 13: 214–223.

Ångström, A. 1964. The parameters of atmospheric turbidity. Tellus, 16: 64–75.

Bricaud, A., Morel, A., and Prieur, L. 1981. Absorption by dissolved organic matter of the sea (yellow substance) in the UV and visible domains. Limnology and Oceanography, 26: 43–53.

Chauhan, P., Sanwlani, N., and Navalgund, R. R. 2009. Aerosol optical depth variability in the northeastern Arabian Sea during winter monsoon: a study using *in-situ* and satellite measurements. Indian Journal of Marine Science, 38: 390–396.

Das, I., Mohan, M., and Krishnamoorthy, K. 2002. Detection of marine aerosols with IRS-P4-OCM. Proceedings of the Indian Academy of Sciences (Earth & Planetary Science), 111: 425–435.

Dey, S., Sarkar, S., and Singh, R. P. 2004. Comparison of aerosol radiative forcing over the Arabian Sea and Bay of Bengal. Advances in Space Research, 33: 1104–1108.

Eck, T. F., Holben, B. N., Dubivik, O., Smirnov, A., Slutsker, I., Lobert, J. M., and Ramanthan, V. 2001. Column-integrated aerosol optical properties over the Maldives during the northeast monsoon for 1998–2000. Journal of Geophysical Research, 106: 28555–28566.

Gordon, H. R., Brown, J. W., and Evans, R. H. 1988. Exact Rayleigh scattering calculations for use with the Nimbus-7 Coastal Zone Color Scanner. Applied Optics, 27: 862–871.

Im, J., Saxena, V. K., and Wenny, B. N. 2001. An assessment of hygroscopic growth factors or aerosols in the surface boundary layer for computing direct radiative forcing. Journal of Geophysical Research, 10: 20213–20224.

Krishnamoorthy, K., Satheesh, S. K., Suresh Babu, S., and Dutt, C. B. S. 2008. Integrated campaign for aerosols, gases and radiation budget (ICARB): an overview. Journal of Earth System Science, 117: 243–262.

Li, F., and Ramanathan, V. 2002. Winter to summer monsoon variation of aerosol optical depth over the tropical Indian Ocean. Journal of Geophysical Research, Atmospheres, 107(D): 4284–4297.

Menon, H. B. 2004. Calibration of an optical equation to analyse the atmosphere turbidity and water quality of an estuarine environment. Journal of the Indian Society of Remote Sensing, 32: 287–300.

Menon, H. B., Lotliker, A. A., and Nayak, S. R. 2005. Pre-monsoon bio-optical properties in estuarine, coastal and Lakshadweep waters. Estuarine Coastal and Shelf Science, 63: 211–223.

Menon, P. A. 1989. Our Weather. National Book Trust, India. 121 pp.

Moore, G. F., Aiken, J., and Lavender, S. J. 1999. The atmospheric correction of water colour and the quantitative retrieval of suspended particulate matter in case 2 waters applications to MERIS. MERIS Special Issue, International Journal of Remote Sensing, 20: 1713–1737.

Niranjan, K., Malleswara, B. R., Saha, A., and Murty, K. S. R. 2004. Aerosol spectral optical depths and size characteristics at a coastal industrial location in India—effect of synoptic and mesoscale weather. Annales Geophysicae, 22: 1851–1860.

Prasannakumar, S., Ramaiah, N., Gauns, M., Sarma, V. V. S. S., Muralidharan, P. M., Raghukumar, S., Dilipkumar, M., et al. 2001. Physical forcing of biological productivity in the northern Arabian Sea during the North east monsoon season. Deep-Sea Research II, 48: 1115–1126.

Rajeev, K., and Ramanathan, V. 2002. The Indian Ocean Experiment: aerosol forcing obtained from satellite data. Advances in Space Research, 29: 1731–1740.

Ramanathan, V., Crutzen, P. J., and Lelieveld, J. 2001. Indian Ocean Experiment: an integrated analysis of the climate forcing and effects of the great Indo-Asian haze. Journal of Geophysical Research, 106: 28371–28398.

Satheesh, S. K., and Ramanathan, V. 2000. Large differences in tropical aerosol forcing at the top of the atmosphere and Earth's surface. Nature, 405: 60–63.

Wang, M., and Bailey, S. W. 2001. Correction of sun-glint contamination on the SeaWiFS ocean and atmosphere products. Applied Optics, 40: 4790–4798.

Measurement of salinity of Mandovi and Zuari estuarine waters from OCM data

Harilal B Menon* & Nutan P Sangekar

Department of Marine Science, Goa University, Goa – 403 206, India
*[E-mail: harilalm@gmail.com]

Present study deals with a method/algorithm to retrieve salinity through optical remote sensing. The basis is the relation between one of the optically active substances of coastal and estuarine waters viz; chromophoric dissolved organic matter (CDOM) and salinity. Two important conditions for the algorithm to work are 1) CDOM should be the main light absorbing component and 2) the main source of CDOM should be fresh water discharge. Relationship between waters with salinity 26 to 35 PSU and CDOM for the Mandovi and Zuari estuaries have been developed and applied to OCM data of the year 2005. Specific algorithm developed[4]is utilized for the study. Validation of satellite retrieved salinity and *in-situ* resulted in a correlation of 0.86.

[Keywords: Salinity, Ocean colour monitor, Estuary, Chromophoric dissolved organic matter]

Introduction

Understanding spatial distribution of salinity in the coastal waters is an important component of the studies of sediment plume, hypoxia[1] and bio-geochemical cycle[2]. In order to get a synoptic picture of salinity, scientists interpolate *in-situ* values which always have inherent errors. In the present study, an attempt has been made to examine the feasibility of retrieval of salinity from ocean color analysis. Colour of the water is the resultant change in the characteristics of incident light while it interacts with suspended organic, inorganic and dissolved organic matters (DOM). The suspended organic matter is chlorophyll a pigment of phytoplankton while the inorganic matter is sediment. Component of DOM interacting with visible light is chromophoric dissolved organic matter (CDOM), which is produced due to disintegration of organic matters (*in-situ*) and through river discharge. The concentration of dissolved organic matter and hence the CDOM is very high in estuarine waters than in any other regions of the water body[3]. In their studies, Menon *et al.*[4] had developed an algorithm to retrieve CDOM from Ocean Colour Monitor (an optical sensor). From the analysis of spectral absorption of visible light, it was shown that there exists a linear relation between the ratio of reflection coefficients in the red and blue or blue and green part of the spectrum and CDOM absorption[5]. This study also revealed the conservative nature of CDOM in estuaries. If CDOM behaves conservatively, then its concentration should vary with the variation of river flow and should have an inverse relation with

salinity. Bowers *et al.*[5] had shown that this relation works in variety of water bodies if CDOM is the main absorber of light.

Materials and Methods

Area of investigation and data

Mandovi and Zuari estuaries are a complex ecosystem joining the Arabian Sea at the central west coast of India (Fig. 1). Hydrodynamics of the estuaries is controlled by both river runoff and tides during monsoon (June—September) season and tide (semi-diurnal in nature with a range 0.2—2 m) during the non-monsoon seasons. This generates significantly different oceanographic processes between dry (non-monsoon) and wet (monsoon) seasons, resulting in the formation of homogenous, salt-wedge and partially mixed estuaries during pre-monsoon, monsoon and post-monsoon seasons.

In-situ observations

The sampling details, selection of stations and the precautions taken in the field may be seen in Menon et al.[6]. Observations were carried out from 22 hydrographic stations along the axis of the estuaries, during pre-monsoon (12th February, 18th March, 13th April and 11th May), monsoon (15th August and 17th September) and post-monsoon (11th November and 9th December) seasons during the year 2005. From each station, two water samples were collected for the analysis of sediment and CDOM. Along with the collection of water samples, observations were also carried out using Secchi Disk, CTD, Microtops II
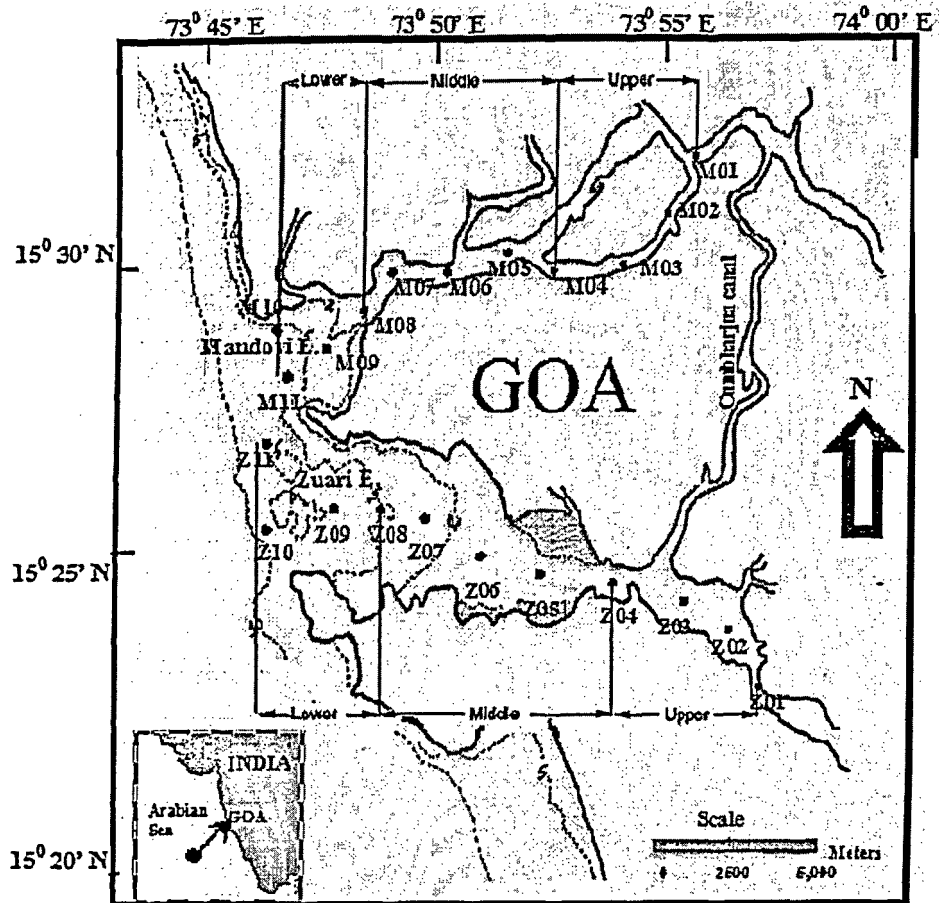
Fig. 1- Map of the study area showing hydrographic stations in different zones of Mandovi and Zuari estuaries of Goa.

sunphotometer, temperature and humidity at each station. Vertical distribution of salinity, at each station, was measured using a CTD. Underwater irradiance was measured using a seven-channel irradiance meter (Satlantic inc).

Suspended sediment from the water sample was measured by gravimetric analysis using pre-weighed 0.45 μm membrane filter. The filters were rinsed in distilled water to remove the salt, allowed to dry, reweighed and kept in oven at 500°C for 3 h. After cooling, once again the filter was weighed for a final analysis. Absorption spectrum of CDOM was measured by Perkin—Elmer dual beam spectrophotometer after filtering samples through 0.2 μm membrane filter. Distilled water was used as a reference. The absorption coefficient was calculated in the way described by Menon et al.[4]. Absorption coefficient at 440 nm was considered as the index of CDOM concentration.

Satellite data processing

Synoptic analysis of salinity was carried out using the data obtained from Ocean Colour Monitor (OCM) flown on board Indian Remote Sensing satellite-P4 (IRS – P4). OCM has six visible and two NIR bands in the range 402 – 885 nm centered at 412, 443, 490, 510, 555, 670, 765 and 865 nm. The spatial resolution and spectral range of the visible bands of OCM are 360 m and 20 nm respectively. The images were geo-referenced using ground control points and the study area was extracted from the full scene through ERDAS Imagine 8.4. Atmospheric correction of data, obtained remotely through an optical sensor, involved elimination of rayleigh and aerosol components. Rayleigh component was computed and removed from each pixel using Doerffer's method[7]. As the water in the study area was turbid, pixels of NIR bands of OCM could not be used to remove aerosol path radiance. Hence aerosol radiance was computed by deriving aerosol optical depth (AOD)

through a Microtops II sunphotometer[8] having filters at 380, 440, 500, 675 and 870 nm. Subsequently, aerosol correction was carried out to each pixel of OCM and water leaving radiance was derived for selected bands. Then applying the algorithm developed by Menon *et al.*[4], a_{CDOM} (440) was retrieved from OCM. This was carried out using a calibrated radiative transfer model[9,4]. Algorithms for the retrieval of CDOM and salinity are given below.

$$a_{CDOM} (440) = 2.9393 (L_w 412/L_w 670)^{-2.2486} \quad ... (1)$$

$$Salinity = (- 2.5355 \times a_{CDOM}(440)) + 34.68 \quad ... (2)$$

Applying the above relation, salinity during the entire year of 2005, except the monsoon season, was retrieved from OCM (Fig 3). Cloud free scenes of OCM on 8th January, 12th February, 18th March, 13th April, 11th May, 23rd September , 6th October, 11th November and 9th December of the year 2005 were used to study the spatial and temporal variability of salinity.

Results

OCM – *in-situ* comparison

In order to validate salinity retrieved from OCM, the accuracy of OCM derived CDOM values was first examined. For the validation, *in-situ* data of CDOM were chosen in such a way that widths of the stations were more than 3 times 360 m, the spatial resolution of OCM. This precaution was taken to avoid overlapping of water pixels with land pixels. Along with the correlation analysis, root mean square (RMS) and bias of the data were also calculated. The data sets were logarithmically transformed (base 10) to calculate RMS and bias. The RMS log error is 14.25% and log difference bias is 3.89%. A good correlation with R equals 0.98 (Fig. 2a), less error and bias further explained the ability of the algorithm in retrieving the sequential variation of CDOM concentration in association with the hydrodynamics of the estuaries. Similarly a good correlation (R = 0.86, Fig. 2c), between salinity retrieved from OCM and *in-situ* values revealed the robustness of salinity algorithm.

Synoptic analysis of salinity from OCM data

To accomplish the task of remotely sensing salinity, it is required to know how the concentration of CDOM in the region varies with salinity. Fig 2b shows a strong linear inverse relation between CDOM and salinity. This relation has been established from
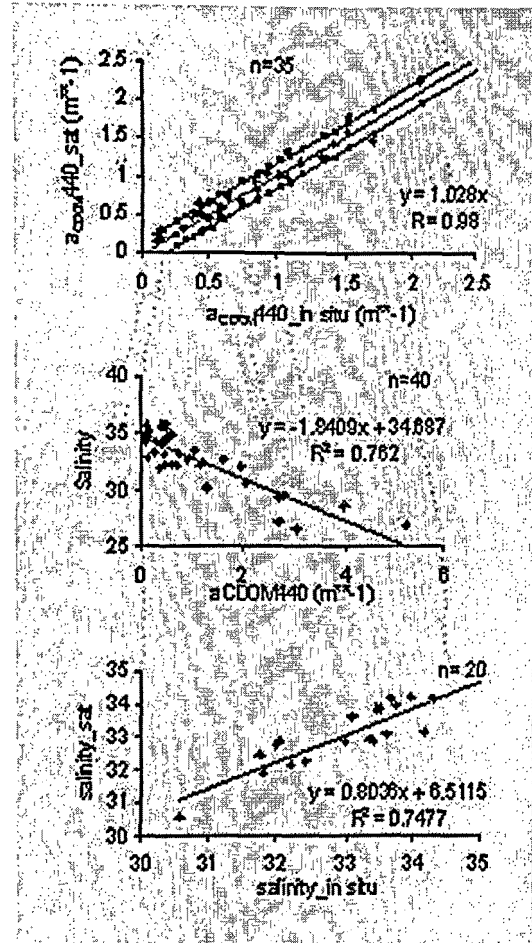

Fig. 2a—Correlation between in-situ and satellite derived a_{CDOM} (440) (the dotted lines in the figure show 95% confidence level).

Fig. 2b—Regression of CDOM and salinity (PSU).

Fig. 2c—Validation satellite retrieved salinity and in-situ measured salinity in of PSU.

40 points from Mandovi and Zuari estuaries. Salinity is ranging from 26 to 35 PSU. Figure 2b proves that CDOM behaves conservatively with respect to salinity and hence could be used as a proxy to salinity. But it is worthwhile to mention that the slope of the regression line varies depending on the concentration of CDOM for 0 PSU. This means, the slope can vary with respect to season and also geographically. To incorporate this variability and thus to map salinity, normalized absorption of CDOM at 440 nm, which is the ratio of $a_{CDOM}(440)$ of the station to $a_{CDOM}(440)$ corresponding to salinity 0 PSU, should be used to develop relation with salinity. Also fine tuning the coefficient on the basis of the entire data set will help

in an algorithm for a region which could work irrespective of the season.

The empirical algorithm was applied to OCM data and salinity for the entire year was mapped (Fig. 3).

Salinity distribution revealed some interesting oceanographic features. Three prominent features are 1) a secluded low salinity plume in the offshore of Zuari estuary, 2) The diffusion of the low salinity plume as
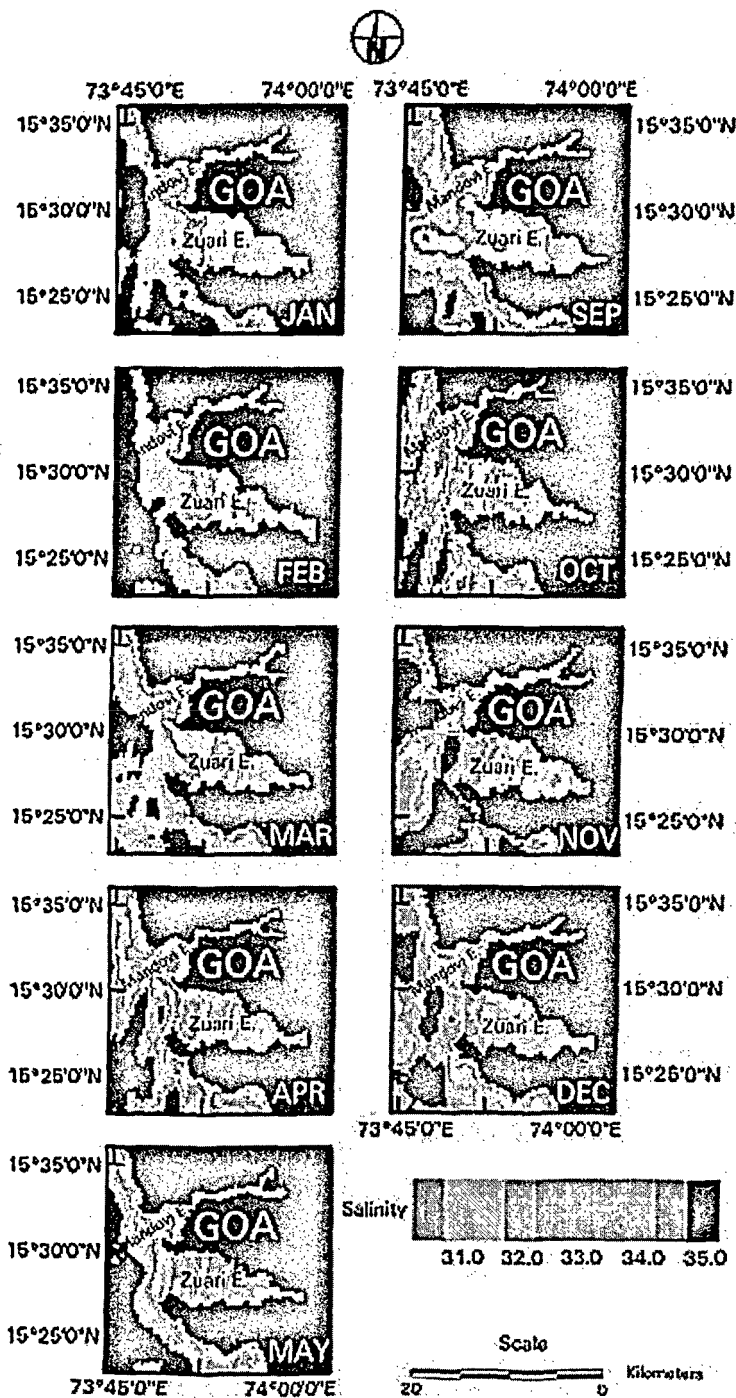

Fig. 3- OCM images of salinity from January to December 2005.

post-monsoon season advances, 3) The transformation of the estuaries from a partially mixed type to homogeneous between February and May.

Discussion

The paper explains a new approach for the synoptic analysis of surface salinity from estuarine waters, having large influence of fresh water discharge, from OCM, an optical sensor, flown onboard IRS – P4. Through a radiative transfer computation, it was shown that major colour components such as chlorophyll a, sediment and CDOM could be retrieved from an optical sensor[1,4]. In the present paper, the work of Menon et al.[4], in retrieving CDOM has been extended to retrieve salinity from OCM data. On the basis of an empirical relation, this was carried out for an entire year 2005. A major requirement for the success of such an empirical relation is that the colour of the water is mainly controlled by this component (CDOM) while the variation of other components is within a range with low sensitivity. Though the colour ratio works well to retrieve salinity from the area of study, the algorithm may not work elsewhere with large variability of other colour components. In such cases, the algorithm can be functional with a new coefficient, when it is tuned with the in-situ data of the area of study. Since the spatial resolution of OCM sensor is 360 m, it is ideal to apply the algorithm in any in-land water bodies with wide range of salinities. But, being a converging funnel shaped estuaries, OCM data could be applied 8 km from the mouth of the estuaries. Hence salinity in the range 30–35 PSU (Fig. 2c) could only be retrieved from OCM data. Unique measurement of salinity from space will enable the oceanographers to study the ecosystem on the basis of synoptic data rather than from point measurements. The advantage of observing salinity of estuaries from space is very significant in the study related to carbon flux to the coastal waters and hence climate.

Conclusion

The study has shown the potential of satellite data for the retrieval of salinity from an optical sensor. This is for the first time that salinity in these estuaries has been analyzed, for an entire year, remotely through an optical sensor having spatial resolution of 360 m. The study could also assess the fate of secluded low salinity plume in the offshore region during the initial phase of post-monsoon. This revealed that it is possible to analyze the salinity pattern, synoptically through an optical sensor, if equipped with good site specific algorithm. A success in mapping salinity and studying for its temporal variation in estuaries will help in developing a basic tool to understand and monitor the discharge of dissolved organic matter from non-point sources which is responsible to make a coastal region hypoxic.

References

1   Kuo, A.Y. & Nielson, B.J., Hypoxia and salinity in Virginia estuaries, *Estuaries*, 10(4)(1987) 277 – 283.
2   Turner, A. & Millward, G.E., Suspended Particles: Their Role in Estuarine Biogeochemical Cycles, *Estuarine, Coastal and Shelf Science*, 55(6)(2002) 857-883.
3   Kirk J.T.O, *Light and photosynthesis in aquatic ecosystems*, (Cambridge, Cambridge University Press) 1994, pp. 509.
4   Menon, H.B., Lotliker, A.A. & Nayak, S.R., Analysis of estuarine colour components during non-monsoon period through Ocean Colour Monitor, *Estuarine, Coastal and Shelf Science*, 66(2006) 523 – 531.
5   Bowers, D.G., Harker, G.E.L., Smith, P.S.D. & Tett, P., Optical properties of a region of fresh water influence (the Clyde sea), *Estuarine, Coastal and Shelf Science*, 50(2000) 717 – 726.
6   Menon, H.B., Lotliker, A.A. & Nayak, S.R., Pre-monsoon bio-optical properties in estuarine, coastal and Lakshadweep waters, *Estuarine, Coastal and Shelf Science*, 63(2005) 211-223.
7   Doerffer, R *Imaging spectroscopy for detection of chlorophyll and suspended matter*, (In GKSS 92/E/54) 1992, pp. 215-257.
8   Chylek, P., Henderson, B. & Mischchenko, M., Aerosol radiative forcing and the accuracy of satellite aerosol optical depth retrieval, *Journal. of Geophysical. Research, R.*,.. 108(2003) 4764.
9   Menon, H.B., Calibration of an optical equation to analyse the atmospheric turbidity and water quality of an estuarine environment, *Photonirvachak*, 32(3)(2004) 287 – 300.